Room-Temperature Phosphorescence and Molecular Conformations of Unsymmetrical Heteroaromatic 1,2-Diketone in the Solid and Liquid States

Mao Komura

2023

Department of Chemistry,

Graduate School of Science, Osaka University

List of Abbreviations

Ac	acetyl
BL	blue light
Bu	butyl
DSC	differential scanning calorimeter
EA	elemental analysis
Et	ethyl
GPC	gel permeation chromatography
HR-MS	high resolution mass spectroscopy
ISC	intersystem crossing
Me	methyl
m.p.	melting point
NMR	nuclear magnetic resonance
OO	1,2-bis[5-(triisopropylsilyl)furan-2-yl]ethane-1,2-dione
PL	photoluminescence
PLQY	photoluminescence quantum yield
PXRD	powder X-ray diffraction
RT	room-temperature
RTP	room-temperature phosphorescence
SCL	supercooled liquid
SS	1,2-bis[3-bromo-5-(triisopropylsilyl)thiophen-2-yl]ethane-1,2-dione
SO	1-(3-Bromo-5-(triisopropylsilyl)furan-2-yl)-2-(3-bromo-5-(triisopropylsilyl)thiophen-2-yl)ethane-1,2-dione
SOC	spin-orbit coupling
THF	tetrahydrofuran
TLC	thin-layer chromatography
UV	ultraviolet
vis	visible
XRD	X-ray diffractometry

List of publications

I. Room-temperature phosphorescence of a supercooled liquid: kinetic stabilisation by desymmetrisation

M. Komura, T. Ogawa and Y. Tani, *Chem. Sci.*, 2021, **12**, 14363–14368.

II. Photoinduced crystal melting with luminescence evolution based on conformational isomerisation

M. Komura, H. Sotome, H. Miyasaka, T. Ogawa and Y. Tani, *Chem. Sci.*, 2023, **14**, 5302–5308.

Supporting publication

1. Y. Tani, M. Terasaki, M. Komura and T. Ogawa, *J. Mater. Chem. C*, 2019, **7**, 11926–11931.
2. Y. Tani, M. Komura and T. Ogawa, *Chem. Commun.*, 2020, **56**, 6810–6813.
3. Y. Tani, K. Miyata, E. Ou, Y. Oshima, M. Komura, M. Terasaki, S. Kimura, T. Ehara, K. Kubo, K. Onda and T. Ogawa, *ChemRxiv* 2023.

Acknowledgement

This research was conducted in Laboratory for Physical Organic Chemistry, department of Chemistry, Graduate School of Science, Osaka University. First, I would like to express my deepest gratitude to Dr. Yosuke Tani at Graduate School of Science, Osaka University, for his many valuable suggestions, discussion, guidance, and continuous encouragement throughout my doctoral journey. His expertise and mentorship were invaluable in shaping the direction of my research. I would like to express my appreciation to Dr. Ken-ichi Yamashita, Prof. Dr. Takuji Ogawa, and Prof. Dr. Takashi Kubo for their guidance, discussion, many suggestions. Their expertise and mentorship were invaluable in fostering my intellectual growth.

Some measurements of this thesis were completed in Miyasaka's Group, at Graduate School of Science, Osaka University. I would like to describe my appreciation to Prof. Dr. Hiroshi Miyasaka and Dr. Hikaru Sotome for on the measurement, analysis, and fruitful discussion. Rheological measurements of this thesis were conducted in Inoue's Group, at Graduate School of Science, Osaka University. I would like to appreciate Prof. Dr. Tadashi Inoue and Dr. Osamu Urakawa, Ms. Arisa Yokokouji for on the instruction of the measurements, analysis, and fruitful discussion.

I would like to appreciate my thesis committee: Prof. Dr. Koichi Fukase, and Prof. Dr. Yasuhisa Mizutani at Graduate School of Engineering Science, Osaka University, for their insightful feedback and discussions. I feel honored to have had this thesis reviewed by two leading researchers.

I wish to acknowledge the *Research Foundation for Opto-Science and Technology*, and Research Fellowships for Young Scientists for their financial support during my Ph.D. program. Additionally, I am profoundly thankful to my family for their unwavering encouragement and support. I also want to express my gratitude to Graduate School of Science, Osaka University for providing the resources and environment necessary for the successful completion of this thesis.

I would like to extend my appreciation to my fellow students and colleagues who provided support during the research process. I would like to thank Mrs. Ryoko Takeda for supporting on my research life.

Finally, I would like to express my gratitude to my best friends: Ms Fumi N. and Ms Midori Y. for their encouragement, understanding. And thanks to everyone who has helped me in my life.

Nov. 2023

Mao Komura

Table of Contents

List of Abbreviations 3

List of publications 4

Acknowledgement 5

Table of Contents 6

Chapter 1 General Introduction 8

1.1 General principles of phosphorescence 9
1.2 Room-temperature phosphorescence from metal-free organic compounds 10
1.3 The effect of desymmetrizing molecular structure on intermolecular interactions 12
1.4 Purpose of this study 13
1.5 References 14

Chapter 2 Room-temperature phosphorescence of a supercooled liquid: kinetic stabilization by desymmetrization 16

2.1 Introduction 17
2.2 Results and Discussion 19
2.2.1 Optical and rheological properties of liquid SO 19
2.2.2 Photophysical properties of SO in liquid state 20
2.2.3 Crystal structure and non-luminescence 26
2.2.4 Stability of the SCL and SCL-to-solid phase transition behavior 29
2.2.5 Glass transition of the SCL and the thermochromic behavior 32
2.3 Summary of Chapter 2 35
2.4 Experimental Section 35
2.4.1 Instrumentation and chemicals 35
2.4.2 Synthesis and characterization of liquid SO 36
2.4.3 Purity inspection of the measurement samples 43
2.4.4 Optical inspection of liquid SO 44
2.4.5 Photophysical properties in solution 45
2.4.6 Photophysical and structural properties of solid SO 46
2.4.7 Variable-Temperature PL measurement of the liquid SO 48

2.5 References and Notes 51

Chapter 3 Photoinduced Crystal Melting with Luminescence Evolution Based on Conformational Isomerization 54

3.1 Introduction 55
3.2 Results and Discussion 56
3.2.1 Real-time tracking of PCLT with luminescence evolution 56
3.2.2 Theoretical study on the conformational dynamics of SO 66
3.2.3 Correlation between crystal structure and PCLT 69
3.2.4 A plausible PCLT mechanism of SO crystal 81
3.3 Summary of Chapter 3 85
3.4 Experimental section 85
3.4.1 Instrumentation and chemicals 85
3.4.2 Details of the laboratory-built hyperspectral imaging system 86
3.4.3 Details of a home-built Raman microscope 87
3.4.4 Procedures for evaluating photoinduced crystal melting 87
3.4.5 Evaluating photoresponse before macroscopic melting 89
3.4.6 Theoretical study on the conformational dynamics of SO 92
3.4.7 Photoresponses and structures of analogous diketones 93
3.5 References and Note 95

Chapter 4 Conclusion 99

Chapter 1

General Introduction

1.1 General principles of phosphorescence

The phosphorescence is a luminescence that occurs during transitions between different spin multiplicities. The energy diagram (Jablonski diagram) in Figure 1.1 shows the representative photophysical processes. Typical organic compounds are in the singlet spin state at the ground state. A molecule that is excited by light absorption changes from the ground singlet state (S_0) to the excited singlet state (S_1), without changing the spin multiplicity. The molecule at S_1 state consumes excited energy via three different photophysical pathways. The radiative decay process to the S_0 state, called as fluorescence, converts the energy as luminescence. The non-radiative decay process to the S_0 state consumes the excess energy by either transferring to the solvent or surrounding molecules or by converting into molecular kinetic energy. The third pathway is a non-radiative transition to the excited triplet state (T_1). These three processes are characterized by rate constants, k_f, k_{nr}^S, and k_{ISC} respectively. In the zero-order approximation, a spin-flipping transition is forbidden. However, considering high-order perturbations such as spin-orbit coupling, the intersystem crossing (ISC) process can be allowed. The T_1 state typically returns to the ground state either through radiative decay (k_p) with phosphorescence, or through non-radiative decay (k_{nr}^T) without luminescence.

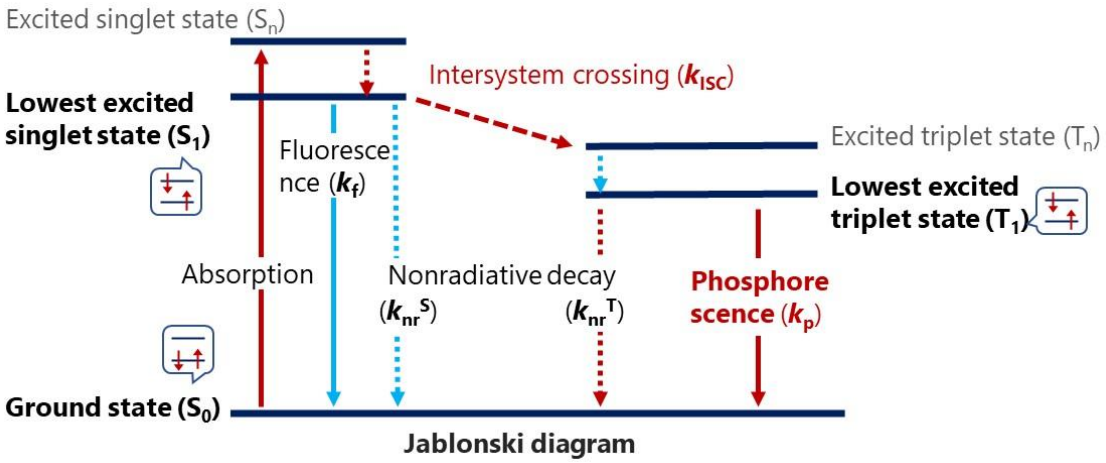

Figure 1.1. Simplified Jablonski diagram illustrating the different photophysical relaxation processes.

The luminescence quantum yield is expressed by the rate constants (k) for the photophysical processes involved. The phosphorescence quantum yield (Φ_p) is represented by equation (1), while the intersystem crossing quantum yield (Φ_{ISC}) is described by equation (2):[1]

$$\boldsymbol{\Phi_{\mathrm{p}}} = \boldsymbol{\Phi_{\mathrm{ISC}}} \frac{\boldsymbol{k_{\mathrm{p}}}}{\boldsymbol{k_{\mathrm{p}}} + \boldsymbol{k_{\mathrm{nr}}^{\mathrm{T}}}} \quad (1)$$

$$\boldsymbol{\Phi_{\mathrm{ISC}}} = \frac{\boldsymbol{k_{\mathrm{ISC}}}}{\boldsymbol{k_{\mathrm{f}}} + \boldsymbol{k_{\mathrm{nr}}^{\mathrm{S}}} + \boldsymbol{k_{\mathrm{ISC}}}} \quad (2)$$

To achieve efficient phosphorescence, it is necessary to increase Φ_{ISC} and k_{p} while reducing $k_{\mathrm{nr}}^{\mathrm{T}}$. The values of k_{p} are influenced by the molecular structure and electronic states such as the overlap of orbitals before and after the transition, the symmetry of the orbitals, and the energy gap between T_1 and S_0 states.[1] The value of $k_{\mathrm{nr}}^{\mathrm{T}}$ is related to the energy transfer to the solvent and surrounding molecules and to molecular motion.

ISC and T_1–S_0 transition are a spin-flip process. In the zeroth-order approximation, transitions that change the spin multiplicity are forbidden. However, when the energy difference between singlet and triplet states is small or spin-orbit coupling (SOC) is strong, a mixing of those states occurs, which allows the transition. SOC is the interaction between the magnetic moments of orbital angular momentum ($\boldsymbol{L}$) due to electron orbital motion and the magnetic moments of electron spin angular momentum ($\boldsymbol{S}$). For a single electron, the magnitude of SOC can be expressed with the following matrix:[1]

$$\langle \psi_{\mathrm{s}} | \hat{H}_{\mathrm{SOC}} | \psi_{\mathrm{f}} \rangle = \left\langle \psi_{\mathrm{s}} \middle| \frac{Ze^2}{2m^2c^2r^3} \boldsymbol{L} \cdot \boldsymbol{S} \middle| \psi_{\mathrm{f}} \right\rangle \quad (3)$$

The ψ_{s} and ψ_{f} represent the wave functions of the orbitals before and after the transition, respectively. Z is the atomic number, e is the electron charge, m is the electron mass, c is the speed of light in a vacuum, and r is the distance from the electron to the atomic nucleus. According to equation (3), when molecule has a heavy atom with a large atomic number, the SOC becomes significant (heavy atom effect). To increase the efficiency of phosphorescence, heavy atoms such as gold, platinum, iridium, or halogen atoms are often incorporated as part of the molecule.[1, 2, 3, 5]

Another strategy to increase SOC is based on molecular design following the El-Sayed rule.[1, 4, 6] The El-Sayed rule is a selection rule for ISC, describing that transitions between different types of orbitals are more likely to occur. For example, transitions from singlet states with (n,π*) configuration to triplet states with (π,π*) configuration are more likely to occur than transitions from singlet states with (π,π*) configuration to triplet states with (π,π*) configuration. Design guidelines for molecules with singlet states containing (n,π*) configuration include incorporating heteroatoms which have lone pair, like oxygen, sulfur, or tellurium into conjugated systems.[4]

1.2 Room-temperature phosphorescence from metal-free organic compounds

Phosphorescence at room-temperature, called as room-temperature phosphorescence (RTP), is a unique luminescence phenomenon. It is useful for a number of applications, including organic

light-emitting diodes (OLEDs), bio-imaging, and encryption inks and these mainly use precious-metal complexes of Ir or Pt.[5] Metal-free organic RTP materials are desirable owing to their cost-effectiveness and low environmental burden.[6] However, most organic RTP luminophores require to suppress non-radiative decay to obtain RTP.[7]

Crystallization is a promising approach to suppress non-radiative decay because it can suppress thermal deactivation due to molecular motion and prevent triplet quenching by oxygen due to lower air permeability than in solution.[8] Such phosphorescence is called as crystallization-induced phosphorescence (CIP) and actively researched in recent years since CIP of a benzophenone derivative was reported by Yuan *et al.* in 2010 (Figure 1.2).[8b] The benzophenone derivatives does not exhibit RTP in solutions or polymers under ambient conditions because of molecular motions such as rotation and vibration. However, they exhibit RTP in the crystalline state because the non-radiative decay is suppressed by intermolecular interactions within the crystal lattice. In addition, Gong *et al.* reported that several derivatives of benzil, a simplest aromatic 1,2-diketone, also exhibited CIP.[8d] However, the optical properties of crystalline materials are deteriorated by lattice defects.[9] Therefore, organic RTP materials that function in non-rigid and flexible molecular environments are desired.

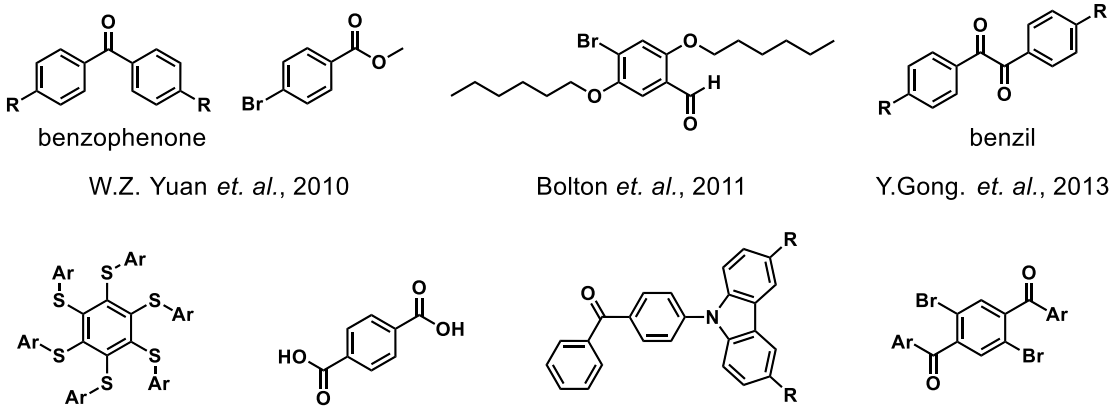

Figure 1.2. Chemical structures of compounds with CIP property[8]

Previously, I and my co-workers synthesized and developed metal-free organic thienyl diketone as a molecular flamework exhibiting efficient RTP in solution, polymer matrix, and amorphous solid states (Figure 1.3).[10] Unlike typical chromophores with rigid skeletons, the diketone skeleton is flexible, with many distinct conformers. Among them, a planar conformer is responsible for the efficient RTP in those states.[10] In particular, Φ_p of one derivative (Figure 1.3) in solution under Ar atmosphere is 38.2%, which is the highest value among metal-free organic compounds in common solvents. This exceptional performance is attributed to the large k_p of

thienyl diketone framework. Metal complexes that exhibit efficient RTP in solution states have large k_p (10^4–10^5 s^{-1}),[11] while only ~10 s^{-1} or less for metal-free organic compounds even with heavy atoms or carbonyl groups to facilitate ISC.[5, 6a] In contrast, the k_p of the thienyl diketone derivatives is approximately 5000 s^{-1} in cyclohexane, which is comparable to that of the platinum porphyrin complex with highly efficient RTP.[5d, 10c]

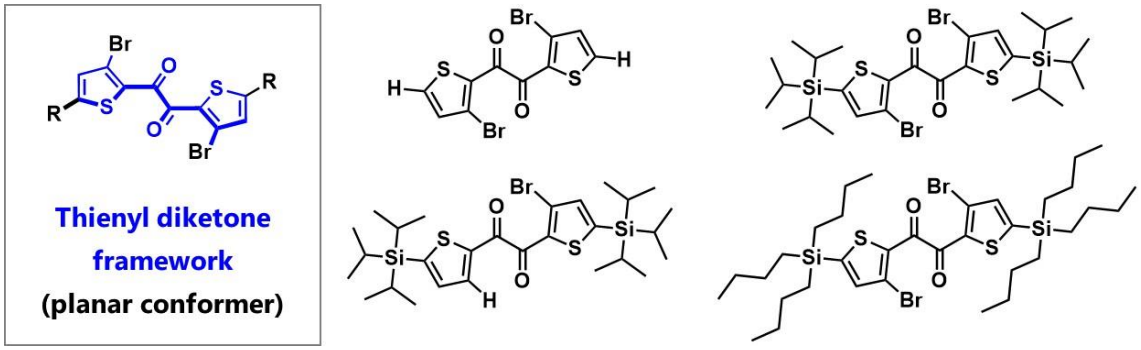

Figure 1.3. The chemical structures of thienyl diketone derivatives with efficient RTP properties in various states. Thienyl diketone framework is highlighted in blue.

1.3 The effect of desymmetrizing molecular structure on intermolecular interactions

Molecular symmetry is a crucial factor that affects the properties of molecular aggregates like crystals, and intermolecular interactions in the crystal is weakened by decreasing molecular symmetry.[12] Gavezzotti *et. al.* reported that para-isomers of aromatic hydrocarbons tend to have higher melting points compared to ortho and meta-isomers.[12c] This trend holds for several substituents, which related to the spatial distribution of the entire molecule rather than the chemical properties of their substituents. Based on these results, Brown and co-workers discussed that the molecules with higher symmetrical structure had a larger enthalpic change upon melting that implied stronger intermolecular interactions in the crystal resulted in higher melting points.[12d]

Previously, I synthesized an unsymmetrical diketone, by replacing one of the bromine atoms in the symmetrical thienyl diketone with a hydrogen atom (Figure 1.4).[10b] Both diketones formed the same skew conformation in the crystals. However, the unsymmetrical thienyl diketone did not exhibit luminescence while the green RTP from skew conformer observed in the symmetrical thienyl diketone. Based on the results of XRD analysis, I revealed that the intermolecular interactions were reduced in unsymmetrical thienyl diketone due to desymmetrization. Intermolecular interactions in a crystal generally contribute to the suppression of molecular motion. Therefore, I concluded that the unsymmetrical thienyl diketone crystal was non-emissive due to molecular motion in the crystal. In addition, the melting point of unsymmetrical thienyl diketone was dramatically lower than that of the symmetrical one due to reducing the

intermolecular interactions in the crystal. Notably, both compounds in the amorphous solid state exhibited yellow RTP that originated from a planar conformer. This implies that the desymmetrizing substitution of thienyl diketone does not significantly affect the RTP properties derived from planar conformations with large k_p while altering intermolecular interactions in the aggregated states.

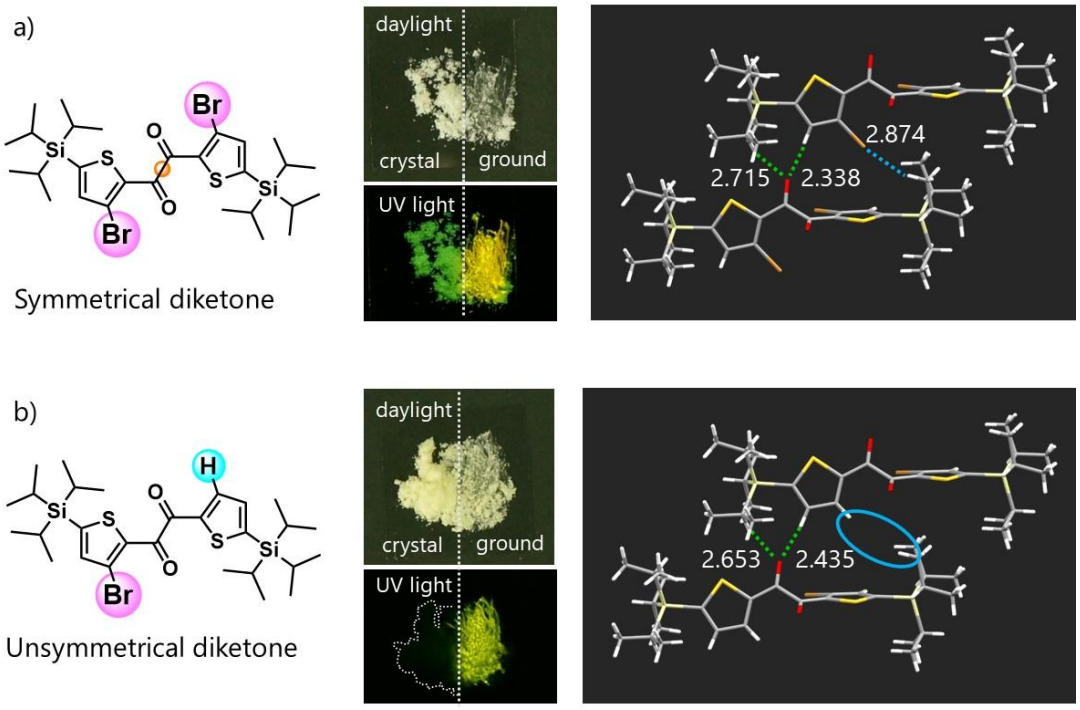

Figure 1.4. Chemicals structures, pictures under daylight and UV light, and crystal structures of a) symmetrical diketone and b) unsymmetrical diketone.

1.4 Purpose of this study

Conventional metal-free organic RTP molecules have been designed for the suppression of non-radiative decay. In contrast, thienyl diketone framework has large k_p and flexibility of structure. In addition, desymmetrizing substitution of thienyl diketone particularly affected on intermolecular interactions in a crystal. Herein, I envisioned that desymmetrizing thienyl diketone framework itself would lead to new properties that conventional molecules could not achieve, such as efficient RTP in a liquid state. Chapter 2 described RTP of unsymmetrical diketone in a supercooled liquid state. Chapter 3 described RTP of unsymmetrical diketone in a crystal and its photoresponse. Thus, the framework desymmetrization maintained its RTP while brought more pronounced effect on the thermal properties, thereby affording unique photofunction such as liquid RTP.

1.5 References

1. a) N. J. Turro, Modern Molecular Photochemistry, *University Science Books*, Sausalito, CA, 1991; b) T. Zhang, X. Ma, H. Wu, L. Zhu, Y. Zhao and H. Tian, *Angew. Chem., Int. Ed.* 2020, **59**, 11206–11216; c) G. Baryshnikov, B. Minaev and H. Ågren*, Chem. Rev.*, 2017, **117**, 6500–6537; d)
2. a) P. T. Chou and Y. Chi, *Chem. Eur. J.* 2007, **13**, 380-395; b) Q. Zhao, C. Huang and F. Li, *Chem. Soc. Rev.* 2011, **40**, 2508-2524; c) C. Fan and C, Yang, *Chem. Soc. Rev.* 2014, **43**, 6439-6469; d) C. P. Tan, Y. M. Zhong, L.N. Ji and Z. W. Mao, *Chem. Sci.* 2021, **12**, 2357-2367
3. a) N. S. e. Konstantin and A. B. Elena, *Physics-Uspekhi* 2005, **48**, 231; b) M. Kasha, *J. Chem. Phys*. 1952, **20**, 71-74; c) D. S. McClure, *J. Chem. Phys.* 1949, **17**, 905-913; d) D. R. Kearns and W. A. Case, *J. Am. Chem. Soc.* 1966, **88**, 5087-5097.
4. a) M. A. El‐Sayed, *J. Chem. Phys.*, 1964, **41**, 2462‐2467; b) W. Zhao, Z. He, J. W. Y. Lam, Q. Peng, H. Ma, Z. Shuai, G. Bai, J. Hao and B. Z. Tang, *Chem* 2016, **1**, 592–602.
5. S. Hirata, *Adv. Opt. Mater.* 2017, **5**, 1700116.
6. a) Kenry, C. Chen and B. Liu, *Nat. Commun*. 2019, **10**, 2111; b) A. D. Nidhankar, Goudappagouda, V. C. Wakchaure and S. S. Babu, *Chem. Sci.* 2021, **12**, 4216–4236; c) W. Shao and J. Kim, *Acc. Chem. Res*., 2022, **55**, 1573–1585.
7. a) D. B. Clapp, *J. Am. Chem. Soc.* 1939, **61**, 523–524; b) C. S. Bilen, N. Harrison and D. J. Morantz, *Nature* 1978, **271**, 235–237; c) W. Z. Yuan, X. Y. Shen, H. Zhao, J. W. Y. Lam, L. Tang, P. Lu, C. Wang, Y. Liu, Z. Wang, Q. Zheng, J. Z. Sun, Y. Ma and B. Z. Tang, *J. Phys. Chem. C* 2010, **114**, 6090–6099; d) Z. An, C. Zheng, Y. Tao, R. Chen, H. Shi, T. Chen, Z. Wang, H. Li, R. Deng, X. Liu and W. Huang, *Nat. Mater.* 2015, **14**, 685–690.; e) M. Baroncini, G. Bergamini, P. Ceroni and *Chem. Commun.* 2017, **53**, 2081–2093; f) A. Forni, E. Lucenti, C. Botta and E. Cariati, *J. Mater. Chem. C* 2018, **6**, 4603-4626.
8. a) C. R. Wang, Y. Y. Gong, W. Z. Yuan and Y. M. Zhang, *Chin. Chem. Lett.* 2016, **27**, 1184–1192; b) W. Z. Yuan, X. Y. Shen, H. Zhao, J. W. Y. Lam, L. Tang, P. Lu, C. Wang, Y. Liu, Z. Wang, Q. Zheng, J. Z. Sun, Y. Ma and B. Z. Tang, *J. Phys. Chem. C*, 2010, **114**, 6090–6099; c) O. Bolton, K. Lee, H.-J. Kim, K. Y. Lin and J. Kim, *Nat. Chem.* 2011, **3**, 205–210; d) Y. Gong, Y. Tan, H. Li, Y. Zhang, W. Yuan, Y. Zhang, J. Sun and B. Z. Tang, *Sci. China Chem.* 2013, **56**,1183–1186.
9. a) W. Zhao, Z. He and B. Z. Tang, *Nat. Rev. Mater.* 2020, **5**, 869–885; b) X. Ma, J. Wang and H. Tian, *Acc. Chem. Res.* 2019, **52**, 738–748; c) N. Gan, H. Shi, Z. An and W. Huang, *Adv. Funct. Mater.* 2018, **28**, 1802657.
10. a) Y. Tani, M. Komura and T. Ogawa, *Chem. Commun.,* 2020, **56**, 6810–6813; b) Y. Tani, M. Terasaki, M. Komura and T. Ogawa, *J. Mater. Chem. C*, 2019, **7**, 11926–11931; c) Y. Tani,

K. Miyata, E. Ou, Y. Oshima, M. Komura, M. Terasaki, S. Kimura, T. Ehara, K. Kubo, K. Onda and T. Ogawa, *ChemRxiv*, 2023.

11. a) A. Bouskila, B. Drahi, E. Amouyal, I. Sasaki and A. Gaudemer, *J. Photochem. Photobiol. A* 2004, **163**, 381-388; b) A. K. Bansal, W. Holzer, A. Penzkofer and T. Tsuboi, *Chem. Phys.* 2006, **330**, 118-129; c) A. Endo, K. Suzuki, T. Yoshihara, S. Tobita, M. Yahiro and C. Adachi, *Chem. Phys. Lett.* 2008, **460**, 155-157; d) J. R. Sommer, A. H. Shelton, A. Parthasarathy, I. Ghiviriga, J. R. Reynolds and K. S. Schanze, *Chem. Mater.* 2011, **23**, 5296-5304
12. a) Y. Shirota, T. Kobata, N. Noma, *Chem. Lett.* 1989, **18**, 1145–1148; b) E. Ueta, H. Nakano and Y. Shirota, *Chem. Lett.* 1994, **23**, 2397–2400; c) A. Gavezzotti, *J. Chem. Soc., Perkin Trans. 2* **1995**, *7*, 1399–1404; d) R. J. C. Brown and R. F. C. Brown. *J. Chem. Educ.* 2000, **77**, 724; e) R. Gao, P. Yuan, X. Zhang, S. Sang, X. C. Hang, H. Nan, C. Liu, C. Zhang, X. Gao, F. Chen, X. Guo and Z. K. Chen, *ACS Appl. Electron. Mater.* 2019, **1**, 1233–1242.

Chapter 2

Room-temperature phosphorescence of a supercooled liquid: kinetic stabilization by desymmetrization

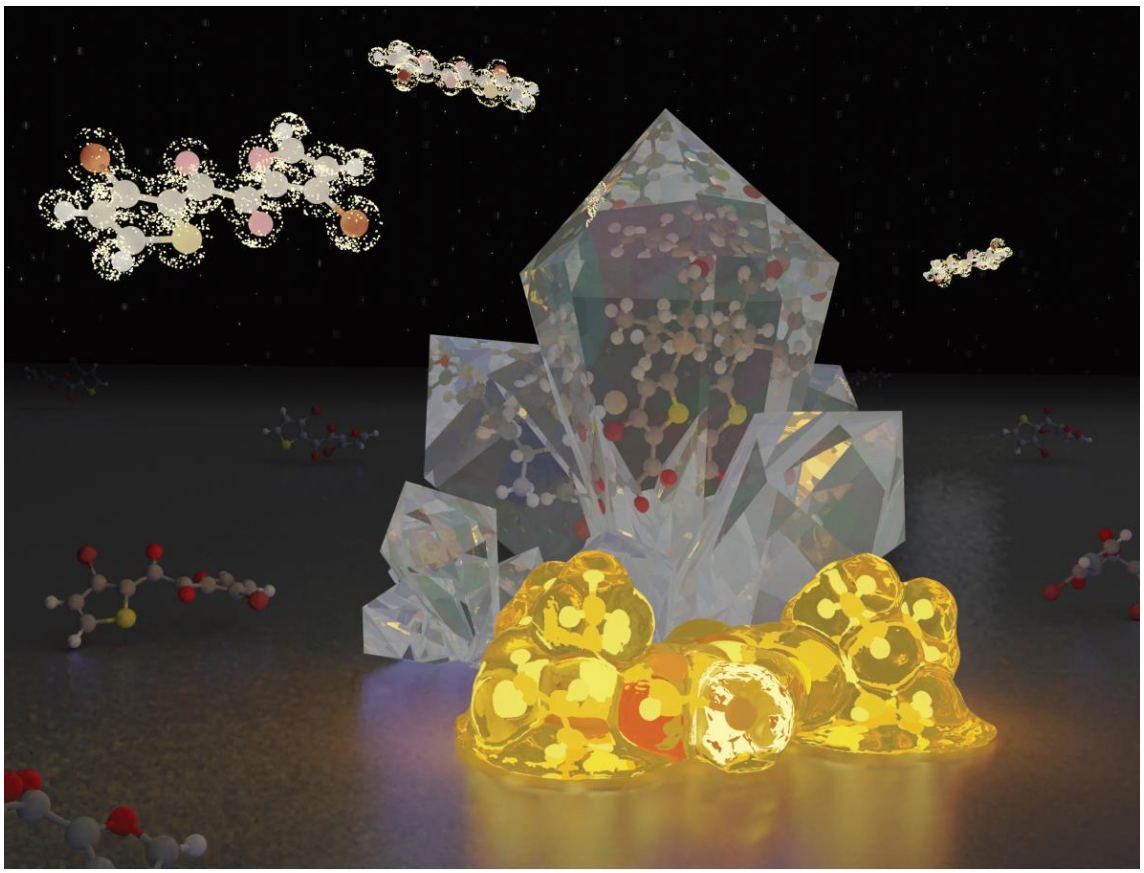

Selected as the inside front cover[I]

2.1 Introduction

The liquid state is the most flexible of condensed materials. Solvent-free liquid chromophores are advantageous because they are easily processed and, unlike solution- or polymer-based materials, can exploit high chromophore densities.[1] However, RTP is hardly observed in the liquid state, where molecules move more freely than in the solid state. To the best of my knowledge, only a pioneering two-component liquid system had been reported to show practical organic RTP before I reported this work.[2] Babu *et al.* demonstrated that the introduction of a long, branched alkyl chain onto a rigid bromonaphthalimide chromophore produces a solvent-free liquid that exhibits visible RTP when mixed with carbonyl compounds; however, the molecular liquid itself showed fluorescence-dominated emission with a faint RTP (Figure 2.1a). In addition, considering that a multicomponent (host-guest) system requires laborious optimization (*e.g.*, choices of host and guest, their ratio, and fabrication procedure), single-component molecular RTP liquids are more convenient and advantageous.[3,4]

I previously demonstrated that desymmetrizing C_2 symmetrical diketone **SS**—by replacing one bromine with hydrogen—reduced the intermolecular interactions in the crystals, dramatically lowered the melting point, and made the crystal non-emissive while maintaining the emissivity of the amorphous solid (Figure 2.1b).[5b] Consequently, the unsymmetrical diketone crystal showed, for the first time, turn-on RTP in response to mechanical stimuli in a metal-free organic molecule. These findings prompted us to expand the utility of the desymmetrization approach.[6]

In this work, I envisaged that desymmetrization provides a practical approach to achieving solvent-free liquid organic RTP (Figure 2.1c). Unsymmetrical furyl thienyl diketone **SO** was designed to combine the characteristics of two C_2-symmetrical diketones, namely the efficient RTP of **SS** and the low melting point of furyl diketone **OO**. Herein, I report that heteroaromatic 1,2-diketone **SO** exhibits RTP in the solvent-free liquid state. Diketone **SO** exists as kinetically stable supercooled liquid (SCL), which is reluctant to crystallize even in the presence of seed crystals or under mechanical stimulations. To my surprise, phosphorescence of **SO** responds in an unusual way to a disorder-order phase transition; the SCL exhibited RTP under air, while the solid state was non-emissive despite its crystallinity. Moreover, the liquid exhibits temperature-dependent phosphorescent color shift (*i.e.*, thermochromism) that follows the thermal phase behavior, including glass transition. These unique properties are attributed to the high conformational flexibility of **SO**, demonstrating the usefulness of phosphorescent molecular liquid with a flexible skeleton.

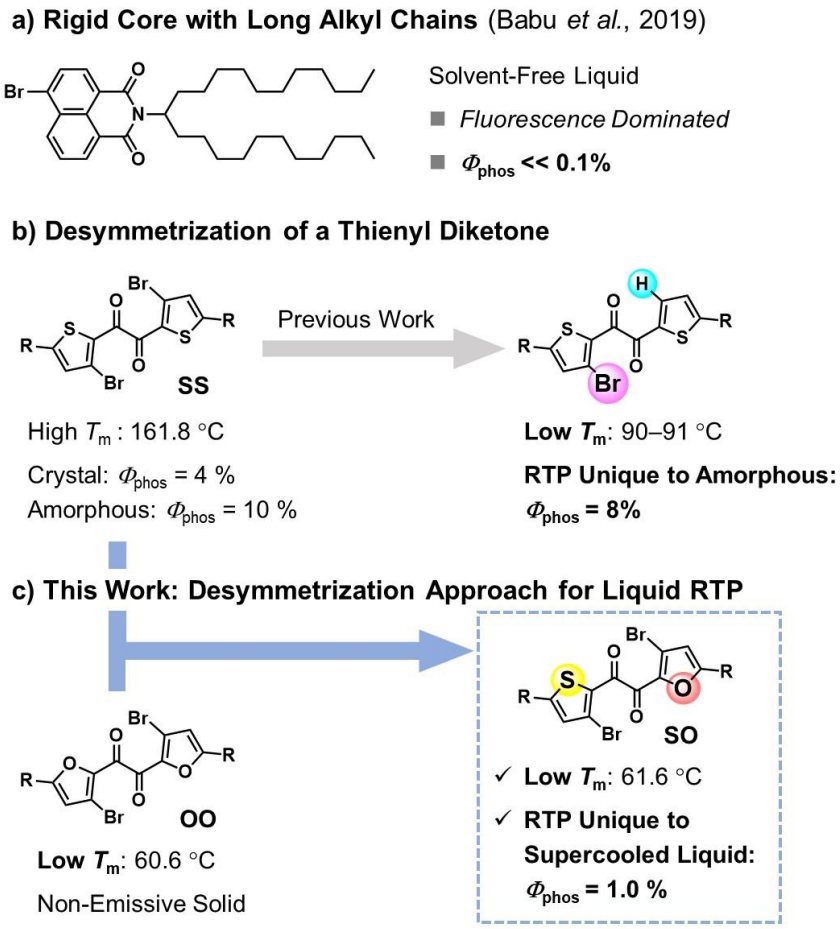

Figure 2.1. Strategy toward solvent-free liquid organic RTP. a) Introducing long alkyl chains into a rigid bromonaphthalimide chromophore. b, c) Desymmetrizing C_2-symmetrical thienyl diketones. The photographic image is of liquid **SO** taken in room light. R = triisopropylsilyl, T_m: melting point. Reproduced from ref I.

2.2 Results and Discussion

2.2.1 Optical and rheological properties of liquid SO

Diketone **SO** was synthesized by the cross-benzoin condensation of the corresponding aldehydes, followed by oxidation.[7] After purification, overnight solvent removal at reduced pressure and 40 °C afforded **SO** as a liquid (Figure 2.1c); as-prepared **SO** was confirmed to be pure and solvent-free by ^{1}H NMR and ^{13}C NMR spectroscopy, and elemental analysis. Further purity inspection was described in section 2.4.3. Liquid **SO** is isotropic, as confirmed by X-ray diffractometry (XRD) and visual inspection under a polarizing optical microscope (Figure 2.2 and Figure 2.18; vide infra). Rheology experiments were carried out on **SO** liquid and the zero-shear viscosity η_0 of liquid **SO** was determined to be 45 ± 2 Pa·s as an average of η' in the angular frequency range from 1 to 100 rad·s^{-1} (shear stress from 46 to 2615 Pa, Figure 2.3a). After the experiments, the sample was heated up to ca. 50 °C (below T_m, 59.5 °C), and then the upper plate was retracted. However, the sample remained as liquid (Figure 2.3b).

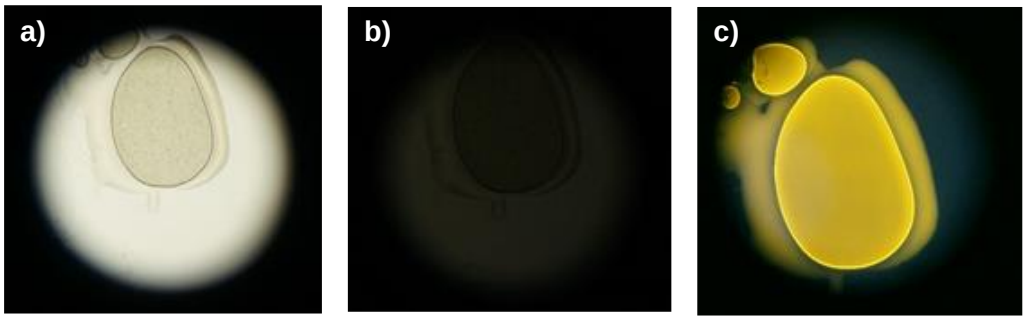

Figure 2.2. Polarizing optical microscope images of liquid **SO** with a) open Nichol prisms and b) crossed Nichol prisms. c) A fluorescence microscope image taken through U-MWUS mirror unit (Olympus, excitation; 330–385 nm, emission; >420 nm). Reproduced from ref I.

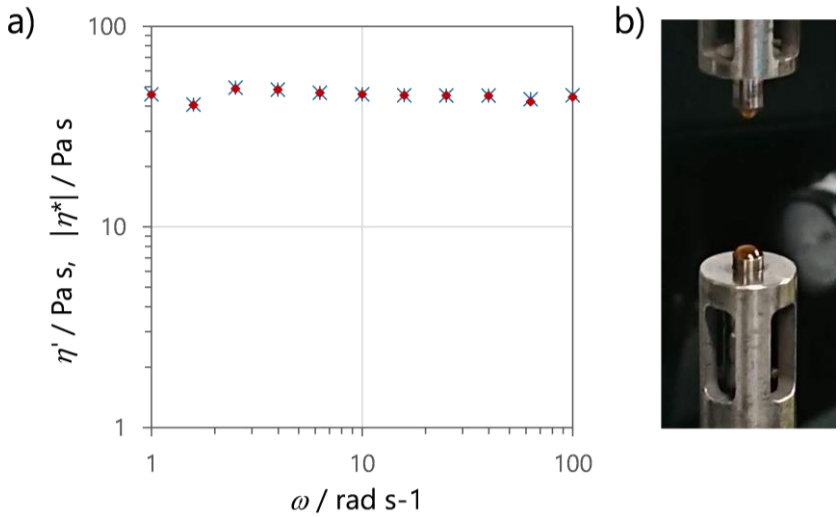

Figure 2.3. a) Variation of complex viscosity $|\eta^*|$ (blue asterisk) and its real part η' (red diamond) as a function of angular frequency ω for liquid **SO** under oscillatory shear deformation $\gamma = 1\%$ at 25 °C. b) A photographic image of liquid **SO** after the rheology experiments. Reproduced from ref I.

2.2.2 Photophysical properties of SO in liquid state

In air at room temperature, solvent-free liquid **SO** exhibited orange phosphorescence without discernible fluorescence (Figure 2.4 and Figure 2.5). Its steady-state photoluminescence (PL) spectrum exhibits an emission maximum at 574 nm with a PL lifetime of 16 μs, which does not include fast decay components in nanosecond order, consistent with phosphorescence-dominated emission without a detectable amount of fluorescence components. The Φ_p value was found to be 1.0%, which is the highest among single-component organic liquids.[2] The RTP of liquid **SO** likely originates from the planar conformer, whose T_1-optimised geometry is shown in Figure 2.6 and Figure 2.7. Density functional theory (DFT) calculations at the UB3LYP-D3/6–311G(d) level of theory suggest that the most stable conformer of **SO'** (in which the silyl groups in **SO** are replaced by H) in the lowest triplet state (T_1) is the planar conformer while it is the skew conformer in the ground state (S_0) (Figure 2.6, Figure 2.8, and Table 2.1). The PL and absorption spectra of liquid **SO** almost overlapped with that of **SO** in cyclohexane, indicating that the conformation of the emitting species in the excited state (T_1) and in the ground state (S_0) are similar in liquid and solution states (Figure 2.9 and Figure 2.10).[5] Therefore, **SO** exists mainly as a skew conformer and relax to a planar conformer after photoexcitation in solution, which is common behavior to aromatic 1,2-diketones (Figure 2.8).[8] I concluded from these results that the emissive conformer of **SO** in solvent-free liquid state is the planar conformer. Time-dependent (TD)-DFT calculations revealed that the T_1–S_0 radiative transition (phosphorescence) principally consists of the HOMO–LUMO transition (94%) with an electronic configuration with $^3(n,\pi^*)$ character, which

is favorable for spin.[8] Moreover, bromine atoms close to the carbonyl oxygen further promote phosphorescence by an intramolecularly directed heavy atom effect (Figure 2.6).[8]

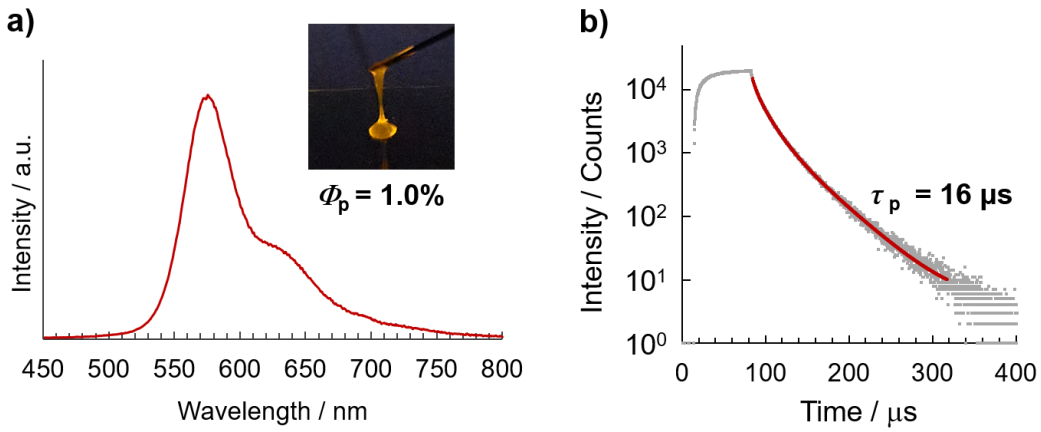

Figure 2.4. (a) Steady-state photoluminescence spectrum and (b) decay profile recorded at 570 nm of liquid **SO** in air at room temperature (λ_{ex} = 368 nm). Inset: photographic image of liquid **SO** when irradiated with UV light (365 nm). Absolute Φ_p was determined using an integrating sphere device. Reproduced from ref I.

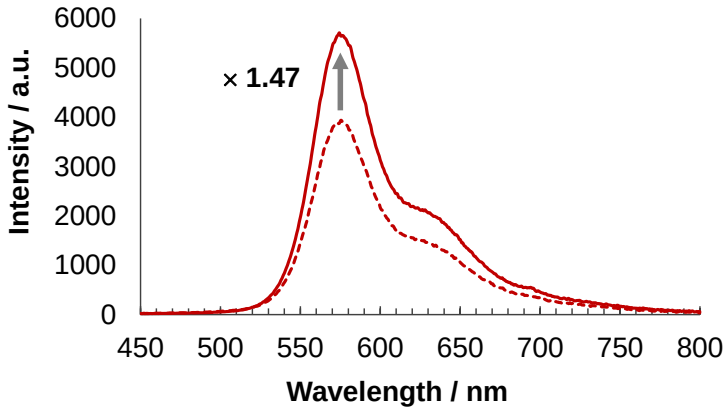

Figure 2.5. Steady-state PL spectra of liquid **SO** (dash line: in air, solid line: in N_2 atmosphere, λ_{ex} = 368 nm). Reproduced from ref I.

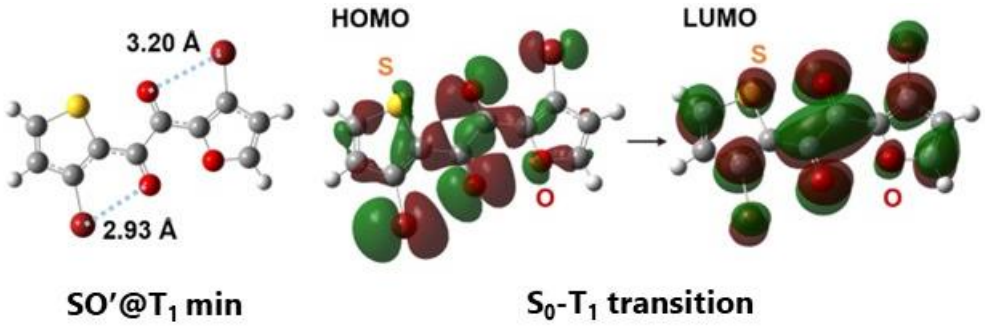

Figure 2.6. Geometry of T_1-optimized planar conformer of **SO′** and its Kohn–Sham HOMO and LUMO orbitals, calculated at the (TD-)UB3LYP-D3/6-311G(d) level of theory. Reproduced from ref I.

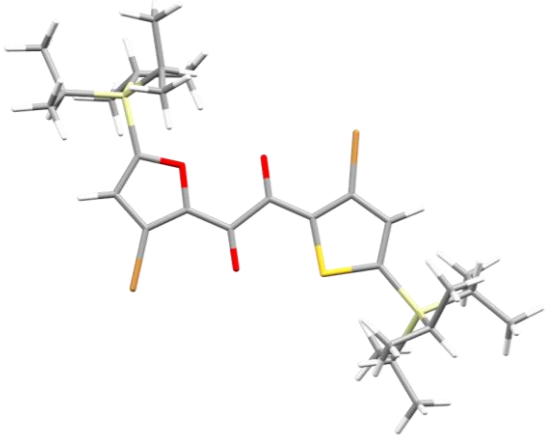

Figure 2.7. Optimized structure of **SO**-planar in the T_1 state calculated at the UB3LYP-D3/6-311G(d) level of theory. Reproduced from ref I.

Table 2.1. The relative Gibbs free energies (ΔG) of four conformers of **SO′** and the corresponding dihedral angles (θ) of the two carbonyls. The energies include thermal correction at 298.150 K. Reproduced from ref I.

	S_0 opt		T_1 opt	
	ΔG / kcal mol^{-1}	θ / °	ΔG / kcal mol^{-1}	θ / °
skew	0	97	3.87	166
skew′	0.91	95	5.60	159
skew″	1.74	123	2.64	168
planar	1.04	135	0	180

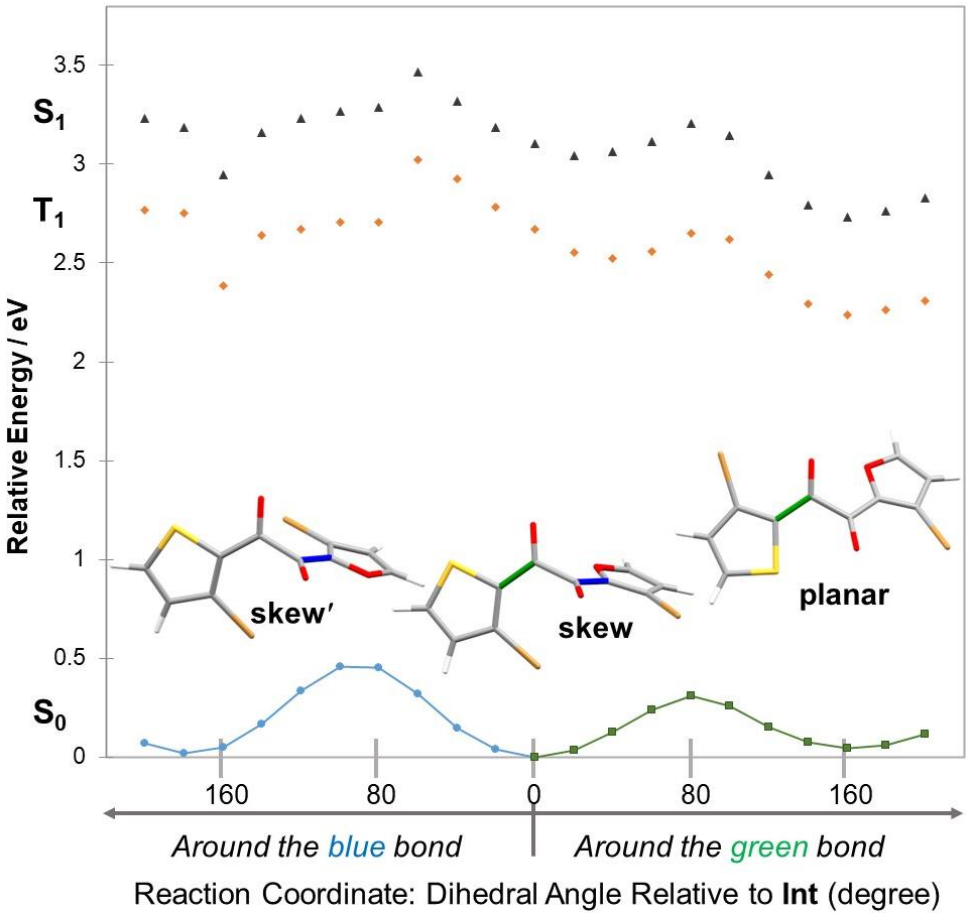

Figure 2.8. Potential energy curve of isolated (*S*)-**SO′** along the dihedral angles of the indicated bonds calculated at the B3LYP-D3/6-311G(d) level with a step of 20°. Energies for S_1 (black triangle) and T_1 states (orange diamond) were calculated for vertical excitation. Reproduced from ref I.

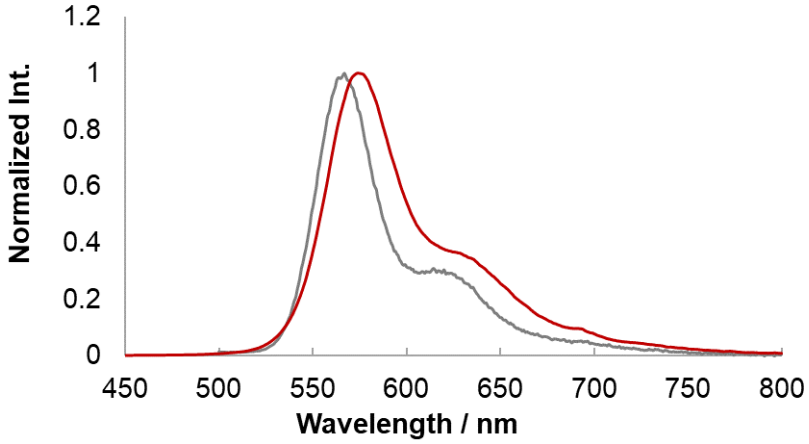

Figure 2.9. Normalized steady-state PL spectra of **SO** in cyclohexane (gray solid line, under Ar) and **SO** liquid (red solid line, under air). λ_{ex} = 368 nm. Reproduced from ref I.

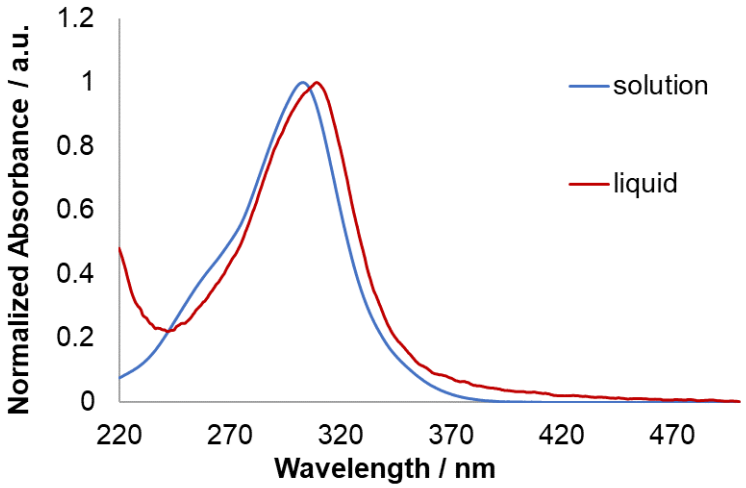

Figure 2.10. Normalized absorption spectra of **SO** in cyclohexane (blue) and liquid (red). Reproduced from ref I.

The RTP of **SO** was only visible in its solvent-free liquid state. In solution, **SO** was virtually non-emissive, even under Ar (Φ_p = 0.04%, 2.2 × 10^{-4} M in cyclohexane). The PL spectrum of solution-phase **SO** is in good agreement with that of the solvent-free liquid, which indicates that the emissive conformers are the same (*i.e.*, the planar conformer) for both states (Figure 2.9). However, the phosphorescence decay rate constants (k_p), which reflect molecular electronic properties, are significantly different (Table 2.2).[11] The liquid exhibits a k_p that is nearly 50-times larger than the solution, which implies that the external heavy atom effect from adjacent molecules contributes in the condensed solvent-free liquid.[8] To investigate the external heavy atom effect on the RTP of **SO**, the PL decay curves of **SO** in the degassed mixed cyclohexane and ethyl iodide solvents (5:1 and 11:1) were acquired. The area-weighted average lifetimes at 570 nm were confirmed to be shortened and approached that of the solvent-free liquid (16 μs) with increasing ethyl iodide proportion: 33, 27, and 22 μs for 1:0, 11:1, and 5:1 cyclohexane/ethyl iodide, respectively (Figure 2.13). These results suggest that the external heavy atom effect of ethyl iodide increased the rates of spin-forbidden processes, and the RTP of **SO** was indeed affected by external heavy atom effect. In contrast, the non-radiative decay rate constants (k_{nr}) of the solvent-free liquid in air and the degassed solution are not significantly different (Table 2.2). The RTP intensity of the liquid is only 1.47-times higher under N_2 (Figure 2.5), suggesting that the liquid is sufficiently viscus to retard oxygen diffusion, thereby suppressing phosphorescence quenching. In support, the zero shear viscosity of liquid **SO** is relatively high (η_0 = 45 ± 2 Pa·s at 25 °C, Figure 2.3).[1, 2, 13] Nonetheless, I emphasise that the RTP enhancement of liquid **SO** principally originates from an increase in k_p rather than a decrease in k_{nr}.

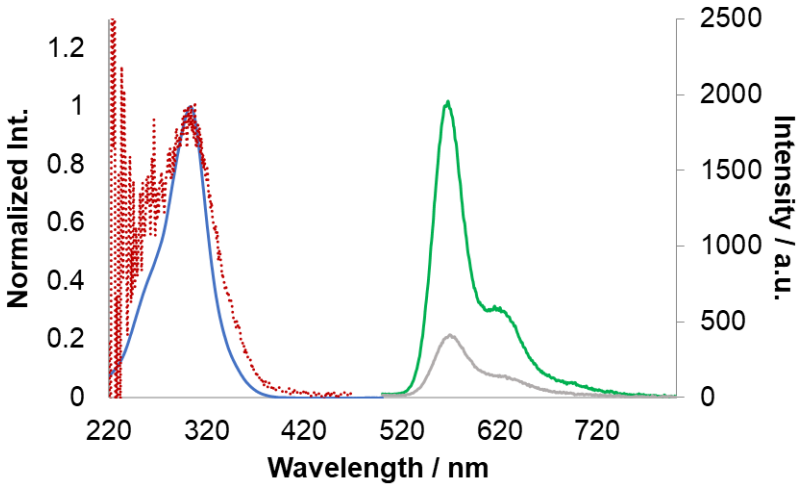

Figure 2.11. Absorption (blue solid line), excitation (red dot line, λ_{em} = 570 nm), and steady-state PL spectra (green solid line; Ar bubbling for 10 min, gray solid line; Air bubbling) of **SO** in cyclohexane (2.2×10^{-5} M for the absorption and excitation spectra, and 2.2×10^{-4} M for the PL spectrum). Reproduced from ref I.

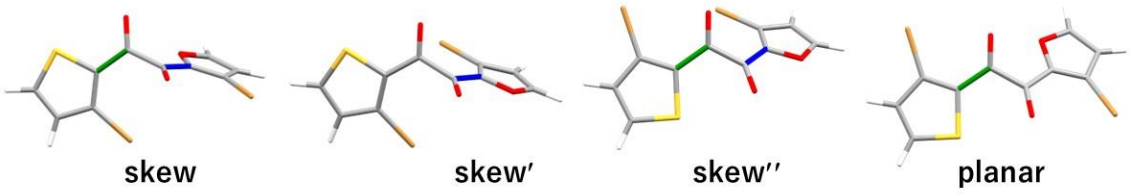

Figure 2.12. Optimized structures of (*S*)-**SO'** in the ground state. Reproduced from ref I.

Table 2.2. Photophysical properties of **SO** at room temperature. Reproduced from ref I.

	Φ_p	τ_p / μs	k_p / s^{-1}[a]	k_{nr} / s^{-1}[a]
Solvent-free liquid[b]	1.0%[c]	16	650	62000
Cyclohexane solution[d]	0.04%[e]	29	14	34000

[a] Calculated according to the formulas: $k_p = \Phi_p/\tau_p$ and $k_{nr} = (1 - \Phi_p)/\tau_p$. [b] In air. [c] Absolute Φ_p determined using an integrating sphere device. [d] 2.2×10^{-4} M under Ar. [e] Relative Φ_p determined using quinine sulfate as the standard.[12]

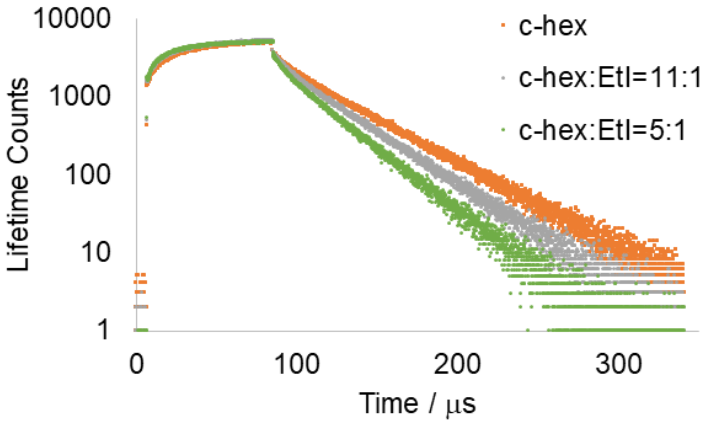

Figure 2.13. Photoluminescence decay curves of **SO** in 1:0, 11:1, and 5:1 cyclohexane/ethyl iodide (2.2×10^{-4} M) at RT under Ar. Reproduced from ref I.

2.2.3 Crystal structure and non-luminescence

Diketone **SO** remained liquid at room temperature for at least three months and eventually solidified. Surprisingly, the solid was non-emissive (Figure 2.14, see chapter 3 for detail of luminescence in a crystal state), although the crystalline nature of the solid was evident from the sharp diffraction peaks observed by powder XRD (Figure 2.15 , vide infra). Thus, **SO** exhibits efficient RTP only in the kinetically stable supercooled liquid (SCL) and is invisible either in solution or in the crystalline state. The observed liquefaction-induced RTP highlights the uniqueness of **SO**, considering that common organic RTP materials require rigid environments.[8, 14-16]

To my delight, a single crystal of **SO** suitable for X-ray structure analysis was obtained from a cooled MeOH solution. In the crystal, **SO** has a skew conformation with a vicinal-dicarbonyl dihedral angle of 83.7(7)° (Figure 2.16a). The powder XRD pattern simulated from the crystal structure was in good agreement with that of solid **SO** obtained by solidification of SCL (Figure 2.15). Therefore, the molecular arrangements and conformations in the solid and the single crystal are comparable. Symmetrical diketone **SS** exists in a skew conformation in the crystal; however, it exhibits RTP owing to more-rigid crystal packing.[5a] Previously, I created a non-emissive but isostructural crystal by desymmetrizing **SS** (Figure 2.1b), and revealed that intermolecular short-contacts involving Br atoms are crucial for the crystal of **SS** to exhibit RTP.[5b] The Br atoms as well as the entire furan moiety have no short contacts in **SO** crystal, which is disadvantageous for suppressing molecular motions (Figure 2.16b). The rather isolated Br atoms also suggest that the external heavy atom effect, likely present in the liquid, is diminispagehed owing to crystal packing (Figure 2.27). Moreover, Hirshfeld surface analysis (see the detail on page 47) of **SO** and **SS** was performed using CrystalExplorer software to compare the intermolecular interactions in the

crystals quantitatively.[17] An average normalized distance from nearest atoms is significantly longer for **SO** than **SS** (0.6468 vs. 0.5515 a.u., Figure 2.18), indicating weaker van der Waals interactions in crystalline **SO**. Such insufficient intermolecular interactions, as well as the absence of the highly emissive planar conformer, are responsible for the lack of emissivity of solid **SO**, despite its crystallinity.

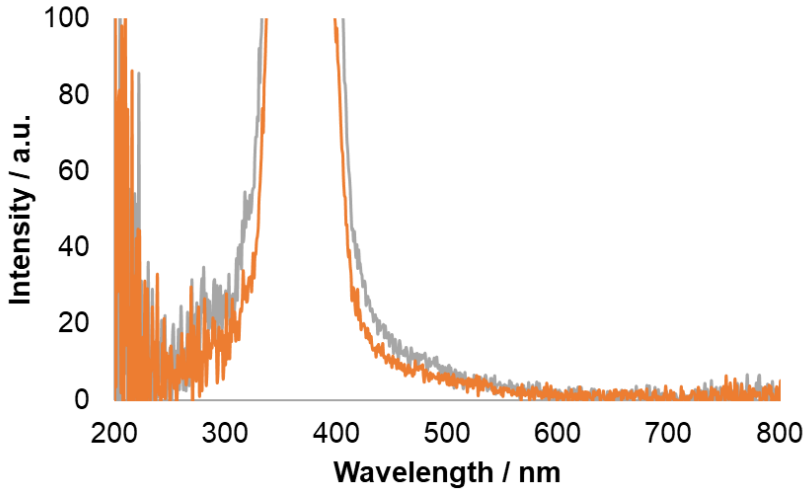

Figure 2.14. PL spectrum of solid **SO** measured using an integrating sphere (gray: blank, orange: solid sample, λ_{ex} = 368 nm). Reproduced from ref I.

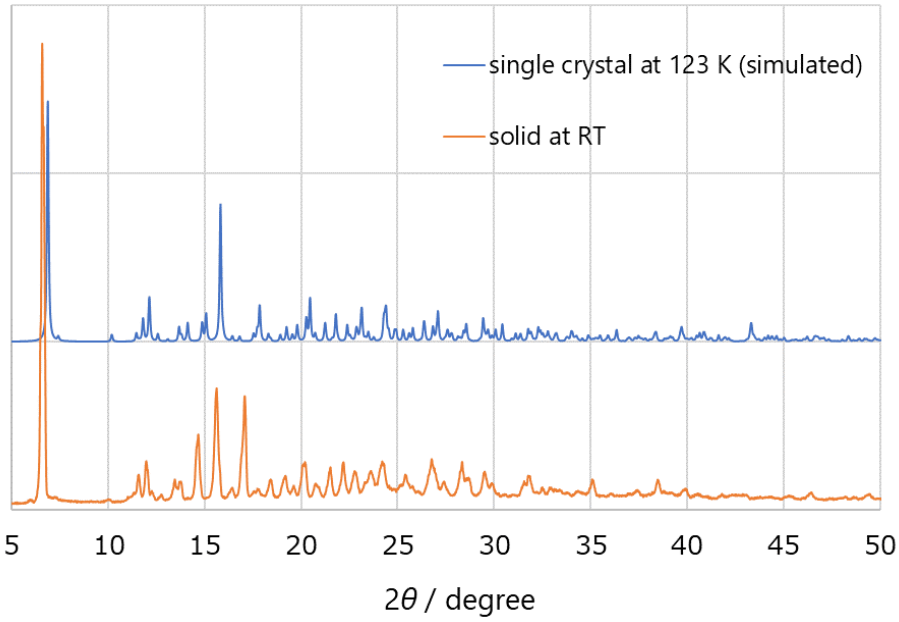

Figure 2.15**.** PXRD profiles of the single crystal of **SO** (simulated, blue line) and solid **SO** (orange line). Reproduced from ref I.

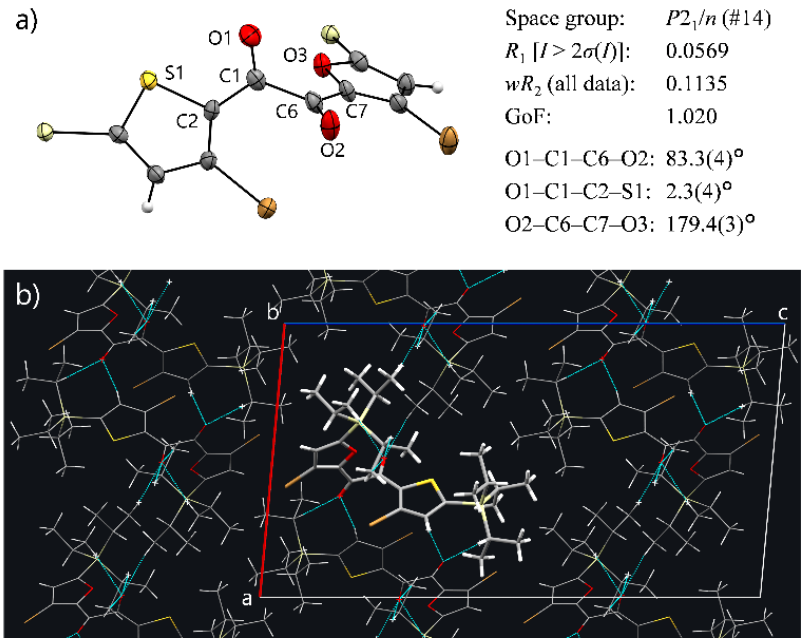

Figure 2.16. Single-crystal X-ray structure of **SO**. (a) ORTEP drawing and selected crystallographic parameters and angles. Isopropyl groups are omitted for clarity. Thermal ellipsoids are set at the 50% probability level. (b) Crystal packing seen along the *b* axis. The two Br atoms and the furan moiety have no short-contacts (dotted cyan lines). Reproduced from ref I.

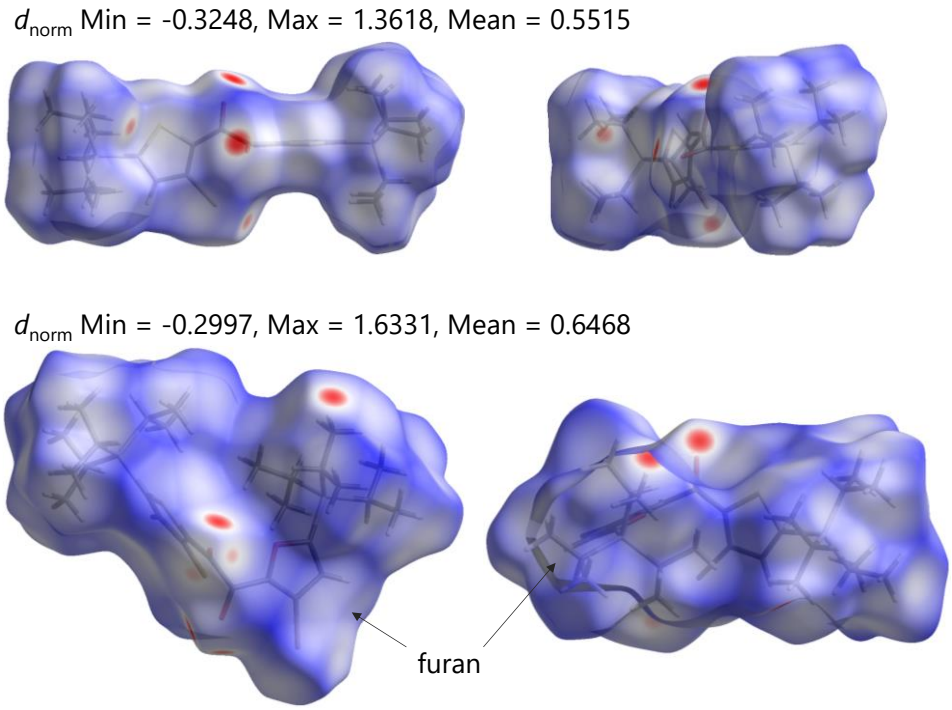

Figure 2.17. Hirshfeld surface of **SS** (top) and **SO** (bottom) mapped with d_{norm} (mapped over a fixed color scale of –0.3 (red) to 1.7 (blue)). The surfaces as well as the minima, maxima, and mean values of d_{norm} were obtained by CrystalExplorer21. Reproduced from ref I.

2.2.4 Stability of the SCL and SCL-to-solid phase transition behavior

To gain insight into molecular designs that lead to liquefaction, I compared the solid-liquid phase-transition behavior of the unsymmetrical diketone **SO** with those of symmetrical diketones **SS** and **OO**. The melting points of **SS**, **OO**, and **SO** are 161.8, 60.0, and 59.5 °C, respectively, which indicates that the thermodynamic liquid-phase stability of **SO** is similar to that of **OO**. Such a low melting point is beneficial for reactivating the RTP of **SO** by heating and for the application in turn-on-type thermosensors.[18]

In view of kinetic stability (*i.e.*, ease of crystallization from the SCL),[13a] **SS** instantaneously crystallizes upon evaporation of the solvent, while **OO** tends to solidify within a few days at room temperature. In contrast, SCL **SO** crystallizes significantly slowly. To monitor the solidification process using XRD (Figure 2.18), the well of a glass sample holder (20 × 20 × 0.2 mm^3) was filled with SCL **SO** and stored in a container at room temperature in air. At first, the liquid exhibited three broad diffraction peaks near 2θ values of 8.6, 14, and 25° (Figure 2.18, dark blue pattern). Tiny islands formed after three months, although no sharp peak was detected at that time. Even though solid **SO** was further scattered over the liquid after four months (seeding), the crystalline domains propagated slowly, taking six months in total for solidification of more than half of the area (Figure 2.18, dark orange pattern and the upper photographic image). Furthermore,

the SCL state was stable under mechanical stimulations, such as pricking with a needle (photographic images in Figure 2.1c and Figure 2.4a) or shear stress by a rheometer (high shear frequency up to 16 s^{-1} at 25 °C; Figure 2.3).[19] Therefore, the SCL state of the unsymmetrical diketone **SO** is obviously more stable than those of the symmetrical diketones. The above results demonstrate that desymmetrizing a molecular structure is a rational and promising approach to developing materials with highly stable SCL states. Thus, desymmetrization increases the number of (meta-) stable conformers within a 2 kcal·mol^{-1} energy range, from five for the symmetrical core of **SS** to eight for the unsymmetrical core of **SO**, as confirmed by DFT calculations (Figure 2.19, Figure 2.12, and Table 2.1). Moreover, the lack of C_2 symmetry provides an additional degree of freedom in relative molecular orientation. These features efficiently prevent nucleation and growth that form ordered molecular arrangements of crystals, which enhances the kinetic stability of the liquid state.

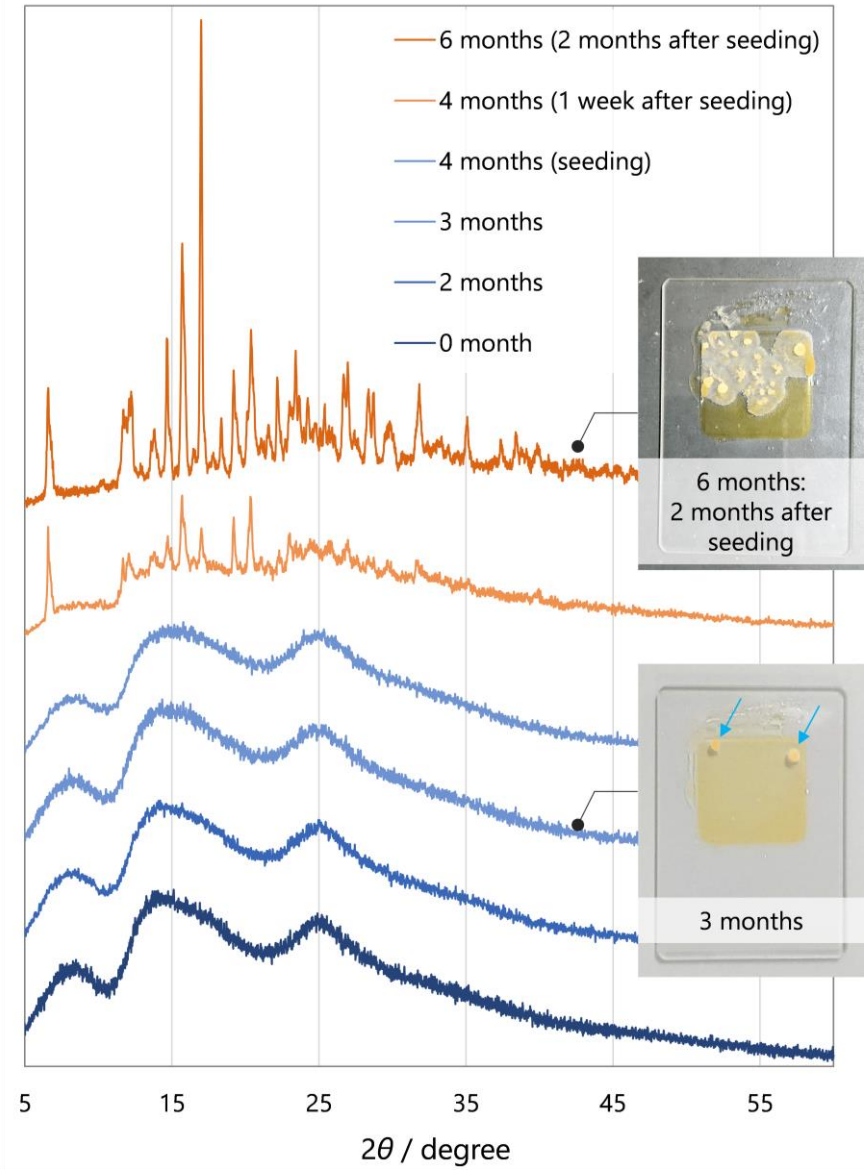

Figure 2.18. Crystallization time-course of **SO** followed by X-ray diffractometry. Inset: photographic images after three month (bottom) and six months (top). The blue arrows indicate small crystallized islands. Solid **SO** was scattered over the central region of the liquid after four months (seeding). Reproduced from ref I.

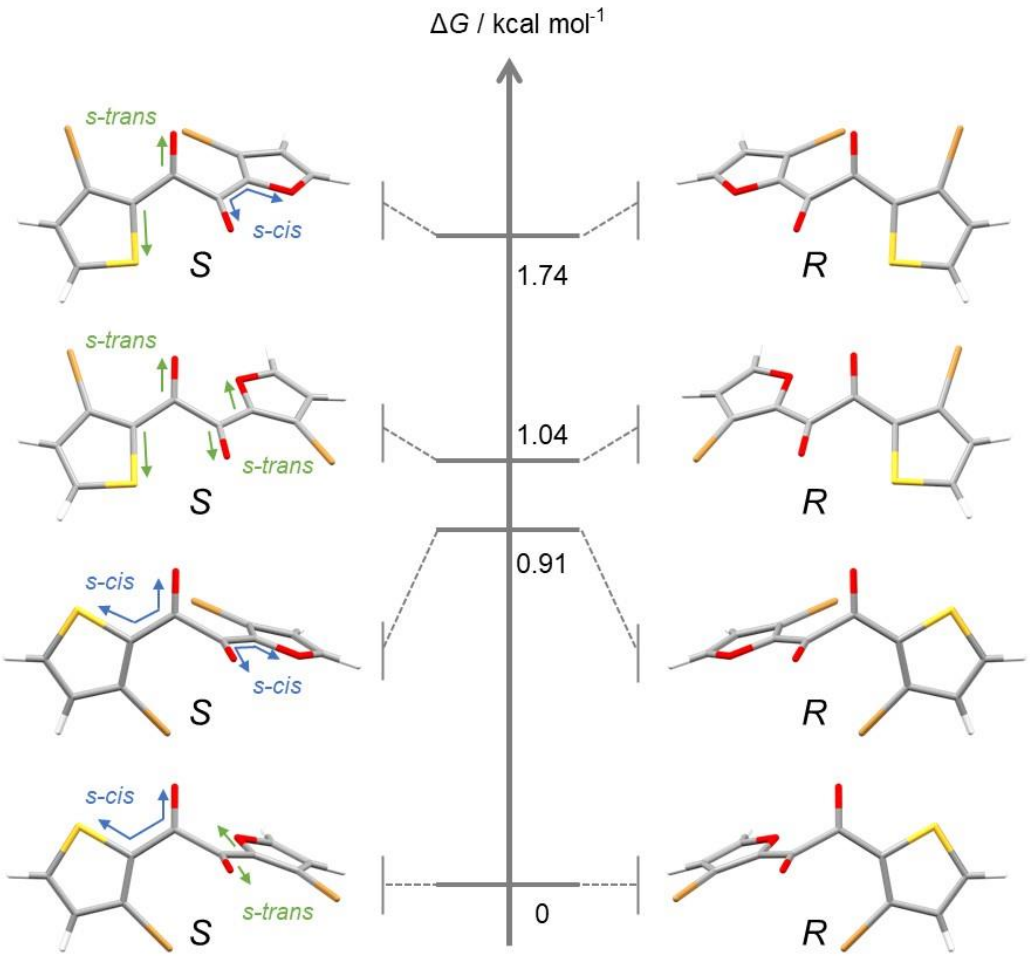

Figure 2.19. Optimized structures and energy levels of eight conformers of **SO′** in the S_0 state calculated at the B3LYP-D3/6-311G(d) level of theory. Reproduced from ref I.

2.2.5 Glass transition of the SCL and the thermochromic behavior

With a highly stable molecular SCL phosphor in hand, I investigated the temperature-dependence of its optical properties in the SCL and glass states, which revealed a PL spectral shift (*i.e.*, thermochromism) that correlates bulk thermal phase behavior with the microscopic molecular environment (Figure 2.20).[4,20] Steady-state PL spectra were acquired from –120 to 20 °C in 10 °C steps, which showed redshifts in the maximum emission wavelength (λ_{max}), from 566 nm to 574 nm. The increased intensity at a lower temperature without the emergence of new peaks is indicative of phosphorescence-dominated emission (Figure 2.21). The relationship between λ_{max} and reciprocal temperature can be fitted using two lines, with the slope changing between –10 and –30 °C. Note that crystallization was not observed by differential scanning calorimetry (DSC) even at a very slow cooling/heating rate of 0.3 °C·min^{-1}, which is another indication of the high stability of the SCL state (Figure 2.20c). Instead, DSC revealed that **SO** has a glass-to-isotropic

liquid-transition temperature (T_g) of –15.7 °C, which is close to where the two lines in Figure 2.20b intersect. Therefore, the phosphorescence wavelength of liquid **SO** responds to a bulk physical property (such as viscosity) that discontinuously changes at T_g.[21] The increase in viscosity prevents surrounding molecules from reorganizing as the dipole of the excited molecule changes, which I consider to be the reason for SCL/glass **SO** exhibiting thermochromic behavior (Figure 2.21). Although the peak shift is subtle for practical application, to the best of my knowledge, this is the first example of the phosphorescence thermochromism of a single-component organic liquid, whose performance will be improved on the basis of the above working hypothesis.

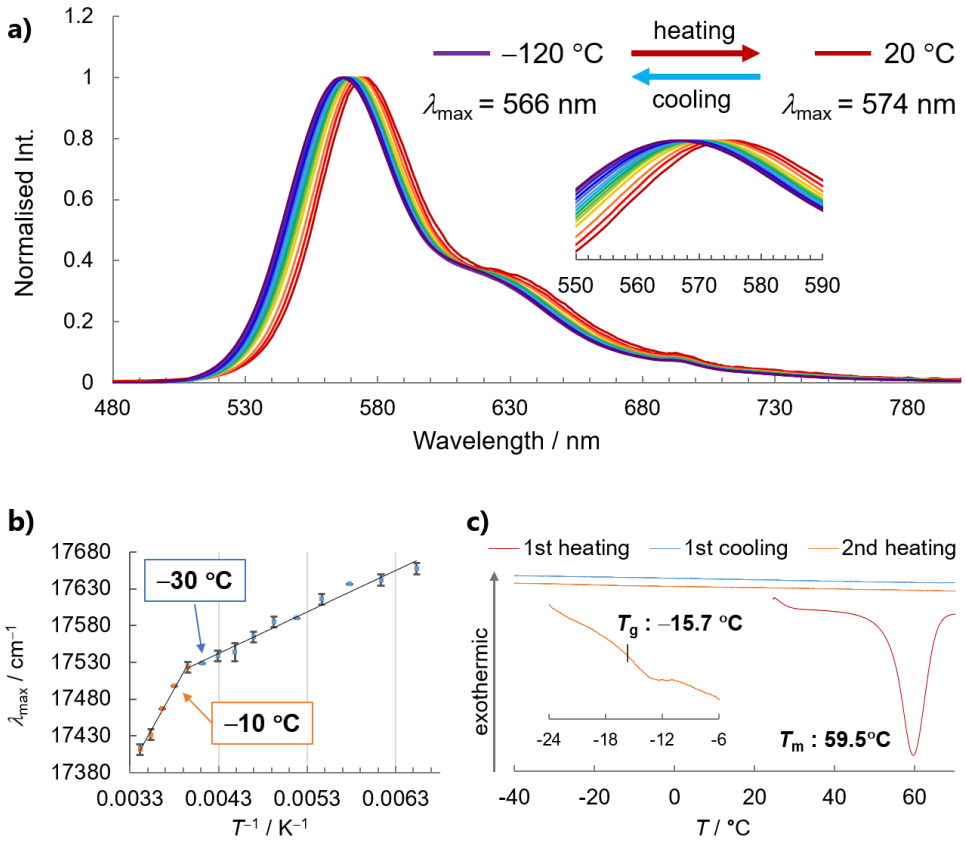

Figure 2.20. Thermochromic behavior of liquid **SO**. a) Steady-state PL spectra acquired from −120 to 20 °C in 10 °C steps. b) Relationship between λ_{max} and reciprocal temperature. The error bars were constructed from three independent measurements. c) DSC thermograms of solid **SO** during heating/cooling cycles at 10 °C·min^{-1} for the 1st heating and at 0.3 °C·min^{-1} for the 1st cooling and 2nd heating processes, under a flow of N_2. Reproduced from ref I.

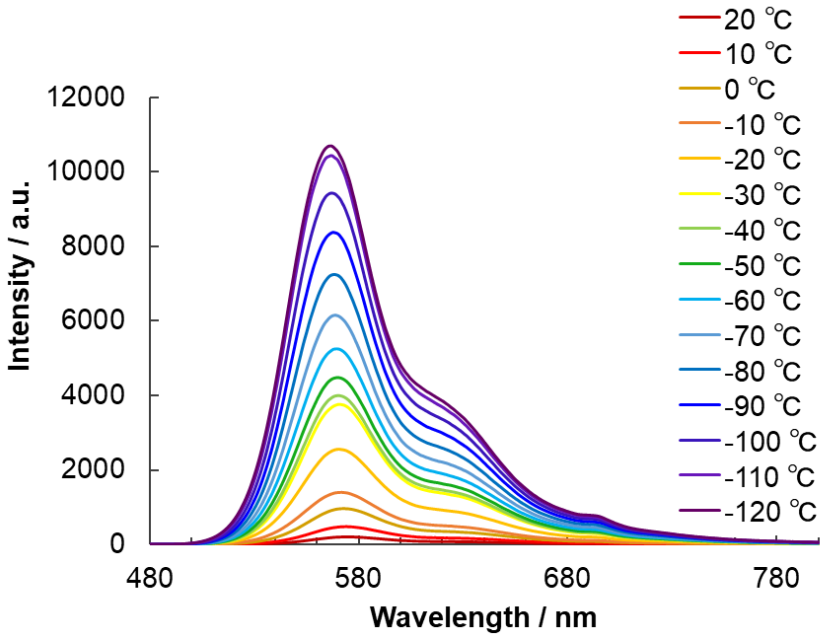

Figure 2.21. Steady-state PL spectra of liquid **SO** acquired from –120 to 20 °C in 10 °C steps. Reproduced from ref I.

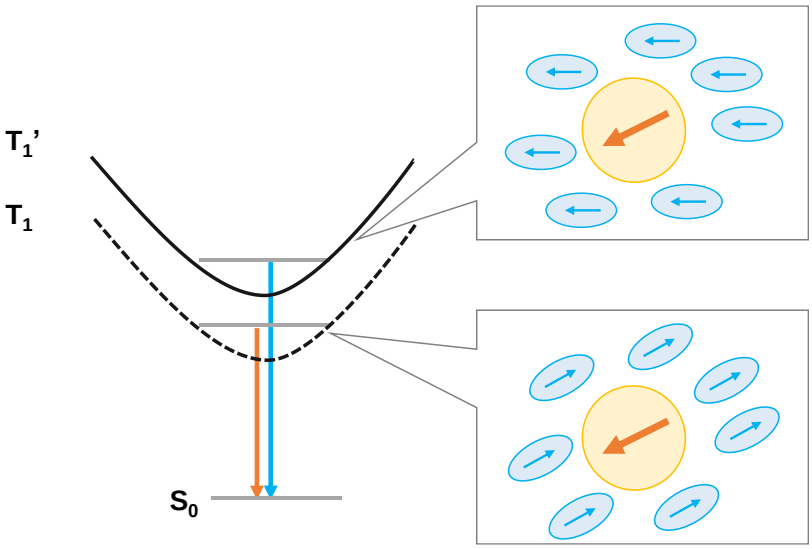

Figure 2.22. Schematic representations explaining the thermochromic phosphorescence: blue shift at low-temperature. At RT (broken curve, T_1), the surrounding molecules (blue circles) reorganize to stabilize the dipole of the excited molecule (yellow circle). At low temperature, the reorganization was prevented owing to an increased viscosity, which results in the emission from a higher energy (solid curve, T_1'). Reproduced from ref I.

2.3 Summary of Chapter 2

Efficient RTP in a solvent-free liquid state in air was realized through desymmetrizing a C_2-symmetrical thienyl diketone. The unsymmetrical flexible core kinetically stabilized the SCL state even in the presence of seed crystals or under pricking or shearing stresses. Notably, only the liquid exhibits RTP; the solution and crystalline solid are virtually non-emissive. I suggest that the liquid is sufficiently dense to benefit from the intermolecular (external) heavy atom effect and suppress oxygen diffusion, while being sufficiently flexible to generate an intrinsically emissive planar conformer. In addition, the unsymmetrical diketone exhibits thermochromic phosphorescence, which stems from its fluidity. This work demonstrates the significance of an unsymmetrical flexible core for realizing RTP in a condensed, yet loose liquid state. Investigations into the use of the SCL solid-phase transition with the aim of developing stimuli-responsive RTP is currently ongoing in our laboratory.

2.4 Experimental Section

2.4.1 Instrumentation and chemicals

Unless otherwise noted, all the reactions were performed under a nitrogen atmosphere using anhydrous solvents and heat-gun-dried glassware on a dual-manifold Schlenk line. ^{1}H and ^{13}C{^{1}H} NMR spectra were recorded on a JEOL ECS400 spectrometer. Chemical shift values (δ) are reported in ppm and are calibrated to tetramethylsilane (0.00 ppm) or residual solvent (7.26 ppm in $CDCl_3$) for ^{1}H, and to $CDCl_3$ (77.0 ppm) for ^{13}C NMR. Melting points were measured using a Hitachi NEXTA DSC200 or a Rigaku Thermo Plus EVO II under a flow of nitrogen at a heating rate of 10 °C min^{-1}. High-resolution mass spectra (ESI-HRMS) were obtained with a Thermo Fisher Scientific LTQ Orbitrap XL mass spectrometer. Elemental analysis (EA) was conducted on a Yanaco MT-6 recorder.

Analytical thin-layer chromatography (TLC) was performed on aluminum plates bearing a layer of Merck silica gel 60 F_{254}. Column chromatography was carried out on silica-gel 60 (Kanto Chemical Co., Inc., spherical, 63–210 μm). Gel permeation chromatography (GPC) was performed using a JAI LC-9130 NEXT equipped with JAIGEL-1HR and 2HR (eluent: $CHCl_3$, flow rate: 10 mL/min).

Anhydrous tetrahydrofuran (THF) and CH_2Cl_2 were purchased from Wako Chemical and Kanto Chemical, respectively, and further purified by passage through activated alumina under positive nitrogen pressure as described by Grubbs et al.[22] Unless otherwise noted, chemicals obtained from commercial suppliers were used without further purification. 2-(Pentafluorophenyl)-6,7-dihydro-5*H*-pyrrolo[2,1-*c*][1,2,4]triazol-2-ium tetrafluoroborate (**S2**), 1,2-bis[3-bromo-5-(triisopropylsilyl)thiophen-2-yl]ethane-1,2-dione (**SS**), and 1,2-bis[5-

(triisopropylsilyl)furan-2-yl]ethane-1,2-dione (**OO**) were synthesized according to the literatures.[23]

All the photophysical properties (*i.e.*, UV-vis absorption, photoluminescence (PL), and excitation spectra, PL quantum yields (PLQYs), and PL lifetimes) were obtained at room temperature (RT) under air unless otherwise noted. UV-vis absorption and PL spectra of solutions were acquired using a Shimadzu UV-3150 spectrometer and a JASCO FP-8200 spectrofluorometer, respectively. Solid- and liquid-state PL spectra were obtained using a JASCO FP-8200 spectrofluorometer. PLQY of a solution of **3** was determined by the relative method using quinine sulfate as a standard[12] using a JASCO FP-8200 spectrometer. PLQYs of **3** liquid and solid were determined by the absolute method using a Hamamatsu photonics C9920-02 spectrometer with an integrating sphere. PL lifetime measurements for liquid, solid, and a solution were performed using a HORIBA DeltaFlex multichannel scaling system using DeltaDiode for excitation (368 nm). Powder X-ray diffraction (PXRD) patterns were collected on a Rigaku MiniFlex600 with CuKα radiation (λ = 1.5418 Å) using D/teX Ultra as a detector.

2.4.2 Synthesis and characterization of liquid SO

2.4.2.1 Synthetic procedures

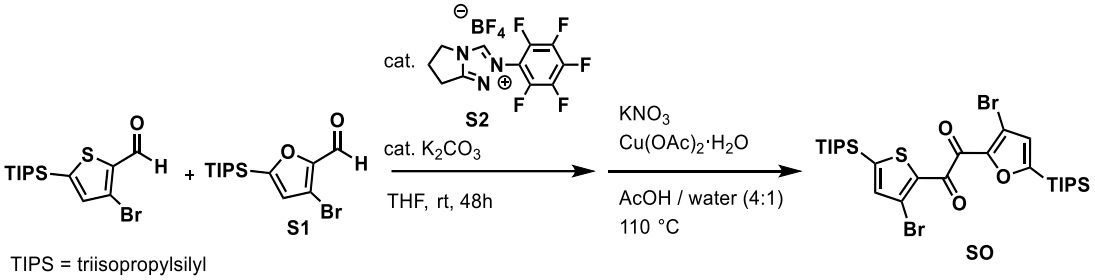

Scheme 2-1. Synthesis of **SO**.

3-Bromo-5-(triisopropylsilyl)furan-2-carbaldehyde (S1)

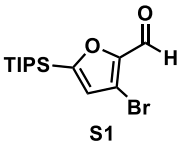

Aldehyde **S1** was synthesized according to a literature with a modified procedure.[23] To a 50 mL 2-neck flask were added diisopropylamine (2.1 mL, 15 mmol) and anhydrous THF (7.5 mL), and cooled to −30 °C. To the stirred mixture was added *n*-butyllithium (BuLi, 2.65 M in hexane, 4.5 mL, 12 mmol), and the stirring was continued for 10 min at −30 °C and 10 min at 0 °C. To the mixture was added a solution of potassium *tert*-butoxide (1.12 g, 10 mmol) in THF (16 mL), and then the resulting mixture was cooled to −78 °C and stirred for 10 min. 2-Bromo-5-(triisopropylsilyl)furan (3.05 g, 10 mmol), synthesized according to a literature,[5, 24] was dissolved in anhydrous THF (10 mL) and was added to the mixture. The temperature was reached to –58 °C while stirring for 1 h, during which the solution color turned to slight orange. Then, to the solution was added *N*,*N*-

dimethylformamide (1.2 mL, 15 mmol) dropwise. The reaction mixture was warmed up to RT, stirred for 15 minutes, and then quenched by adding water and extracted with Et_2O three times. The combined organic layers were dried over $MgSO_4$, filtered, and then evaporated. The residue was purified by silica-gel column chromatography (hexane/CH_2Cl_2 = 3:1) to give **S1** (1.743 g, 53%) as a light-yellow liquid. **^{1}H NMR** (400 MHz, $CDCl_3$) δ: 9.75 (s, 1H), 6.83 (s, 1H), 1.40-1.33 (m, 3H), 1.12 (d, *J* = 7.2 Hz, 18H). **^{13}C NMR** (100 MHz, $CDCl_3$) δ: 175.96, 166.22, 151.37, 126.52, 111.92, 18.27, 10.72. **ESI-HRMS** (*m*/*z*): $[M+Na]^+$ calcd for $C_{14}H_{23}BrO_2SiNa$, 353.0543; found, 353.0511.

1-(3-Bromo-5-(triisopropylsilyl)furan-2-yl)-2-(3-bromo-5-(triisopropylsilyl)thiophen-2-yl)ethane-1,2-dione (SO)

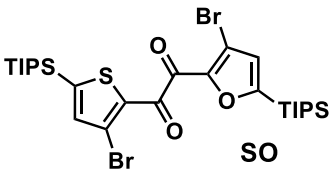

SO

Unsymmetrical diketone **SO** was synthesized via the cross-benzoin condensation and oxidation with a modified proccedure.[5, 25] To a Schlenk tube were added K_2CO_3 (6.0 mg, 0.04 mmol) and triazolium salt **S2** (15.3 mg, 0.04 mmol), and the tube was shortly evacuated and backfilled with N_2 three times. THF (1.0 mL) was added via a syringe and the suspension was stirred for 15 minutes. To the pale red suspension were added **S1** (0.35 g, 1.06 mmol) and 3-bromo-2-formyl-5-(triisopropylsilyl)thiophene[5] (0.791 g, 2.11 mmol) in THF (0.5 mL) under a flow of N_2. The mixture was stirred for 48 h at RT, and then quenched by adding water. The organic layer was separated and the aqueous layer was extracted with Et_2O. The combined organic extracts were dried over $MgSO_4$, filtered, and then evaporated. The residue was purified by silica-gel column chromatography (hexane/CH_2Cl_2 = 1:1). Then, to a Schlenk tube were added the obtained benzoins, KNO_3 (134 mg, 1.32 mmol), $Cu(OAc)_2{\cdot}H_2O$ (15 mg, 0.074 mol), and AcOH/H_2O (4:1, 5.0 mL). The mixture was stirred for 2 h at 110 °C. After cooling to RT, the reaction was quenched by adding H_2O and CH_2Cl_2. The organic layer was separated and the aqueous layer was extracted with CH_2Cl_2 three times. The combined organic extracts were dried over $MgSO_4$, filtered, and then evaporated. The residue was purified by silica-gel column chromatography (hexane/CH_2Cl_2 = 2:1). Evaporation of the solvents afforded **SO** (397 mg, 55%) as an orange oil. The oil was eventually solidified to a white powder. **m.p.** 59.5 °C. **^{1}H NMR** (400 MHz, $CDCl_3$) δ: 7.20 (s, 1H), 6.87 (s, 1H), 1.40-1.33 (m, 3H), 1.28-1.21 (m, 3H), 1.11 (d, *J* = 7.2 Hz, 18H), 1.03 (d, *J* = 7.2 Hz, 18H). **^{13}C NMR** (100 MHz, $CDCl_3$) δ: 184.07, 179.89, 167.01, 149.71, 148.61, 140.27, 138.78, 127.73, 118.36, 110.79, 18.34, 18.27, 11.50, 10.73. **EA** Calcd for $C_{28}H_{44}Br_2O_3SSi_2$: C, 49.70; H, 6.55. Found: C, 49.79; H, 6.58.

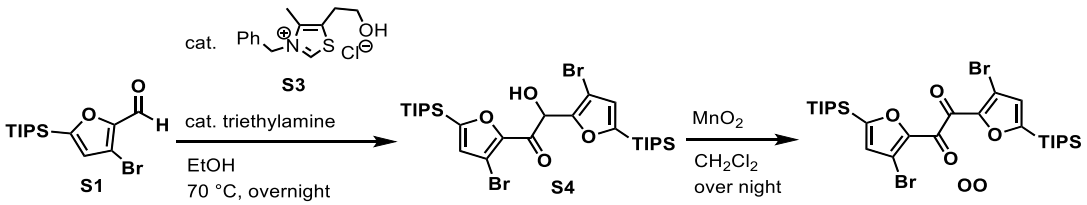

Scheme 2-2**.** Synthesis of **OO**

1,2-Bis(3-bromo-5-(triisopropylsilyl)furan-2-yl)-2-hydroxyethan-1-one (S4)

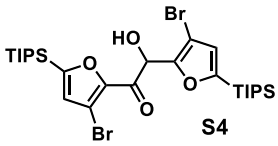

To a Schlenk tube were added **S1** (0.331 g, 1.0 mmol), thiazolium salt **S3** (14.3 mg, 0.05 mmol), and EtOH (1.0 mL). The tube was shortly evacuated and backfilled with N_2 three times, after which triethylamine (10 μL, 0.07 mmol) was added. The mixture was stirred at 70 °C overnight, and then quenched at RT by adding sat. NH_4Cl aq. The organic layer was separated and the aqueous layer was extracted with CH_2Cl_2 three times. The combined organic extracts were dried over $MgSO_4$, filtered, and then evaporated. The residue was purified by silica-gel column chromatography (hexane/CH_2Cl_2, 1:1) to give **S4** (0.24 g, 72%) as a colorless oil. **^{1}H NMR** (400 MHz, $CDCl_3$) δ: 6.77 (s, 1H), 6.59 (s, 1H), 5.91 (d, J = 4.8 Hz, 1H), 4.31 (d, J = 5.5 Hz, 1H), 1.39-1.24 (m, 3H), 1.22-1.08 (m, 3H), 1.02-0.96 (m, 36H). **^{13}C NMR** (100 MHz, $CDCl_3$) δ: 183.71, 165.32, 158.75, 151.99, 149.12, 127.89, 125.14, 110.26, 100.43, 67.13, 18.33, 18.27, 18.25, 10.68. Only one resonance peak for the methine carbons $SiCH(CH_3)_2$ was observed owing to overlapping. **ESI-MS** (*m*/*z*): $[M+Na]^+$ calcd for $C_{28}H_{46}Br_2O_4Si_2Na$, 685.1174; found, 685.1253.

1,2-Bis(3-bromo-5-(triisopropylsilyl)furan-2-yl)ethane-1,2-dione (OO)

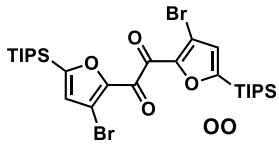

The diketone **OO** was synthesized according to a literature.[26] To a 50 mL flask were added **S4** (238 mg, 0.714 mmol), MnO_2 (621 mg, 7.14 mmol), and dry CH_2Cl_2 (7 mL). The mixture was stirred overnight at RT. The mixture was filtered through a pad of Celite, and then evaporated. The residue was purified by silica-gel column chromatography (hexane/AcOEt, 20:1) and GPC to give **OO** (70 mg, 15%) as a slight brown liquid, which was solidified upon standing to a white solid. **m.p.** 60.6 °C. **^{1}H NMR** (400 MHz, $CDCl_3$) δ: 6.84 (s, 2H), 1.27–1.24 (m, 6H), 1.04 (d, J = 7.6 Hz, 36H). **^{13}C NMR** (100 MHz, $CDCl_3$) δ: 179.95, 167.23, 149.54, 127.63, 110.90, 18.29, 10.77. **EA** Calcd for $C_{28}H_{44}BrO_4Si_2$: C, 50.91; H, 6.71. Found: C, 50.82; H, 6.67.

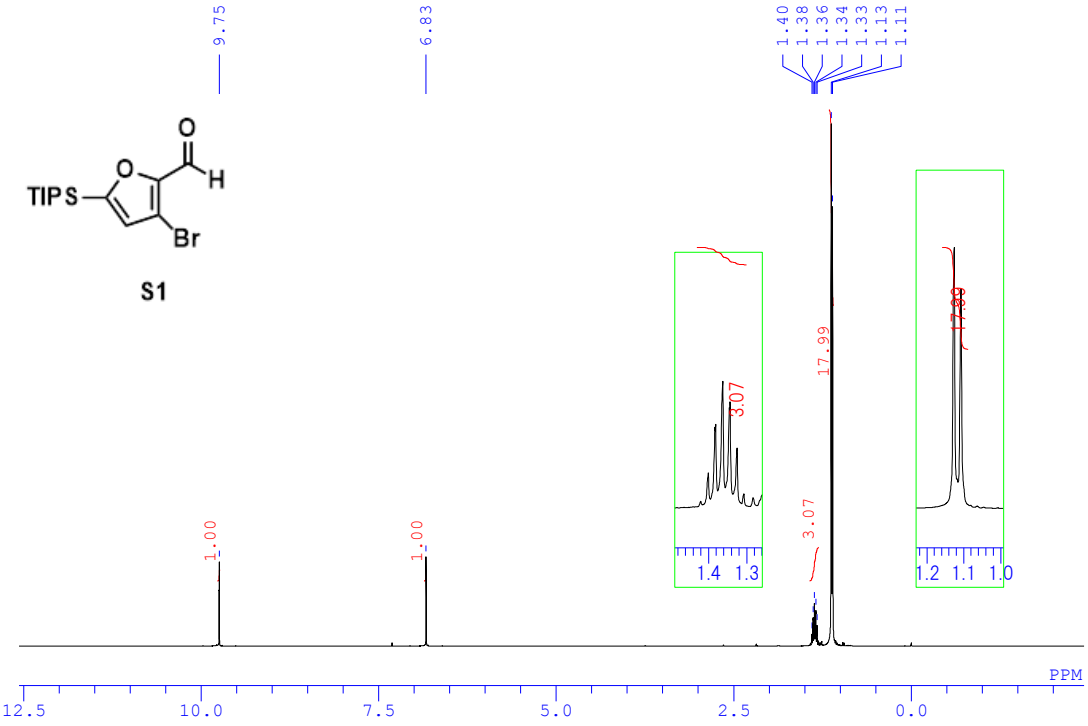
9.75
6.83
1.40
1.38
1.36
1.34
1.33
1.13
1.11
O
O
H
TIPS
Br
S1
1.00
1.00
3.07
17.99
3.07
1.4 1.3
1.2 1.1 1.0
PPM
12.5
10.0
7.5
5.0
2.5
0.0

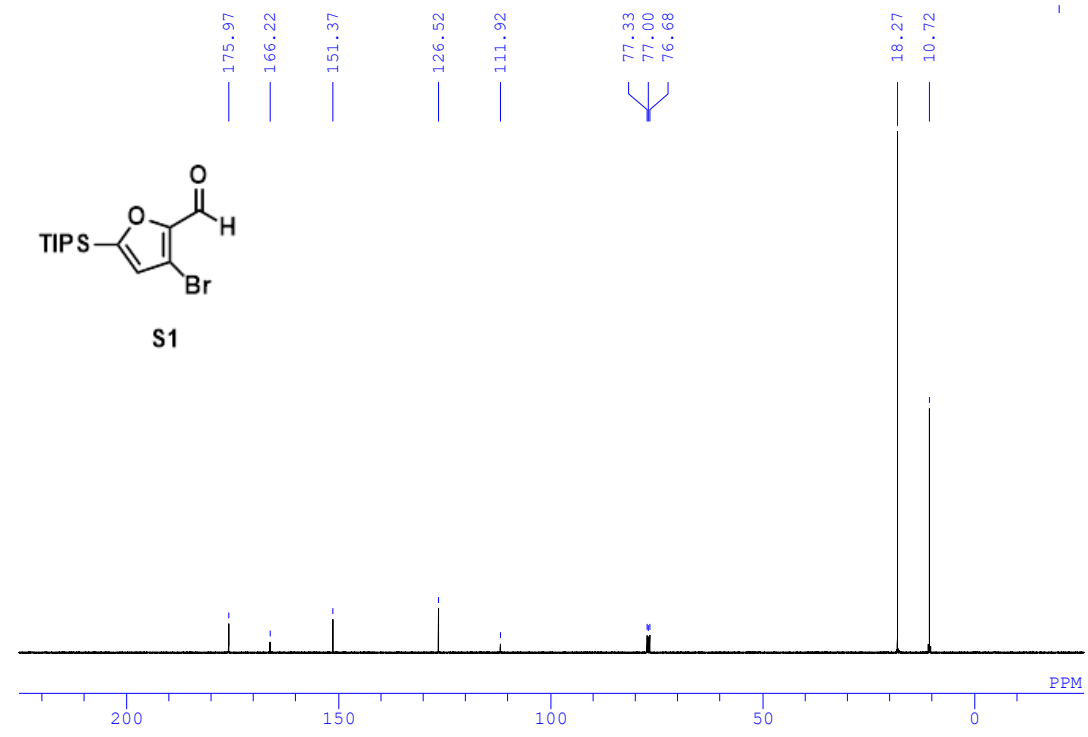
175.97
166.22
151.37
126.52
111.92
77.33
77.00
76.68
18.27
10.72
O
O
H
TIPS
Br
S1
PPM
200
150
100
50
0

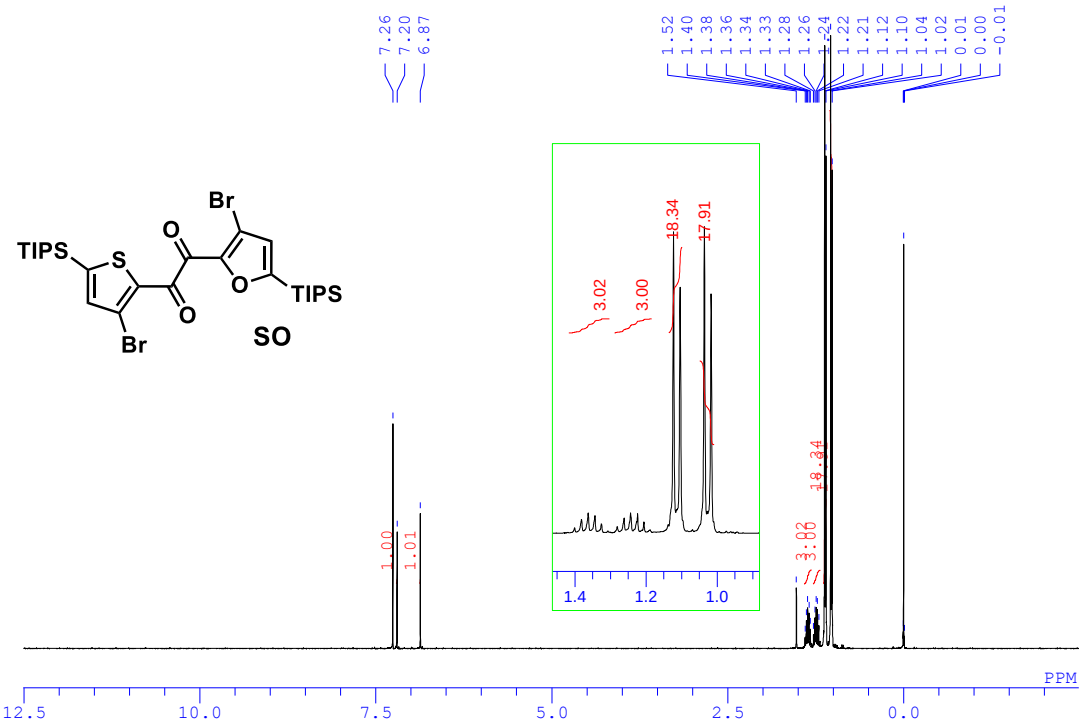
7.26
7.20
6.87
1.52
1.40
1.38
1.36
1.34
1.33
1.28
1.26
1.24
1.22
1.21
1.12
1.10
1.04
1.02
0.01
0.00
-0.01
Br
TIPS
S
O
O
O
TIPS
Br
SO
3.02
3.00
18.34
17.91
1.00
1.01
1.4
1.2
1.0
PPM
12.5
10.0
7.5
5.0
2.5
0.0

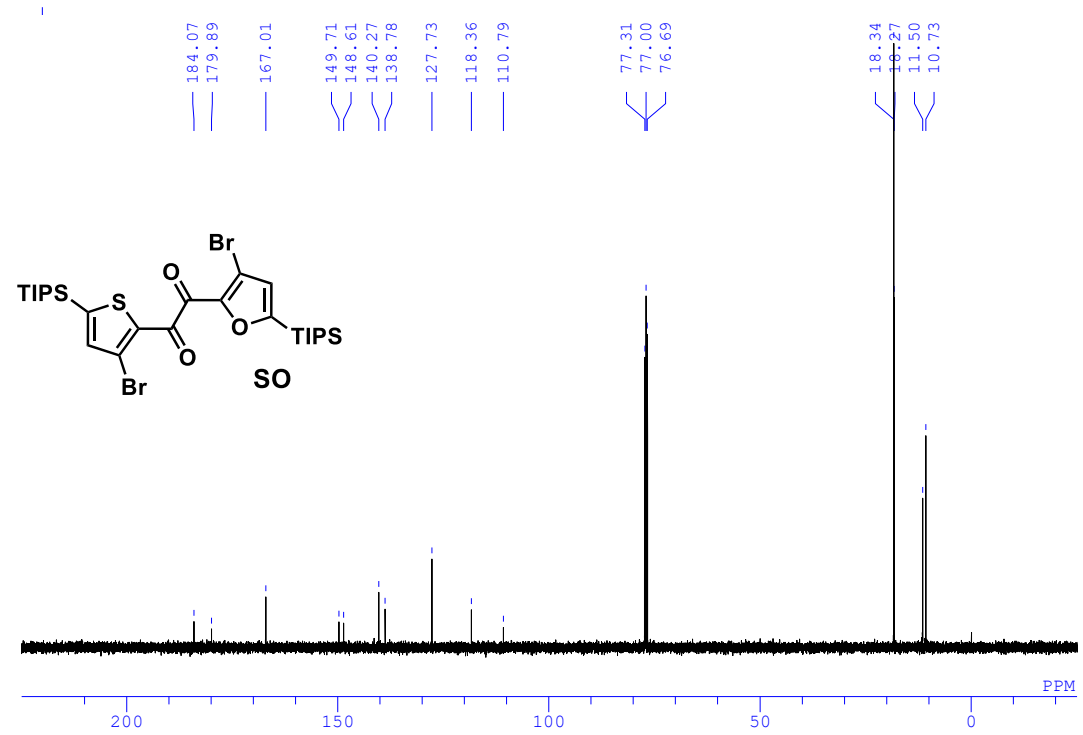
184.07
179.89
167.01
149.71
148.61
140.27
138.78
127.73
118.36
110.79
77.31
77.00
76.69
18.34
18.27
11.50
10.73
Br
TIPS
S
O
O
O
TIPS
Br
SO
PPM
200
150
100
50
0

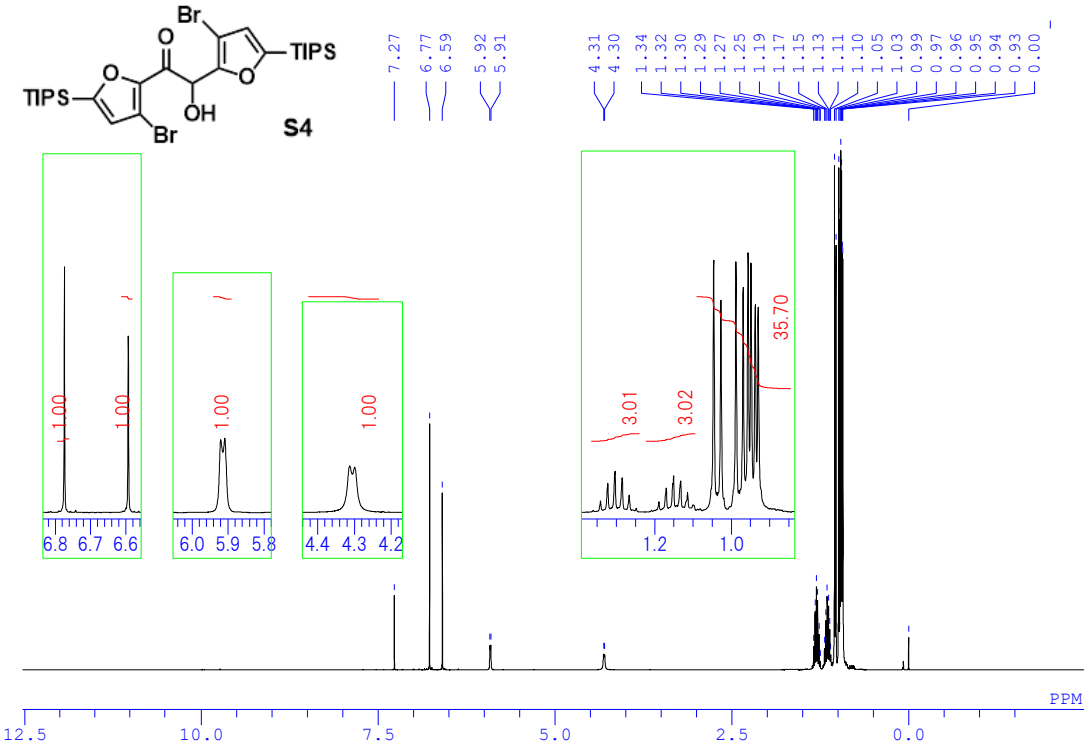
Br
O
TIPS
TIPS
O
O
OH
Br
S4
7.27
6.77
6.59
5.92
5.91
4.31
4.30
1.34
1.32
1.30
1.29
1.27
1.25
1.19
1.17
1.15
1.13
1.11
1.10
1.05
1.03
0.99
0.97
0.96
0.95
0.94
0.93
0.00
1.00
1.00
1.00
1.00
3.01
3.02
35.70
6.8 6.7 6.6
6.0 5.9 5.8
4.4 4.3 4.2
1.2
1.0
PPM
12.5
10.0
7.5
5.0
2.5
0.0

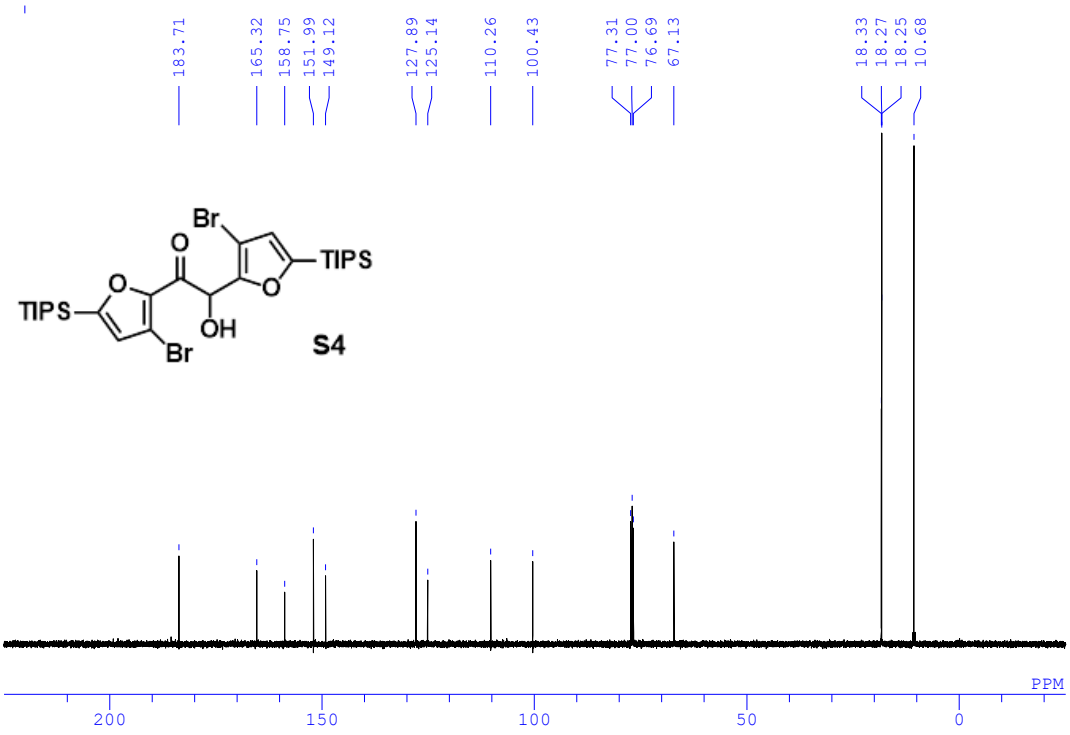
183.71
165.32
158.75
151.99
149.12
127.89
125.14
110.26
100.43
77.31
77.00
76.69
67.13
18.33
18.27
18.25
10.68
Br
O
TIPS
TIPS
O
O
OH
Br
S4
PPM
200
150
100
50
0

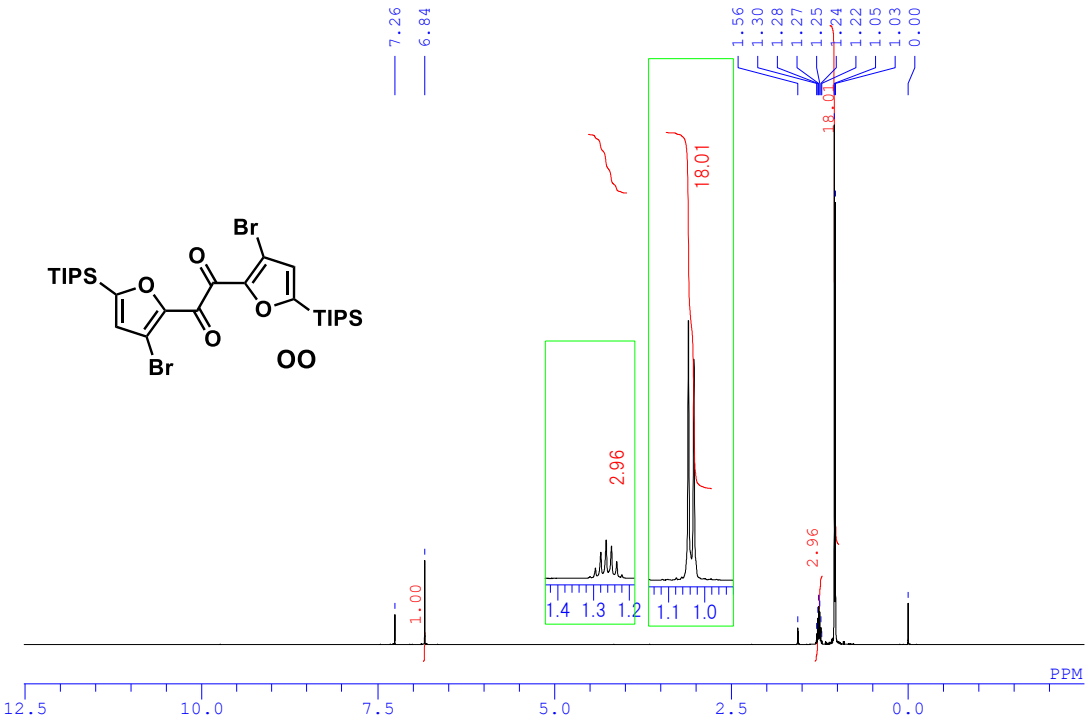
7.26
6.84
1.56
1.30
1.28
1.27
1.25
1.24
1.22
1.05
1.03
0.00
18.01
2.96
1.00
1.4 1.3 1.2
1.1 1.0
PPM
12.5
10.0
7.5
5.0
2.5
0.0
Br
TIPS
O
TIPS
Br
OO

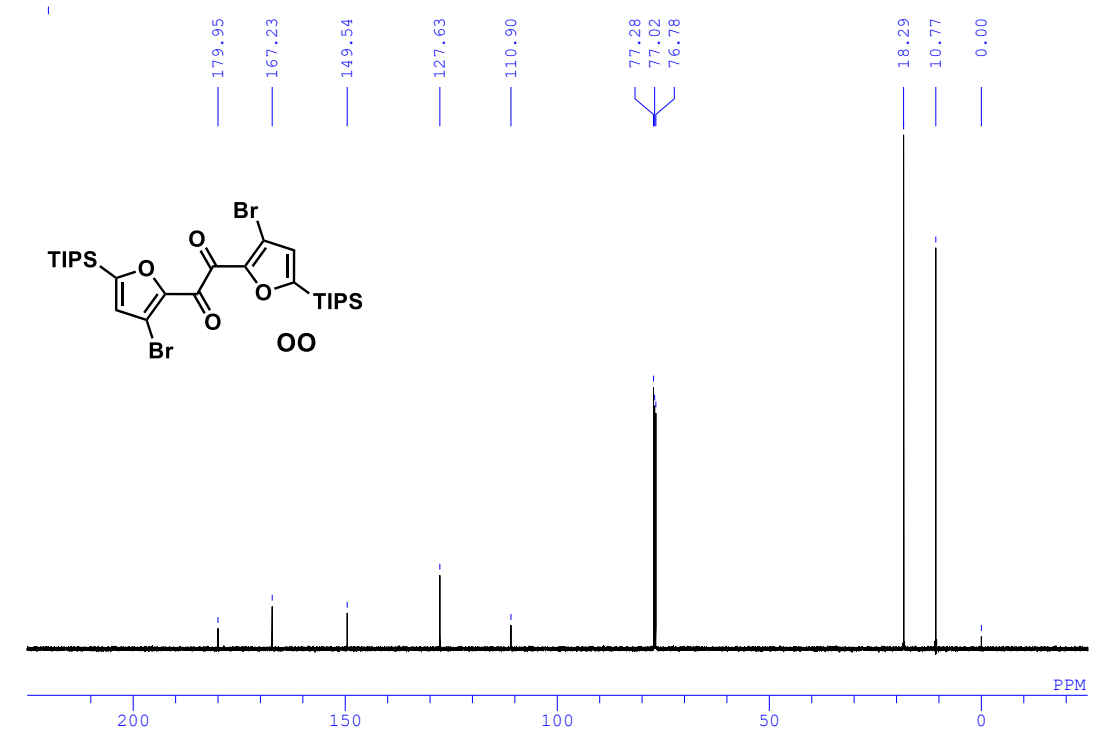
179.95
167.23
149.54
127.63
110.90
77.28
77.02
76.78
18.29
10.77
0.00
PPM
200
150
100
50
0
Br
TIPS
O
TIPS
Br
OO

2.4.3 Purity inspection of the measurement samples

The purity of **SO** was evaluated by recycling size-exclusion chromatography using a JAI LC-9130 NEXT instrument equipped with JAIGEL-1HR and 2HR (eluent: $CHCl_3$, flow rate: 10 mL/min) with a UV detector (254 nm). No trace of any impurity was detected (Figure 2.23). In addition, before and after recrystallization from MeOH (measured as SCL after melting the crystal), the photoluminescence spectra were identical (Figure 2.24) and the lifetimes were almost identical (16 vs 15 μs, Figure 2.25). The spectra of liquid **SO** from different synthesis batches were also identical (Figure 2.24).

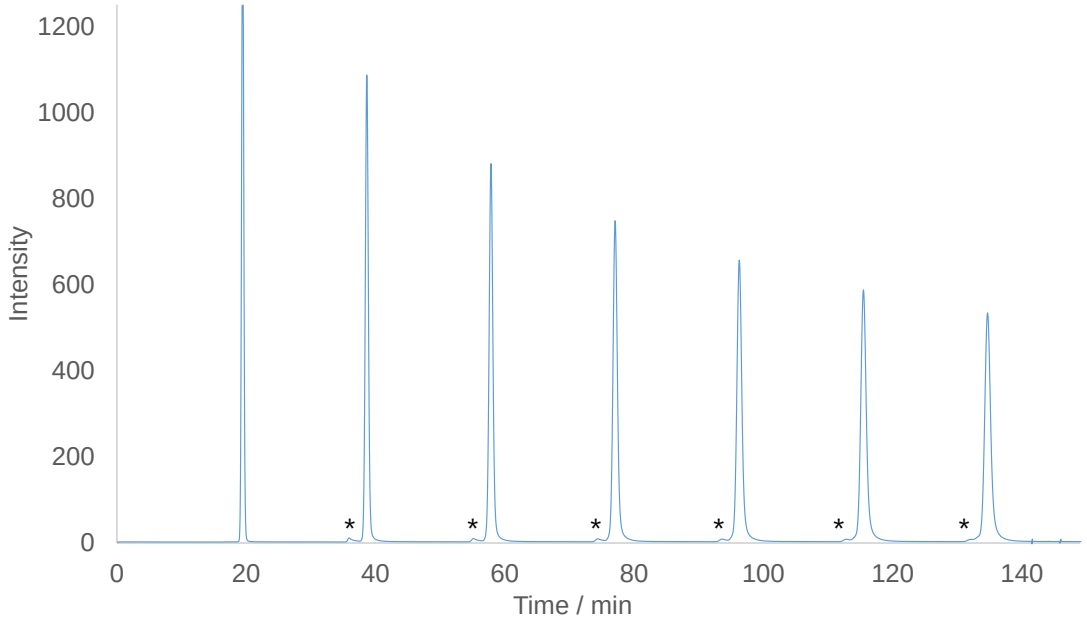

Figure 2.23. Recycling size-exclusion chromatogram of **SO**. Asterisks indicate recycling artifacts. Reproduced from ref I.

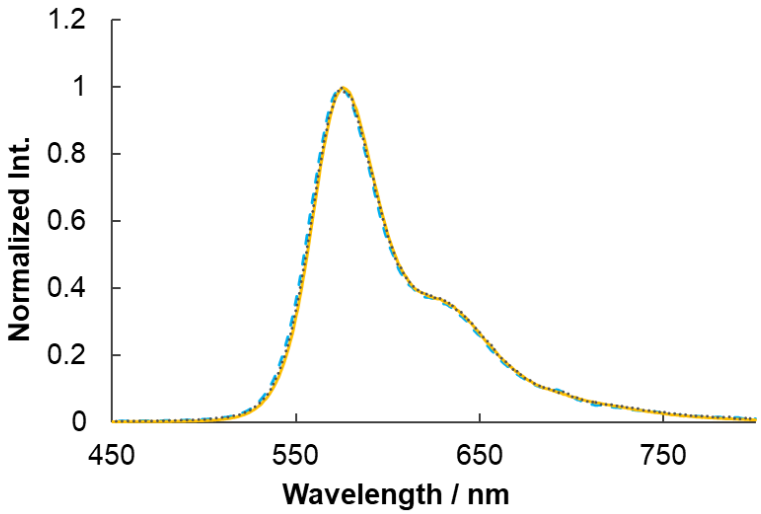

Figure 2.24. Photoluminescence spectra of liquid **SO** before (blue broken line) and after recrystallization from MeOH (yellow solid line), and from a different synthesis batch (grey dotted trace) at RT in air. Reproduced from ref I.

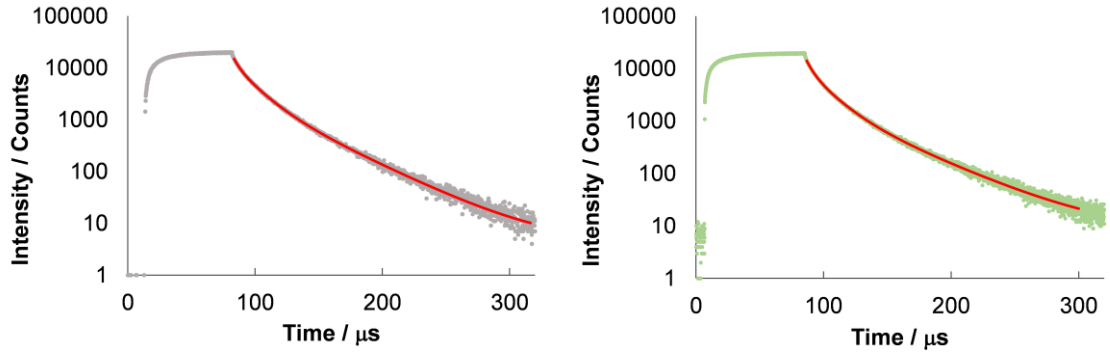

Figure 2.25. Photoluminescence decay curves of liquid **SO** before (left) and after recrystallization from MeOH (right) at RT in air. The red lines are fitted curves. PL intensities were recorded at 570 nm (λ_{ex} = 368 nm). Reproduced from ref I.

2.4.4 Optical inspection of liquid SO

Solvent-free liquid **SO** was inspected under an Olympus BX60M polarized and fluorescence microscope. Photographic images in Figure 2.2 were taken using SONY NEX-5N.

2.4.5 Photophysical properties in solution

2.4.5.1 PL, excitation, and UV-vis absorption spectra of SO in cyclohexane

Analytically pure **SO** was dissolved in spectral-grade cyclohexane (2.2×10^{-4} M), and degassed by Ar bubbling for 10 min. The PL spectrum was obtained (λ_{ex} = 368 nm) using a JASCO FP-8200 spectrometer. The excitation (λ_{em} = 570 nm) and UV-vis absorption spectra were obtained for a diluted solution (2.2×10^{-5} M) using the JASCO FP-8200 spectrometer and a Shimadzu UV-3150 spectrometer, respectively.

2.4.5.2 Comparison of the absorption spectra of SO in cyclohexane and liquid

UV-vis absorption spectrum of **SO** in solvent-free liquid state was obtained using a Shimadzu UV-3150 spectrometer with a Shimadzu ISR-3100 integrating sphere attachment. Liquid sample was prepared as a thin film by drop-casting onto a quartz substrate.

2.4.5.3 PL lifetime of SO in solution

The PL decay curve of **SO** in the degassed cyclohexane solution was acquired immediately after the measurement of the PL spectrum in Figure 2.26 with a HORIBA DeltaFlex multichannel scaling system using DeltaDiode for excitation (368 nm). The area-weighted average lifetime τ_p = 33 μs was obtained from a double-exponential fit using a HORIBA EZTime software (τ_1 = 11 μs (39%), τ_2 = 47 μs (61%)). The reduced chi-square of the curve fitting was 1.04. PL intensity of **SO** was recorded at 570 nm.

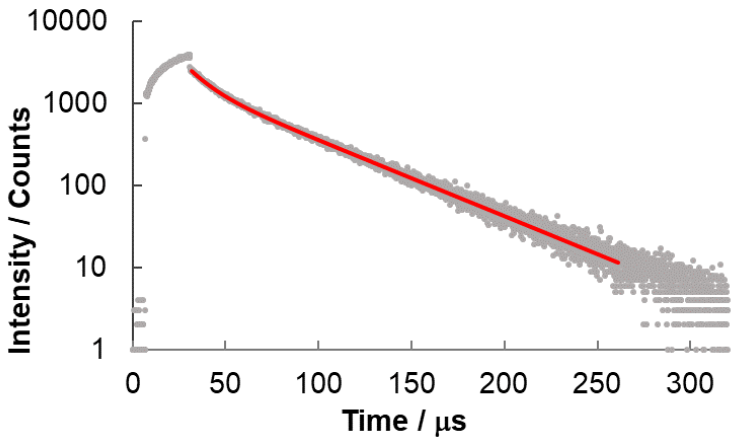

Figure 2.26. PL decay curve of **SO** in cyclohexane (2.2×10^{-4} M) at RT under Ar. The red line denotes the fit to the curve. The PL intensity at 570 nm was recorded (λ_{ex} = 368 nm). Reproduced from ref I.

2.4.5.4 External heavy atom effect in solution

The PL decay curve of **SO** in the degassed mixed cyclohexane and ethyl iodide solvents (5:1 and 11:1) was acquired with a HORIBA DeltaFlex multichannel scaling system using DeltaDiode for excitation (368 nm).

2.4.6 Photophysical and structural properties of solid SO

2.4.6.1 PLQY of solid SO

I was unable to determine the PLQY of solid **SO** because no emission was detected at all using the integrating sphere equipped on the C11347-01 spectrometer (Figure 2.14).

2.4.6.2 Single crystal X-ray structure analysis

Data were collected on a Rigaku XtaLAB Synergy-R diffractometer with graphite monochromated MoKα radiation (λ = 0.71075 Å) in the ω-scan mode. The crystal was cooled by a stream of cold N_2 gas. Collection, indexing, peak integration, cell refinement, and scaling of the diffraction data were performed using the CrysAlisPro (Rigaku) software. The structure was solved by direct method (SHELXT 2018) and refined by full-matrix least-square refinement on F^2 (SHELXL2018). The non-hydrogen atoms were refined anisotropically. All hydrogen atoms were placed on the calculated positions and refined using the riding model.

Table 2.3. Crystallographic data for **SO** (CCDC 2095928)

Empirical formula	$C_{28}H_{44}Br_2O_3SSi_2$
Formula weight	676.69
Temperature / K	123
Crystal system	Monoclinic
Space group	$P\,2_1/n$
a / Å	14.1498(4)
b / Å	9.2174(3)
c / Å	25.7482(8)
α / °	90
β / °	95.165(3)
γ / °	90
Volume / Å^3	3344.56(18)
Z	4
ρ(calcd) / g·cm^{-3}	1.344
Crystal size / mm^3	0.4 × 0.2 × 0.1
Completeness	99.99%
Goodness-of-fit on F^2	1.02
Final R indexes [I > =2σ (I)]	R_1 = 0.0569, wR_2 = 0.1030
Final R indexes [all data]	R_1 =0.0958, wR_2 = 0.1135
CCDC number	2095928

2.4.6.3 Hirshfeld surface analysis of SS and SO crystals

Hirshfeld surface analysis provides a way to view molecules as "organic wholes".[17a] To investigate the intermolecular interactions visually and quantitatively, Hirshfeld surfaces of **SS** and **SO** in the crystal structure were mapped with normalised contact distance d_{norm} with a fixed color scale of –0.3 (red) to 1.7 (blue) using CrystalExplorer21 software. [17b] d_{norm} is defined as follows:

$$d_{\mathrm{norm}} = \frac{d_{\mathrm{i}} - r_{\mathrm{vdW}}}{r_{\mathrm{vdW}}} + \frac{d_{\mathrm{e}} - r_{\mathrm{vdW}}}{r_{\mathrm{vdW}}}$$

where d_i is the distance from the Hirshfeld surface to the nearest nucleus inside the surface, d_e is the corresponding distance to the nearest nucleus outside the surface, and r_{vdW} is the van der Waals radius of the atoms. The positive (blue) d_{norm} indicates a distance larger than van der Waals contact. As a whole, the surface of **SO** is bluer than that of **SS**, and the mean of d_{norm} is larger for **SO** than

SS. In addition, the surface area is larger for **SS** than **SO** (609 and 570 Å^2). These results suggest weaker intermolecular interactions in **SO** than **SS**.

2.4.6.4 Structural identity of the single crystal and solid

PXRD patterns of solid **SO** were collected and compared with those simulated from the crystal structure. Considering that the crystal structure was determined at 123 K while the PXRD of the solid was conducted at RT, these two profiles matched very well, which indicates that the molecular arrangement and conformation in the solid sample were similar to those in the crystal (Figure 2.15).

2.4.7 Variable-Temperature PL measurement of the liquid SO

Liquid **SO** was placed in a quartz tube and capped with a silicon septum under air. The PL spectra were acquired from –120 to 20 °C in 10 °C steps using a JASCO FP-8200 spectrometer equipped with a CoolSpeK USP-203-B cryostat (UNISOKU) with a L42 sharp cut filter (HOYA, longpass, > 420 nm) and a U340 bandpass filter (HOYA) (λ_{ex} = 368 nm). The intensity increased at a lower temperature without the emergence of new peaks, indicating that the emission is phosphorescence-dominated (Figure 2.21). The plot of the maximum emission wavelength (λ_{max}) against reciprocal temperature ($1/T$) was constructed from three independent measurements with a standard deviation as error bars (Figure 2.20).

2.4.7.1 Rheology experiment

Rheology experiments were carried out using an ARES G2 (TA Instruments Inc.) rheometer. Liquid **SO** was sandwiched between two parallel plates so that it completely filled a gap of 1.0 mm. The complex shear modulus $G^* = G' + iG''$, where G' is the storage modulus and G'' is the loss modulus, were measured at 25 °C in an angular frequency ω range from 1 to 100 rad·s^{-1} under oscillatory shear deformation (γ = 1%). The complex viscosity $|\eta^*| = (\eta'^2 + \eta''^2)^{1/2}$, where $\eta' = G''/\omega$ and $\eta'' = G'/\omega$, matched well with η' (Figure 2.3). Therefore, the zero-shear viscosity η_0 of liquid **SO** was determined to be 45 ± 2 Pa·s as an average of η' in the angular frequency range from 1 to 100 rad·s^{-1} (shear stress from 46 to 2615 Pa). After the experiments, the sample was heated up to ca. 50 °C (below T_m, 59.5 °C), and then the upper plate was retracted. However, the sample remained as liquid (Figure 2.3b). For comparison, Kim *et al.* reported that shear frequency of 0.03 s^{-1} induced crystallization of stable supercooled molecular liquid (reference 19 in the main text, J. Kim *et al.*, *ACS Cent. Sci.* 2015). Note that angular frequency of 1 and 100 rad·s^{-1} corresponds to frequency of 0.16 and 16 s^{-1}, respectively.

2.4.7.2 Density functional theory calculations

(Time dependent (TD)-)density functional theory (DFT) calculations were conducted at the (U)B3LYP-D3/6-311G(d) level of theory using Gaussian 16 program package.[27] According to the

results in Chapter 2, the four conformers of (*S*)-**SO′**—skew, skew′, skew″, and planar—were optimized both in the ground state and the T_1 state. Frequency calculation confirmed that all the optimized structures have no imaginary frequency. **SO′**-planar (C_s symmetry, Figure 2.6 in the main text) is the most stable conformer in the T_1 states. In addition, starting from the (*S*)-**SO′**-skew in the ground state, I scanned the coordinates around each one of the two thiophene–carbonyl bonds. The step of the scan was set to 20°. At each structure, single-point TD-DFT calculations were performed to obtain the S_1 and T_1 energy levels. From the results, I concluded that **SO′**-planar (Figure 2.6 in the main text) is accessible upon photoexcitation of **SO′**-skew, which is the same conformer as that found in the crystal structure.

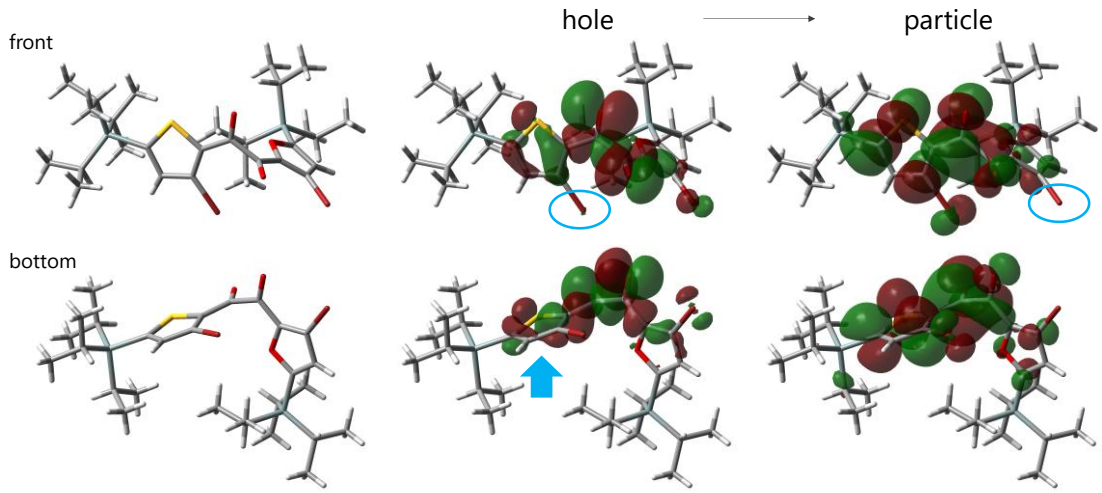

Figure 2.27. Molecular structure and natural transition orbitals for the phosphorescence (T_1–S_0) transition at the geometry of the crystal structure, calculated at the TD-uB3LYP-D3/6-311G(d) level of theory. Blue ellipses highlight the absence of orbital on bromine atoms, indicative of an inefficient heavy atom effect. The blue arrow highlights a π-symmetrical orbital contribution on the thiophene ring, which contaminates into the $^3(n,\pi^*)$ transition and decreases the transition probability. Reproduced from ref I.

2.4.7.3 Thermal property and thermochromic behavior of SO

Differential scanning calorimetry (DSC)

DSC was performed with a Hitachi NEXTA DSC200 (Figure 2.20c and Figure 2.28, the same measurement) or a Rigaku Thermo Plus EVO II (Figure 2.4) under a flow of nitrogen. There is no exothermic recrystallization peak in the heating and cooling traces even at slower scanning rates (up to 0.3 °C·min^{-1}).[13]

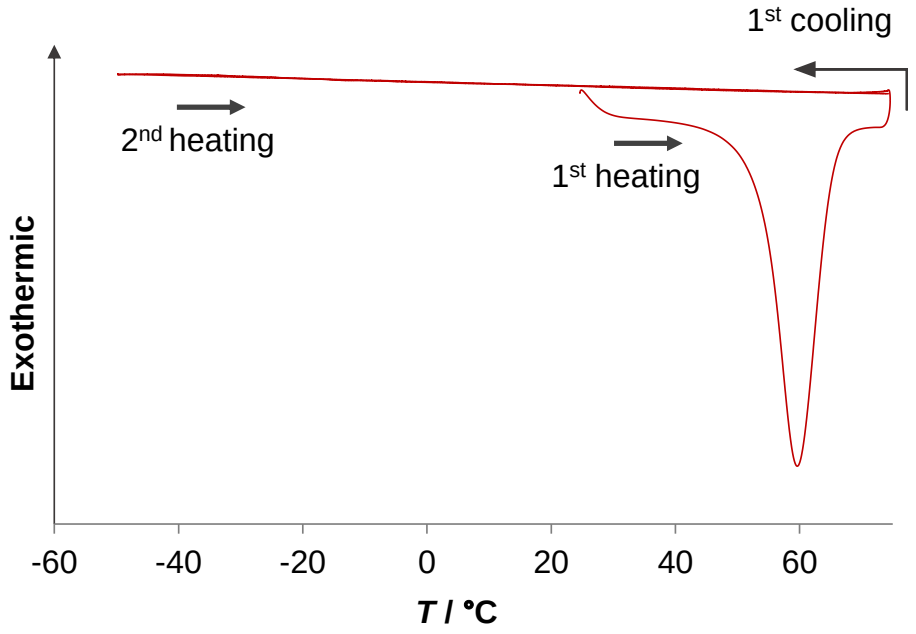

Figure 2.28. DSC thermograms of solid **SO** during heating/cooling cycles at 10 °C·min^{-1} for the 1st heating and at 0.3 °C·min^{-1} for the 1st cooling and 2nd heating processes, under a flow of N_2. Reproduced from ref I.

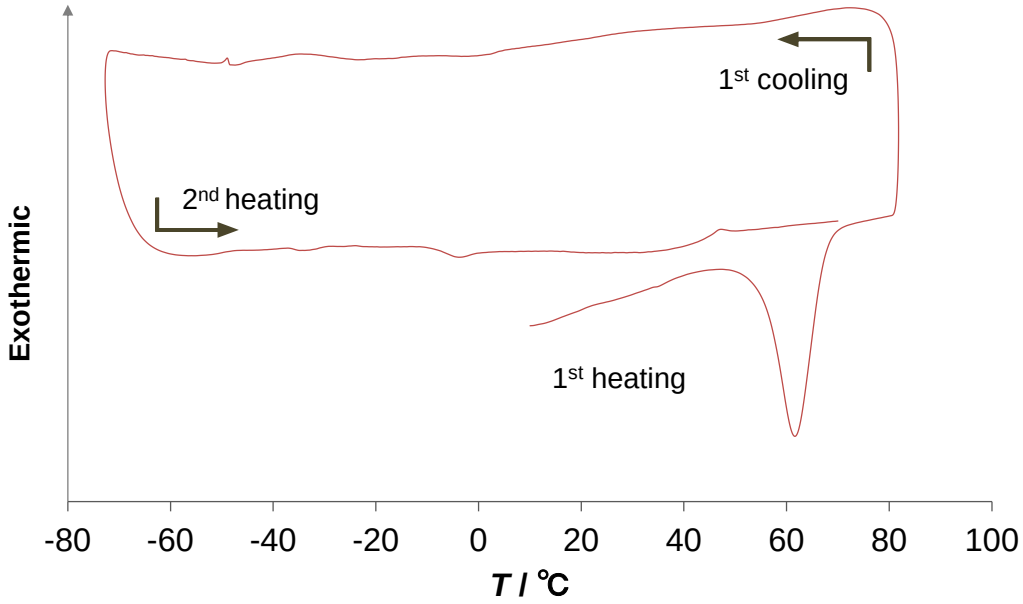

Figure 2.29. DSC thermograms of solid **SO** during heating/cooling cycles at 10 °C·min^{-1} under a flow of N_2. Reproduced from ref I.

2.5 References and Notes

1 a) T. Nakanishi, Functional Organic Liquids, *John Wiley & Sons, Ltd*, 2019; b) F. Lu and T. Nakanishi, *Adv. Opt. Mater*. 2019, **7**, 1900176; c) A. Ghosh and T. Nakanishi, *Chem. Commun.* 2017, **53**, 10344–10357; d) K. Kushwaha, L. Yu, K. Stranius, S. K. Singh, S. Hultmark, M. N. Iqbal, L. Eriksson, E. Johnston, P. Erhart, C. Müller and K. Börjesson, *Adv. Sci.* 2019, **6**, 1801650.

2 Goudappagouda, A. Manthanath, V. C. Wakchaure, K. C. Ranjeesh, T. Das, K. Vanka, T. Nakanishi and S. S. Babu, *Angew. Chem., Int. Ed.* 2019, **58**, 2284–2288.

3 For selected examples of single-component molecular solids that exhibit multiple phosphorescence, see: a) J. Chen, X. Chen, Y. Liu, Y. Li, J. Zhao, Z. Yang, Y. Zhang and Z. Chi, *Chem. Sci.* 2021, **12**, 9201.; b) K. Tabata, T. Yamada, H. Kita and Y. Yamamoto, *Adv. Funct. Mater.* 2019, **29**, 1805824.

4 For single-component molecular solids that exhibit thermochromic phosphorescence, see: a) Z. Niu, C. Ma, W. Ye, H. Wang, W. Jia, H. Shi, H. Shi, Z. An and W. Huang, *RSC Adv.* 2019, **9**, 19075–19078.; b) T. Wang, Z. Hu, X. Nie, L. Huang, M. Hui, X. Sun and G. Zhang, *Nat. Commun.* 2021, **12**, 1364.

5 a) Y. Tani, M. Terasaki, M. Komura and T. Ogawa, *J. Mater. Chem. C* 2019, **7**, 11926–11931; b) Y. Tani, M. Komura and T. Ogawa, *Chem. Commun.* 2020, **56**, 6810–6813.

6 R. J. C. Brown and R. F. C. Brown, *J. Chem. Educ.* 2000, **77**, 724; b) A. Gavezzotti, J. Chem. Soc., *Perkin Trans. 2* 1995, 1399–1404.

7 a) D. Mari, N. Miyagawa, K. Okano and A. Mori, *J. Org. Chem.* 2018, **83**, 14126–14137; b) J. Fröhlich and C. Hametner, *Monatsh Chem* 1996, **127**, 435–443.

8 a) D. S. Roy, K. Bhattacharyya, S. C. Bera and M. Chowdhury, *Chem. Phys. Lett.* 1980, **69**, 134–140. (b) K. Bhattacharyya and M. Chowdhury, *J. Photochem.* 1986, **33**, 61–65.

9 a) N. J. Turro, Modern Molecular Photochemistry, University Science Books, *Sausalito, CA,* 1991; b) S. K. Lower and M. A. El-Sayed, *Chem. Rev.* 1966, **66**, 199–241; c) S. Hirata, *Adv. Opt. Mater.* 2017, **5**, 1700116.

10 Bolton, K. Lee, H.-J. Kim, K. Y. Lin and J. Kim, *Nat. Chem.* 2011, **3**, 205–210.

11 In principle, Φ_p can be expressed as follows: $\Phi_p = \Phi_{ISC}\, k_p / (k_p + k_{nr}) = \Phi_{ISC}\, k_p\, \tau_p$, where Φ_{ISC} is the quantum efficiency of intersystem crossing (ISC). I assumed Φ_{ISC} to be unity because no discernible fluorescence was observed. However, the experimentally determined Φ_p / τ_p gives $\Phi_{ISC}\, k_p$. The larger Φ_p / τ_p for the liquid likely indicates a larger k_p, but might also indicate a larger Φ_{ISC}, which is explained by external heavy atom effects that facilitate the ISC in the liquid.

12 a) K. Suzuki, A. Kobayashi, S. Kaneko, K. Takehira, T. Yoshihara, H. Ishida, Y. Shiina, S. Oishi and S. Tobita, *Phys. Chem. Chem. Phys.* 2009, **11**, 9850–9860. (b) A. M. Brouwer,

Pure Appl. Chem. 2011, **83**, 2213–2228.

13 a) F. Lu, K. Jang, I. Osica, K. Hagiwara, M. Yoshizawa, M. Ishii, Y. Chino, K. Ohta, K. Ludwichowska, K. J. Kurzydłowski, S. Ishihara and T. Nakanishi, *Chem. Sci.* 2018, **9**, 6774–6778; b) T. Machida, R. Taniguchi, T. Oura, K. Sada and K. Kokado, *Chem. Commun.* 2017, **53**, 2378.

14 a) Kenry, C. Chen and B. Liu, *Nat. Commun.* 2019, **10**, 2111; b) A. D. Nidhankar, Goudappagouda, V. C. Wakchaure and S. S. Babu, *Chem. Sci.* 2021, **12**, 4216–4236.

15 a) D. B. Clapp, *J. Am. Chem. Soc.* 1939, **61**, 523–524; b) C. S. Bilen, N. Harrison and D. J. Morantz, *Nature* 1978, **271**, 235–237; c) W. Z. Yuan, X. Y. Shen, H. Zhao, J. W. Y. Lam, L. Tang, P. Lu, C. Wang, Y. Liu, Z. Wang, Q. Zheng, J. Z. Sun, Y. Ma and B. Z. Tang, *J. Phys. Chem. C* 2010, **114**, 6090–6099; d) Z. An, C. Zheng, Y. Tao, R. Chen, H. Shi, T. Chen, Z. Wang, H. Li, R. Deng, X. Liu and W. Huang, *Nat. Mater.* 2015, **14**, 685–690; e) M. Baroncini, G. Bergamini, P. Ceroni and *Chem. Commun.* 2017, **53**, 2081–2093; f) A. Forni, E. Lucenti, C. Botta and E. Cariati, *J. Mater. Chem. C* 2018, **6**, 4603-4626.

16 a) W. Zhao, Z. He and B. Z. Tang, Nat. Rev. Mater. 2020, **5**, 869–885; b) X. Ma, J. Wang and H. Tian, *Acc. Chem. Res.* 2019, **52**, 738–748; c) N. Gan, H. Shi, Z. An and W. Huang, *Adv. Funct. Mater.* 2018, **28**, 1802657.

17 a) P. R. Spackman, M. J. Turner, J. J. McKinnon, S. K. Wolff, D. J. Grimwood, D. Jayatilaka and M. A. Spackman, *J. Appl. Cryst.* 2021, **54**, 1006–1011; b) M. A. Spackman and D. Jayatilaka, *CrystEngComm* 2009, **11**, 19–32; c) M. A. Spackman and P. G. Byrom, *Chem. Phys. Lett.* 1997, **267**, 215–220.

18 a) S. Suzuki, D. Yamaguchi, Y. Uchida and T. Naota, *Angew. Chem., Int. Ed.* 2021, **60**, 8284–8288.; b) H. Shoji and S. Kobatake, *Chem. Commun*. 2013, **49**, 2362–2364.

19 K. Chung, M. S. Kwon, B. M. Leung, A. G. Wong-Foy, M. S. Kim, J. Kim, S. Takayama, J. Gierschner, A. J. Matzger and J. Kim, *ACS Cent. Sci.* 2015, **1**, 94–102.

20 a) T. Ogawa, W. M. C. Sameera, M. Yoshida, A. Kobayashi and M. Kato, *Dalton Trans.* 2018, **47**, 5589–5594; b) T. Ogawa, M. Yoshida, H. Ohara, A. Kobayashi and M. Kato, *Chem. Commun.* 2015, **51**, 13377–13380.

21 M. Han, Y. Tian, Z. Yuan, L. Zhu and B. Ma, *Angew. Chem., Int. Ed.* 2014, **53**, 10908–10912.

22 A. B. Pangborn, M. A. Giardello, R. H. Grubbs, R. K. Rosen and F. J. Timmers, *Organometallics* 1996, **15**, 1518–1520.

23 a) D. Mari, N. Miyagawa, K. Okano and A. Mori, *J. Org. Chem.* 2018, **83**, 14126–14137; b) J. Fröhlich, C. Hametner, *Monatsh Chem* 1996, **127**, 435–443.

24 B. Tang, C. D. Bray, G. Pattenden and J. Rogers, *Tetrahedron* 2010, **66**, 2492–2500.

25 E. G. Delany and S. J. Connon, *Org. Biomol. Chem.* 2018, **16**, 780–786.

26 A. Feriani, G. Gaviraghi, G. Toson, M. Mor, A. Barbieri, E. Grana, C. Boselli, M. Guarneri,

D. Simoni and S. Manfredini, *J. Med. Chem.* 1994, **37**, 4278–4287.

27 M. J. Frisch, G. W. Trucks, H. B. Schlegel, G. E. Scuseria, M. A. Robb, J. R. Cheeseman, G. Scalmani, V. Barone, G. A. Petersson, H. Nakatsuji, X. Li, M. Caricato, A. V. Marenich, J. Bloino, B. G. Janesko, R. Gomperts, B. Mennucci, H. P. Hratchian, J. V. Ortiz, A. F. Izmaylov, J. L. Sonnenberg, Williams, F. Ding,F. Lipparini, F. Egidi, J. Goings, B. Peng, A. Petrone, T. Henderson, D. Ranasinghe, V. G. Zakrzewski, J. Gao, N. Rega, G. Zheng, W. Liang, M. Hada, M. Ehara, K. Toyota, R. Fukuda, J. Hasegawa, M. Ishida, T. Nakajima, Y. Honda, O. Kitao, H. Nakai,T. Vreven, K. Throssell, J.A. Montgomery Jr., J. E. Peralta, F. Ogliaro, M. J. Bearpark, J. J. Heyd, E.N. Brothers, K.N. Kudin, V. N. Staroverov, T. A. Keith, R. Kobayashi, J. Normand, K. Raghavachari, A. P. Rendell, J. C. Burant, S. S. Iyengar, J. Tomasi, M. Cossi, J. M. Millam, M. Klene, C. Adamo, R. Cammi, J. W. Ochterski, R. L. Martin, K. Morokuma, O. Farkas, J. B. Foresman and D.J. Fox, *Gaussian 16 Rev. B.01*; Wallingford, CT, 2016.

Chapter 3

Photoinduced Crystal Melting with Luminescence Evolution Based on Conformational Isomerization

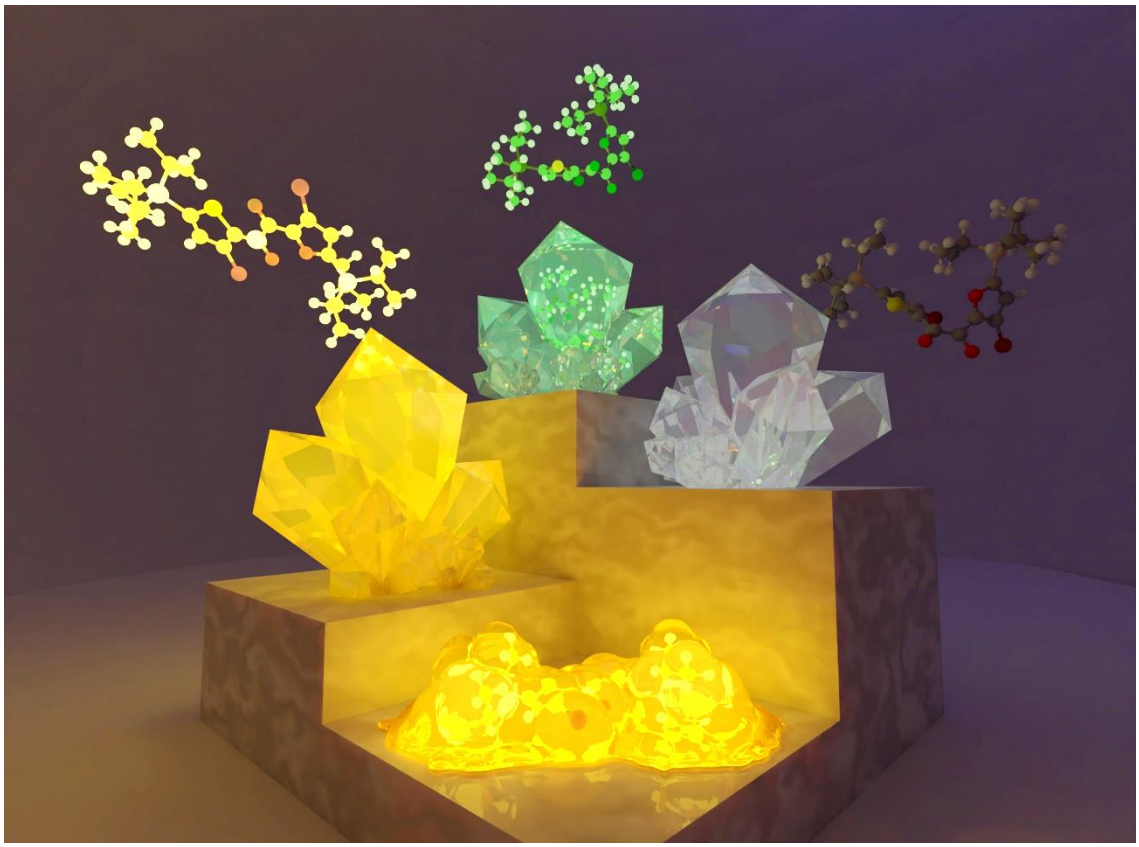

Selected as the inside front cover[II]

3.1 Introduction

Photo-induced crystal-to-liquid transition (PCLT) is the phenomenon of crystal melting by light irradiation,[1–16] in which photoexcitation causes molecular structural changes in the crystal and eventually leads to the melting. PCLT has been actively investigated due to a fundamental interest in the underlying mechanism/process of transducing light energy from the molecular structure change to macroscopic phase transition. Moreover, considerable effort has been focused on applications such as photolithography,[8] thermal energy storage,[9–12] and light-melt adhesion[13–15,17,18] because PCLT can induce drastic changes in the macroscopic physical properties. However, the PCLT-active molecular motifs are severely limited. Namely, PCLT has been observed in only three photochromic motifs: azobenzene,[1–11,13–15] hydrazone,[12] and spiropyran[16] that undergo *E*/*Z* isomerization or the cleavage/formation of the σ-bond in crystals upon excitation. As a consequence, whether being molecularly photochromic is mandatory or not is inconclusive; a minimum requirement for the molecules to be PCLT-active can be to exhibit excited-state structural changes. Given that various photofunctional molecules other than photochromic ones exhibit considerable structural changes at the excited states, the molecular design and functions of PCLT-active materials hold immense potential for increased diversity. In particular, photofunctions that are sensitive to the molecular conformation and/or environment are worth integrating with PCLT; such functions will be useful to reveal how the molecular structural change leads to the melting of the whole crystal.

Luminescence is a promising property for the *in situ* observations of phase transitions because it allows the real-time, high-sensitivity detection of the emissive part in a bulk material.[19-22] Microscopic visualization of the crystallization process based on time-course luminescence have been reported previously.[23-27] However, to the best of my knowledge, PCLT has never been studied using luminescence. Although azobenzenes are a promising motif for studying PCLT, their photoinduced *trans-cis* isomerization dissipates the excited-state energy nonradiative (Figure 3.1a).[28–30]

In chapter 2, I reported the room-temperature phosphorescence (RTP) of a heteroaromatic diketone, **SO** (Figure 3.1b).[31] In contrast to typical metal-free organic phosphors that only phosphoresce in the crystal form,[32-36] **SO** exhibits RTP in its supercooled liquid (SCL) state (*i.e.*, the metastable liquid state at temperatures lower than its melting point). Detailed experimental and theoretical investigations revealed that **SO** exists in distinct rotational isomers, including skew and planar conformers (Figure 3.1b). Most notably, while the crystal consists of the poorly emissive skew conformer, the planar conformer is more stable in the excited state and is responsible for the RTP in the SCL state.[31,37-40] Such conformation-dependent RTP would be promising to visualize PCMT.

Here, I report on heteroaromatic 1,2-diketones as a novel class of PCLT-active compounds,

which do not contain conventional photochromic frameworks. Moreover, one of the diketones, **SO**, exhibits PCLT accompanied by luminescence evolution (Figure 3.1b). During light irradiation, the **SO** crystal exhibits two-step changes in the luminescence color and intensity, which are reflective of the molecular conformation and environment and allow for the visualization of the local melting process in real-time.[41] Although the photo-induced RTP enhancement of organic crystals has been actively investigated, none of them leads to the melting transition.[42–47] My work demonstrates the functional diversification of PCLT-active motifs, which expands future directions toward the development of PCLT-related materials.

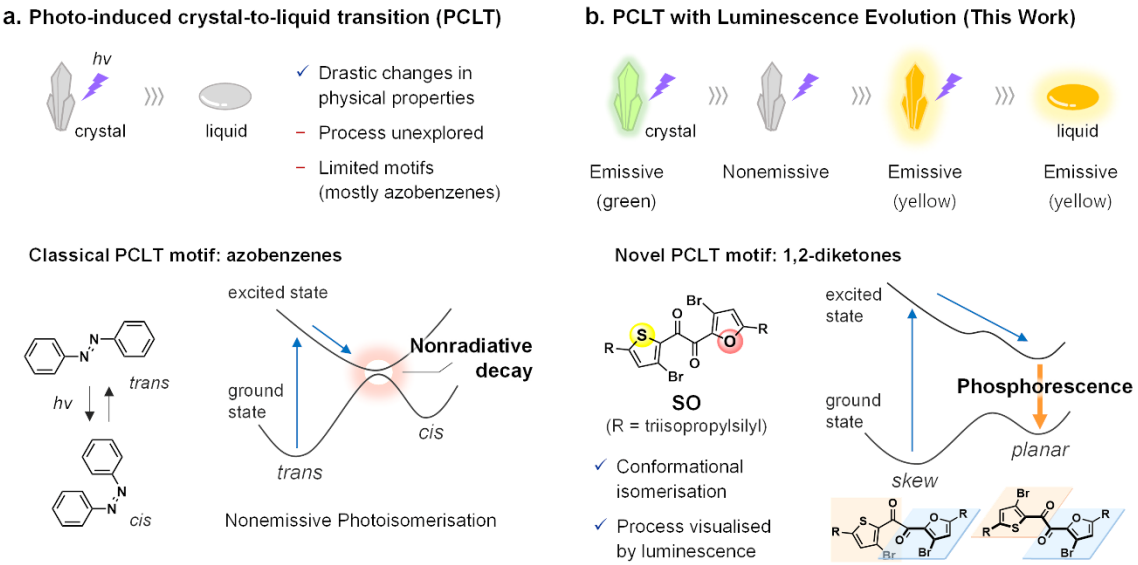

Figure 3.1. Schematic illustration of the photoinduced crystal-to-liquid transition (PCLT), chemical motifs, and their photophysical pathways. (a) Classical PCLT without luminescence properties. (b) PCLT with luminescence evolution. See Figure 3.14 and Figure 3.15 for calculated potential energy curves of **SO**. Reproduced from ref II.

3.2 Results and Discussion

3.2.1 Real-time tracking of PCLT with luminescence evolution

This research was initiated by an unexpected observation of the photoinduced melting of the **SO** crystal, accompanied by the changes in luminescence intensity and color under a fluorescence microscope (Figure 3.2a).[41] Under ultraviolet (UV) irradiation (60 mW cm^{-2}, λ_{max} = 365 nm), the crystal initially exhibits a feeble green emission, which disappeared within few seconds. Moreover, the yellow emission, which had 15 μs lifetime and was assigned as phosphorescence (Figure 3.3), emerged and expanded to the whole crystal. Finally, the crystal melted into an isotropic liquid, as evident from the disappearance of the birefringence (Figure 3.4). As reported

in Chapter 2, **SO** forms a kinetically super-stable SCL at room temperature that exhibits the same yellow RTP.[31] Hence, its melting is a crystal-to-SCL transition, that is, a transition to the kinetically trapped metastable phase. Irradiation with blue light (BL) resulted in no discernible changes in the bright-field and polarizing images even after more than 30 min (Figure 3.6b). In contrast, UV irradiation induced noticeable melting (i.e., the birefringence was faded and the outline of crystals became rounder) only after 2.5 min (Figure 3.6c). The UV-vis absorption spectrum of the **SO** crystal indicated that the crystal absorbs more photons in the UV region than in the BL region (Figure 3.5). Therefore, the melting of crystal is triggered by light absorption.

Next, to learn more about the photomelting phenomenon, UV light was irradiated on the top-left part of the crystal (Figure 3.2b, top right). After 220 s, only the irradiated area exhibited yellow emission and melted (Figure 3.2b, bottom row). The sharp boundary indicates that the melting transition does not propagate to the unirradiated crystal region and is not caused by heat. Note that the emergence of the yellow luminescence also supports the non-heat-induced melting, because the phosphorescence of the SCL state disappears at higher temperatures (lower than the melting point, which is 59.5 °C, see Figure 3.7). In addition, the sharp boundary also indicates that the recrystallisation of the melt is sufficiently slow, likely owing to the high kinetic stability of the SCL state. Most notably, the turning-on of the luminescence preceded the macroscopic melting. The bright-field and polarizing optical images indicated that the irradiated area was still crystalline after 60-s irradiation, while a distinct emission was observed simultaneously (Figure 3.2b, middle row). Thus, the emission is clearly indicative of molecular-level melting, which is not evident from the light reflection, transmission, and absorption characteristics.

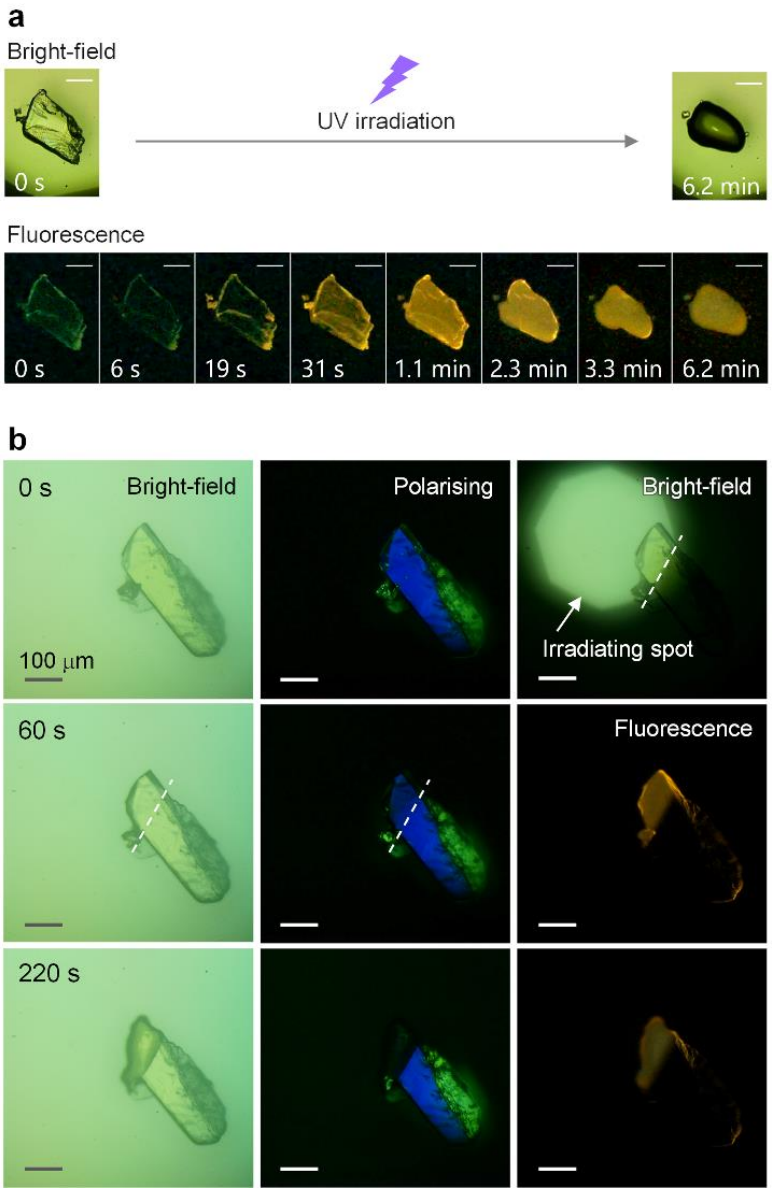

Figure 3.2. Photographic images of the photoinduced crystal melting with luminescence evolution observed under microscope. (a) Whole crystal was exposed to UV irradiation (scale bar: 50 μm). (b) Top-left part of the crystal was exposed to UV irradiation. Polarizing optical microscope images were taken under cross Nichol prism. Reproduced from ref II.

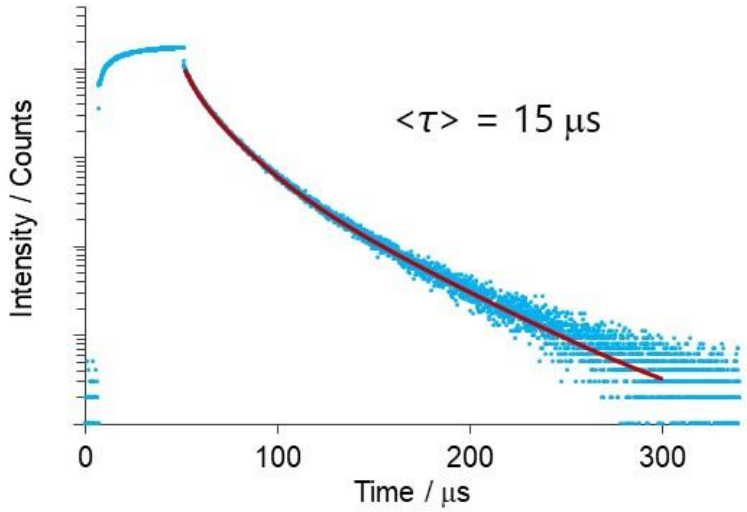

Figure 3.3. Photoluminescence decay curve of **SO** crystal after UV irradiation for 1 min at RT in air. The red line is the fitted curve. PL intensity was recorded at 575 nm (λ_{ex} = 368 nm). Reproduced from ref II.

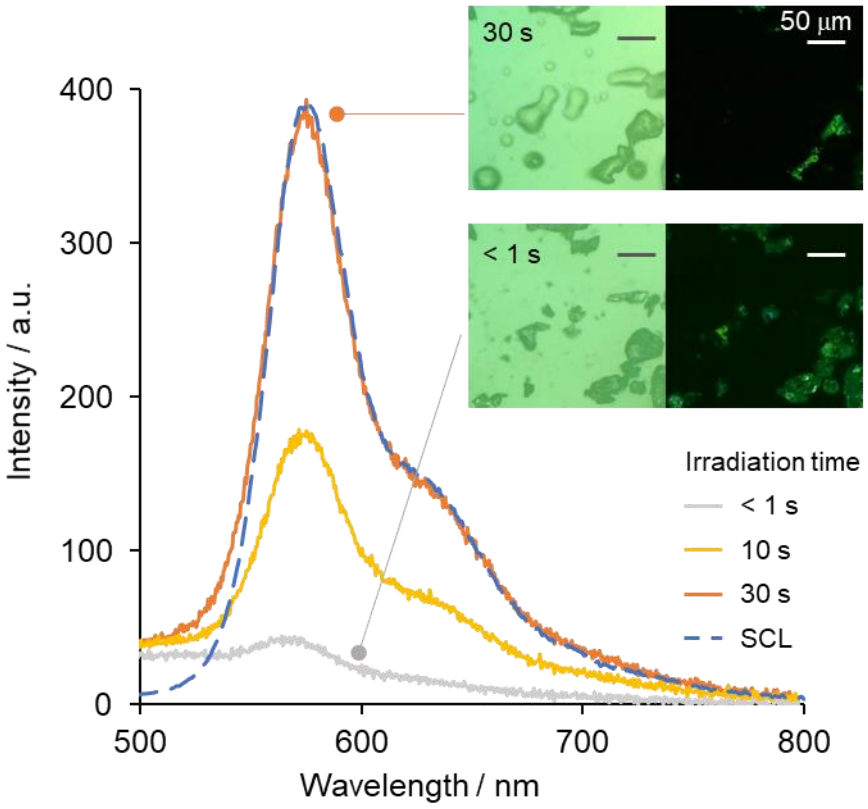

Figure 3.4. Photoluminescence spectra of **SO** pristine powder and SCL. Inset: photographic images under bright-field (left) and polarizing (right) optical microscope before and after irradiation. Reproduced from ref II.

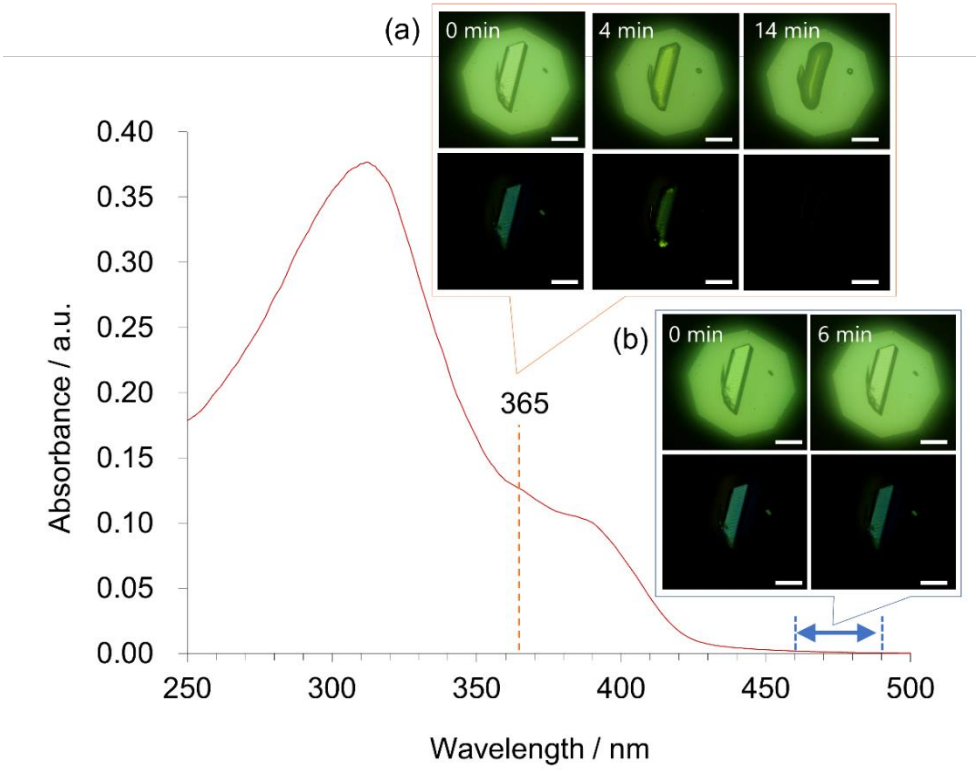

Figure 3.5. Absorption spectrum and photographic images of **SO** crystal obtained using (inset, top) bright-field and (inset, bottom) polarizing optical microscopes with crossed Nichol prisms before and after (a) UV-light irradiation and (b) blue-light irradiation for indicated periods. Double-headed arrow represents irradiation wavelength range of blue light. Scale bar: 100 μm. Reproduced from ref II.

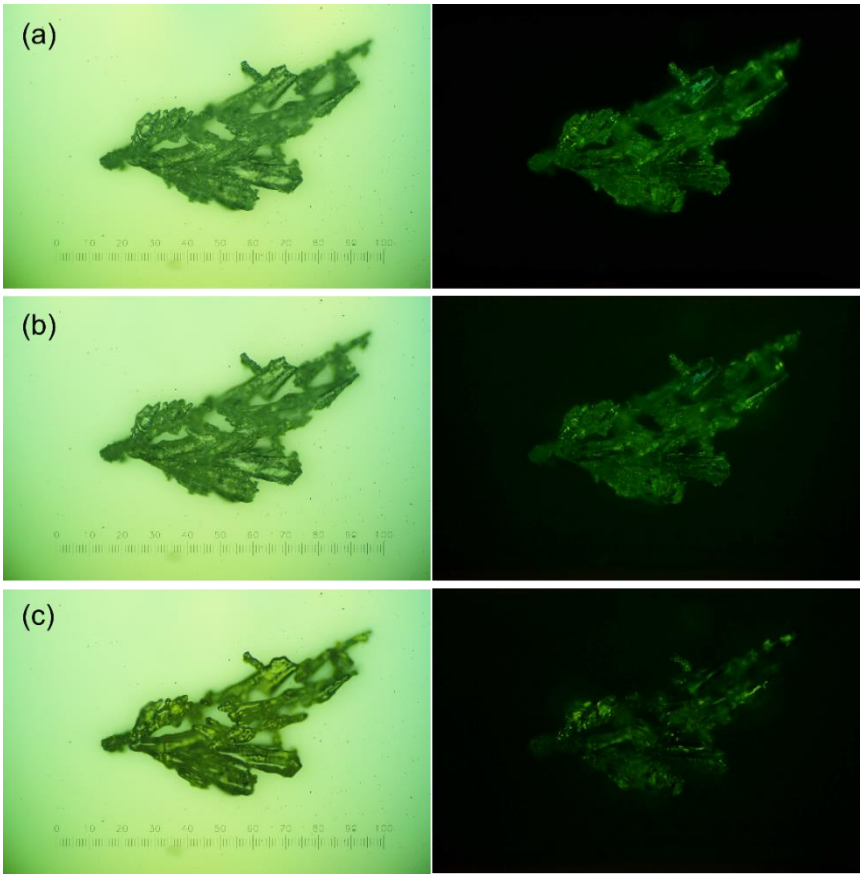

Figure 3.6. Photographic images of **SO** crystals under (left) bright-field and (right) polarizing optical microscope with crossed Nichol prisms (a) before irradiation, (b) after continuous blue-light irradiation for 32 min, and (c) after continuous UV-light irradiation for 2.5 min. Scale bar: 1.0 mm. Reproduced from ref II.

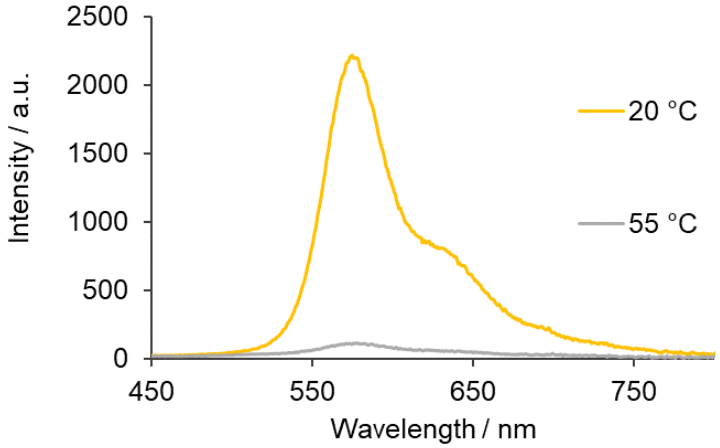

Figure 3.7. Steady-state PL spectra of **SO** SCL at 20 and 55 °C. Reproduced from ref II.

To gain further insights into the luminescence evolution during PCLT, I tracked the changes in the luminescence spectrum of a single crystal under continuous UV irradiation (Figure 3.8a). UV excitation initially resulted in a weak green luminescence peak at approximately 520 nm, which disappeared within a second (Figure 3.8a, red trace). The yellow luminescence (λ_{max} = 575 nm) turned on only after an inductive period. In another independent experiment, I observed that the yellow luminescence intensity increased in a sigmoidal manner as irradiation time advanced, indicative of the autocatalytic nature of the molecular process behind the luminescence evolution (Figure 3.8b).[48-50] The yellow emission matches the photoluminescence spectrum of the SCL state and can be ascribed to the RTP from the planar conformer (Figure 3.4).[31] Meanwhile, the initial green emission is assignable to the skew conformer because **SO** exhibits the skew conformation in the crystal (see below, Figure 3.9, Figure 3.16a).[31, 37–39] Therefore, the luminescence evolution reflects the local melting process, which involves the conformation change from skew to planar.[52-53]

Such conformation change is supported by Raman microscopy experiments (Figure 3.10). The Raman spectra of a liquid and a pristine crystal are shown in Figure 3.11a and the time-course of the Raman spectra under UV irradiation for a **SO** crystal are shown in Figure 3.10. The Raman spectrum of the crystal gradually changed and finally matched that of the SCL, which was prepared by removing solvents from the solution. Although I observed two intense peaks in the range between 1400–1500 cm^{-1}, those peaks are commonly appeared in all the isomers and cannot be used to distinguish isomers, according to the simulated spectra (Figure 3.11 and Figure 3.12). Nonetheless, the spectrum of the SCL was more complex than that of the pristine crystal, which suggested the existence of other conformers than the skew conformer (Figure 3.13 and Figure 3.11a). In particular, the peak in the range between 1600 and 1700 cm^{-1} became gradually rounded along UV irradiation. According to the simulated Raman spectra (Figure 3.11b), such spectral changes agree with the occurrence of the planar conformer.

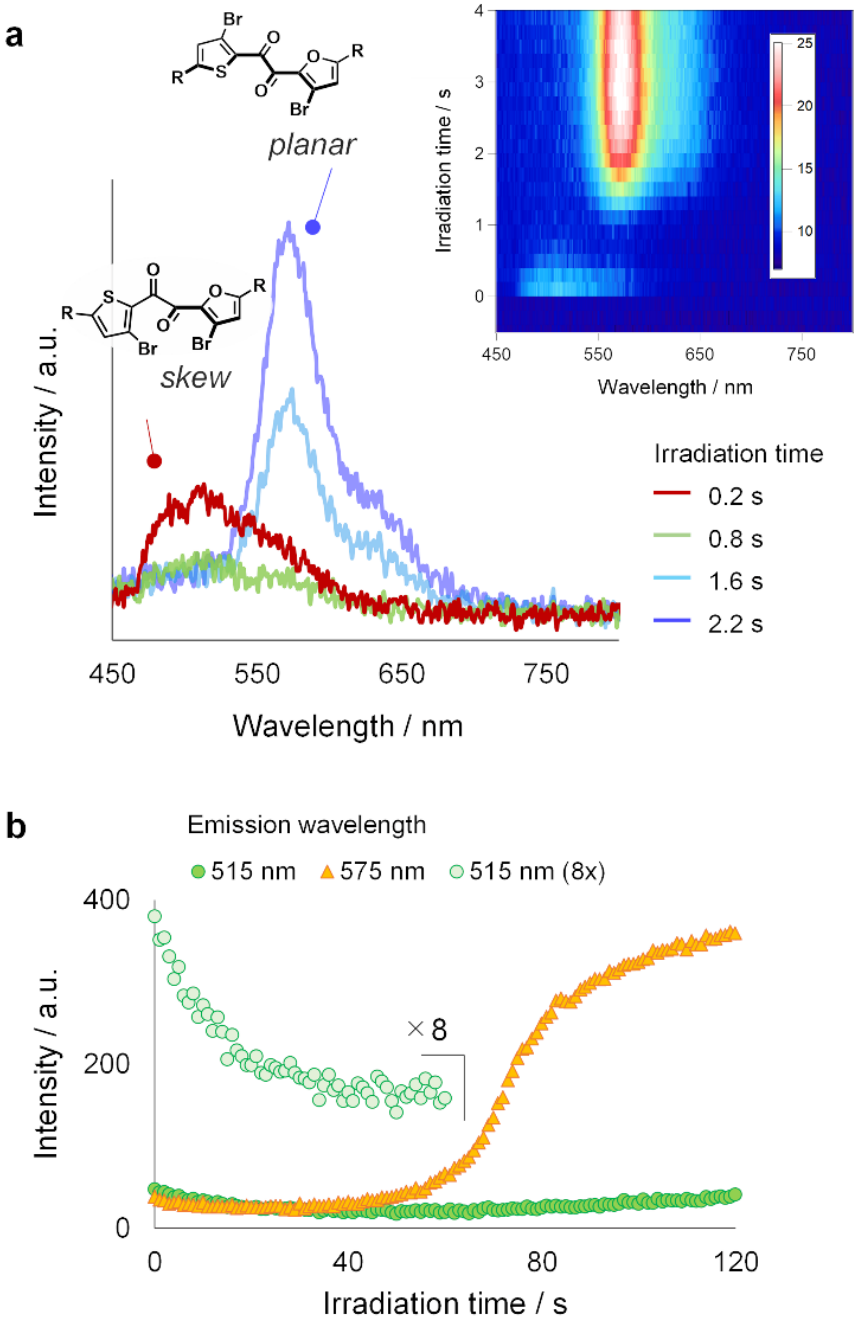

Figure 3.8. Time course of (a) photoluminescence spectra and (b) luminescence intensity (λ_{em} = 515 nm and 575 nm) of **SO** crystal during continuous UV irradiation. Note that crystal size and light source for panels (a) and (b) are different. Reproduced from ref II.

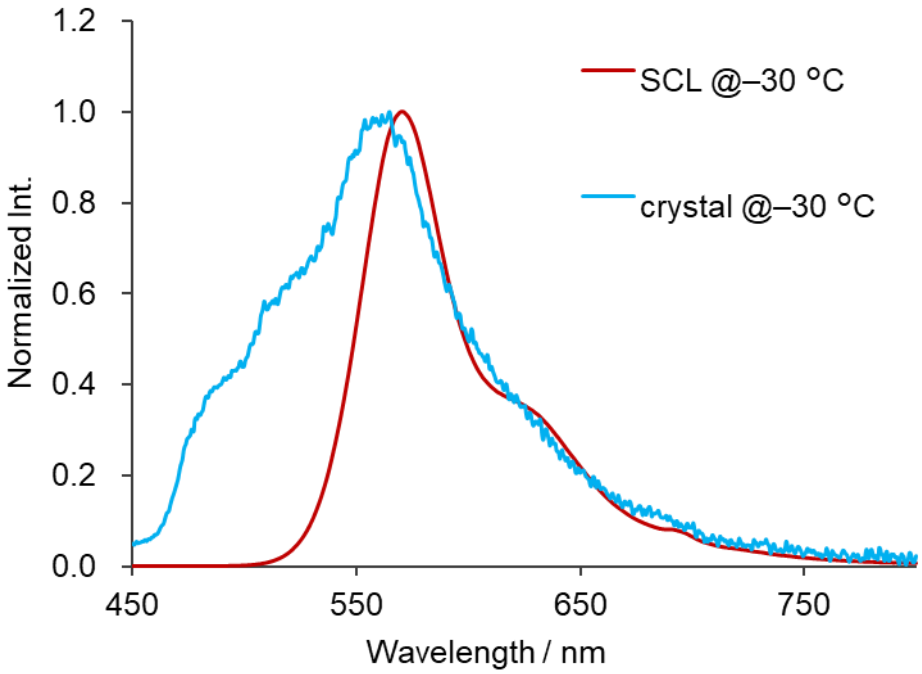

Figure 3.9. Normalized steady-state PL spectra of **SO** crystal and SCL in air at –30 °C. Reproduced from ref II.

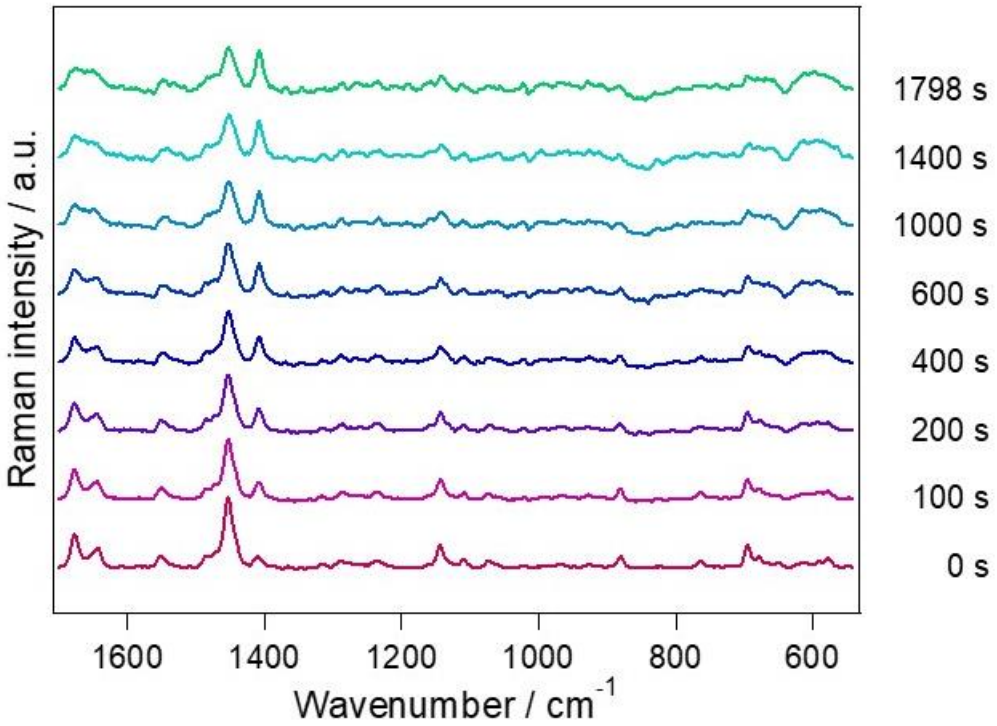

Figure 3.10. Time-course of the Raman spectra of **SO** crystal under UV irradiation. Reproduced from ref II.

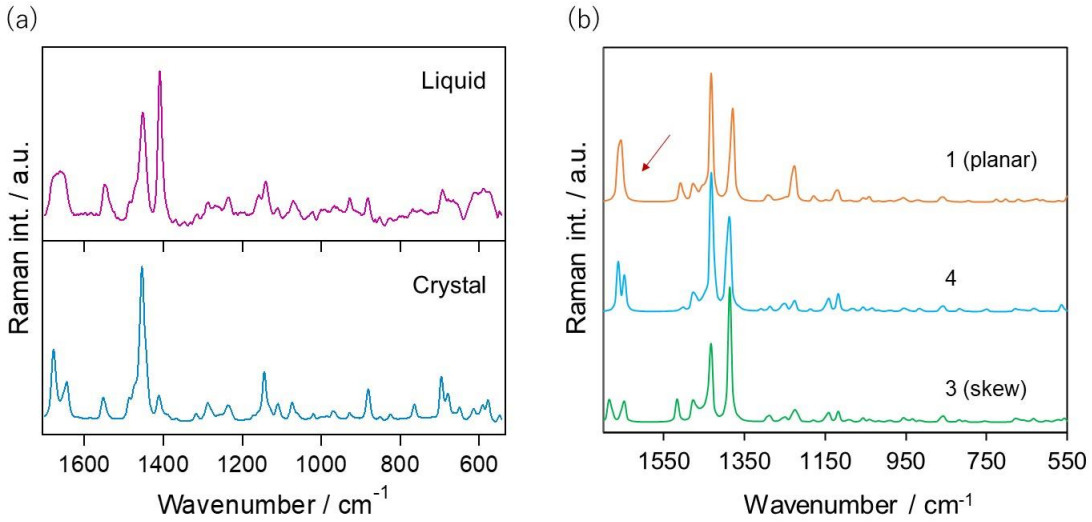

Figure 3.11. (a) Raman spectra of **SO** single crystal and liquid phases. (b) Simulated Raman spectra of **SO** conformers at the S_0-optimised geometries, calculated at the B3LYP-D3/6-311G(d) level of theory (Figure 3.12). Reproduced from ref II.

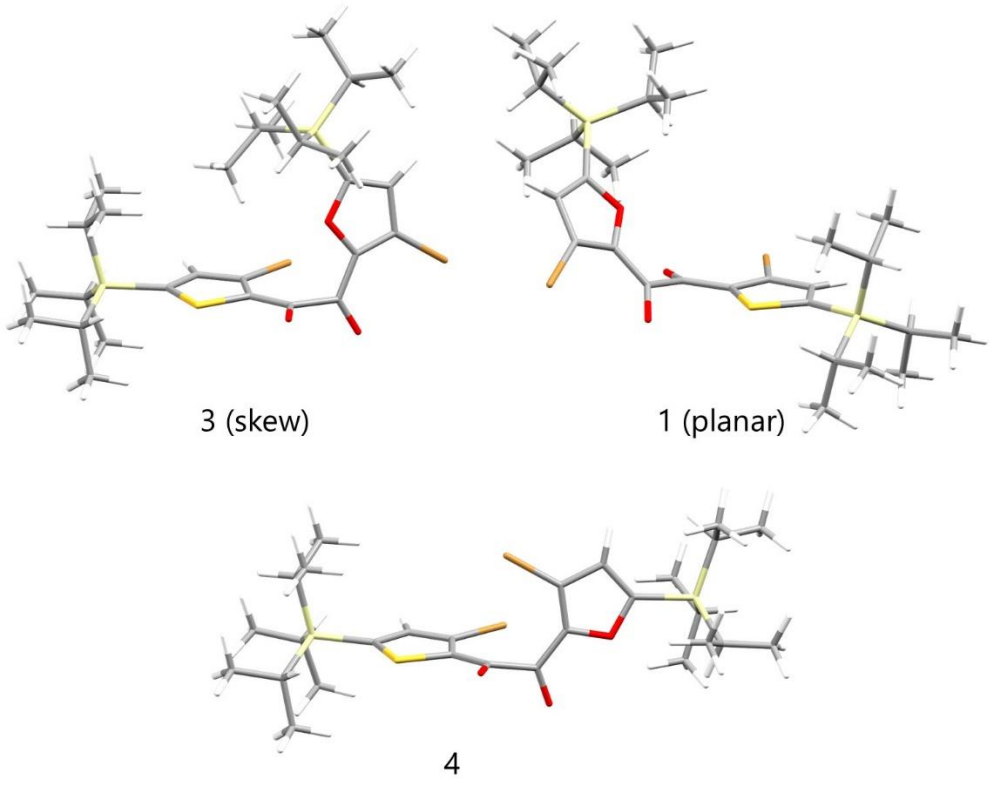

Figure 3.12. Optimized structures of **SO** conformers in S_0 state calculated at the B3LYP-D3/6-311G(d) level. Conformer 4 corresponds to the second conformer from the bottom in Figure 3.13. Reproduced from ref II.

3.2.2 Theoretical study on the conformational dynamics of SO

As discussed in Chapter 2,[31a] **SO′**, in which the silyl groups of **SO** are replaced with H, has a total eight conformers (each of the four conformers has (*S*) and (*R*)) within a 2 kcal mol^{-1} energy range. Among them, **SO′**-skew is the most stable at the ground state (Figure 3.13, Table 3.1). In contrast, at the T_1 state, the optimized **SO′**-planar is the most stable conformer (Table 3.1). Specifically, **SO′**-planar is more stable than **SO′**-skew by 3.9 kcal mol^{-1}. Note that the energy gap become 9.9 kcal mol^{-1} when considering the triisopropylsilyl substituents (i.e., **SO**-planar vs. **SO**-skew).

To gain insight into the dynamics in excited states, I scanned the coordinates around the thiophene–carbonyl bond starting from the (*S*)-**SO′**-planar in the ground state (Figure 3.14, the rotation axis is indicated as the green bond). The step of the scan was set to 20°. At each structure, single-point TD-DFT calculations were performed to obtain the S_1 and T_1 energy levels. From the results, I concluded that **SO′**-planar is accessible upon photoexcitation of **SO′**-skew, which corresponds to the conformer in the crystal.

To estimate the activation barrier of the conformational change between **SO′**-skew and **SO′**-planar, I calculated transition-state (TS) geometries in the ground and T_1 states. The obtained geometries were confirmed to be saddle-point structures that have one imaginary frequency. In addition, I displaced the saddle-point geometries along the mode with the imaginary frequency and subjected them to structure optimization. As a result, corresponding **SO′**-skew and **SO′**-planar structures in the corresponding electronic states[1a] were obtained. These results indicate that the obtained geometries are the TS for the conformational changes. The estimated Gibbs energy of activation from **SO′**-skew to **SO′**-planar in the T_1 state is quite small (2.4 kcal/mol) while that for the backward conformation change in the ground state (i.e., from **SO′**-planar to **SO′**-skew) is also small (Figure 3.14, Figure 3.18b, and Figure 3.15).

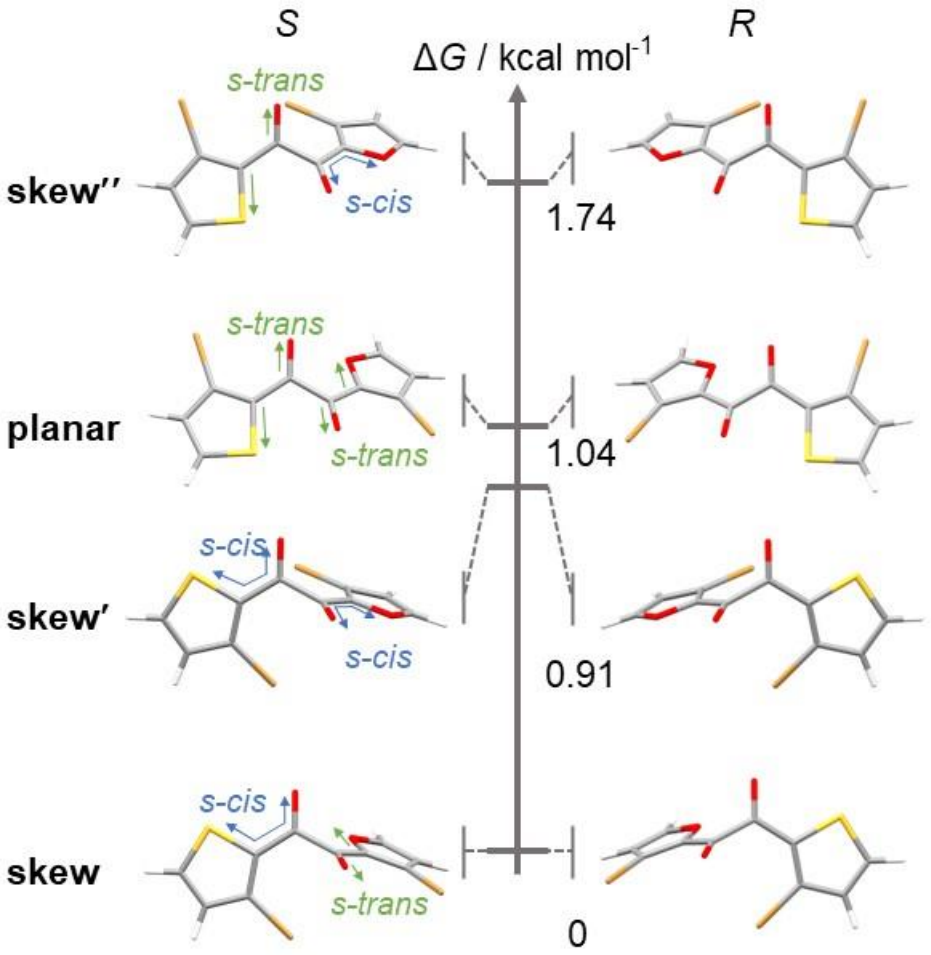

Figure 3.13. Optimized structures and energy levels of eight conformers of **SO′** in the S_0 state calculated at the B3LYP-D3/6-311G(d) level of theory. Reproduced from ref II.

Table 3.1. The relative Gibbs free energies (ΔG) of four conformers of **SO′** and the corresponding dihedral angles (θ) of the two carbonyls. The energies include thermal correction at 298.150 K. Reproduced from ref II.

	S_0 opt		T_1 opt	
	ΔG / kcal mol^{-1}	θ / °	ΔG / kcal mol^{-1}	θ / °
skew	0	97	3.87	166
skew′	0.91	95	5.60	159
skew″	1.74	123	2.64	168
planar	1.04	135	0	180

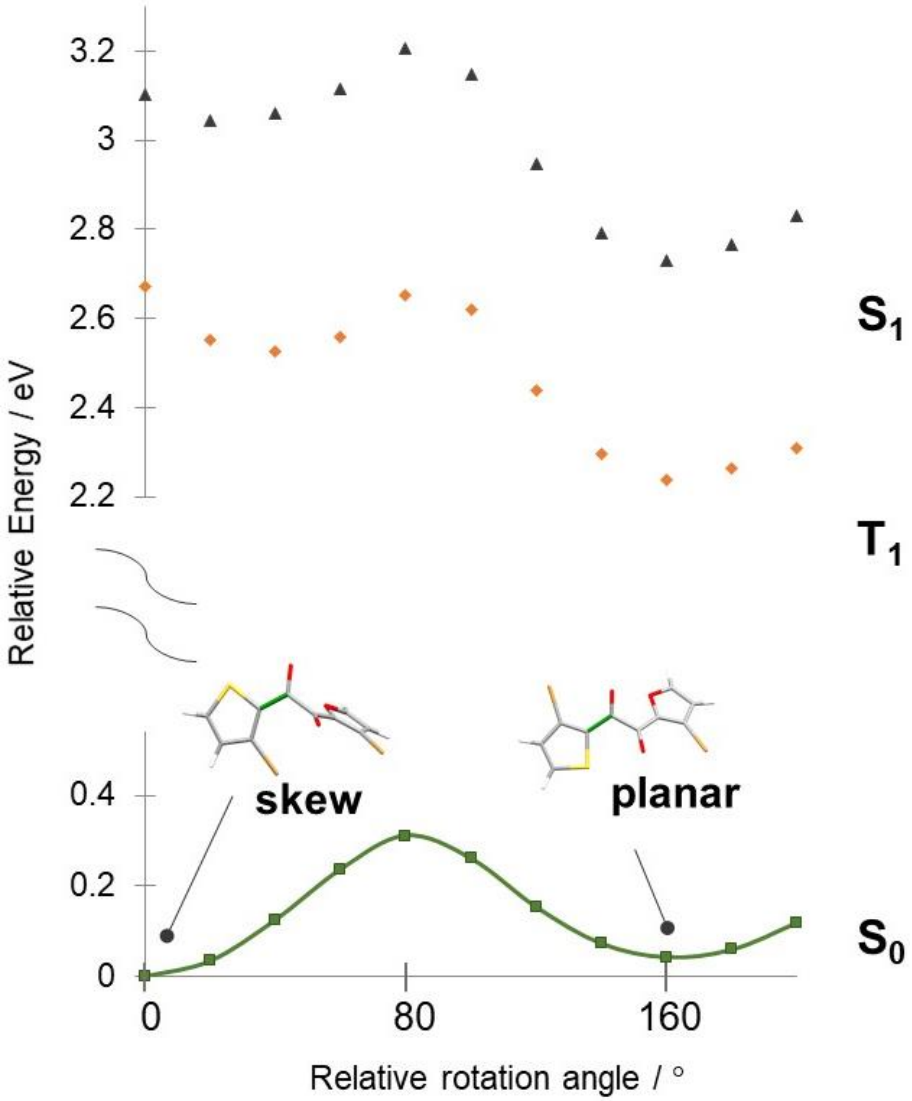

Figure 3.14. Potential energy curve of isolated (*S*)-**SO′** along the rotation around the green bond calculated at the B3LYP-D3/6-311G(d) level with a step of 20 °. Energies for S_1 (black triangle) and T_1 states (orange diamond) were calculated for vertical excitation. Reproduced from ref II.

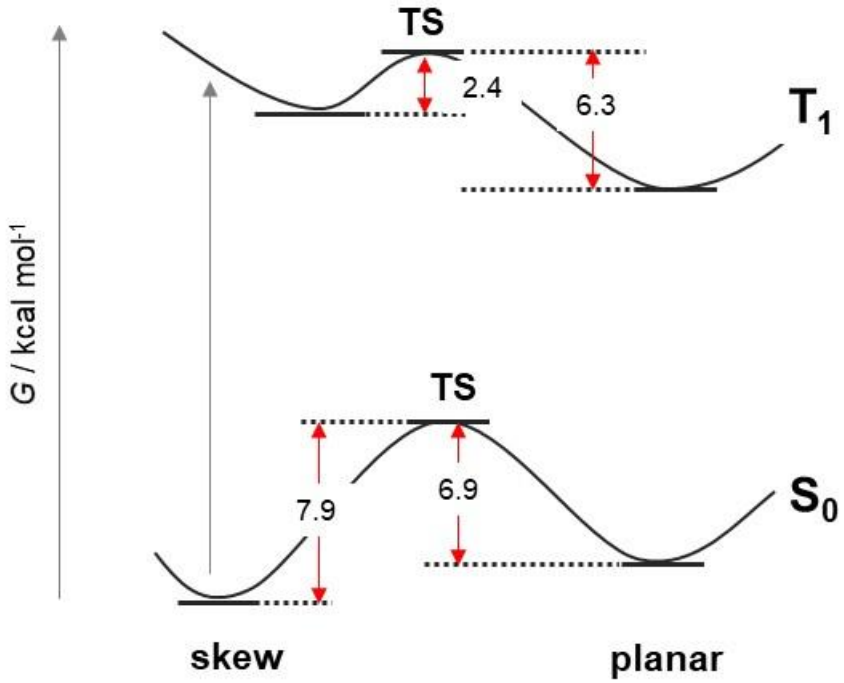

Figure 3.15. Summary of the calculated Gibbs energies of activation for the conformational change of **SO′**. Reproduced from ref II.

3.2.3 Correlation between crystal structure and PCLT

Although it is evident that the molecular conformation changes from skew to planar in the crystal, how such a large structural change proceeds is unclear. To elucidate the details of the large structural change, I investigated the crystal structure and examined its relaxation after UV excitation. I successfully performed a single-crystal X-ray structural analysis of **SO** at 300 K (Figure 3.16a and Figure 3.17). Compared to the structure at 123 K,[31a] the thermal ellipsoids become large particularly in the silyl moieties. The packing structure shows that the silyl moieties form disordered layers along the (10–1) planes, while the heteroaromatic 1,2-diketone cores are relatively more ordered (Figure 3.16b).[54] Furthermore, according to density functional theory (DFT) calculations, the silyl moiety moves along the disordered (10–1) planes upon the excited-state structural relaxation, which is smaller than the skew-to-planar conformational change (Figure 3.14 and Figure 3.18). Therefore, the mechanical stress in the crystal upon relaxation is relatively small and is mitigated by the disordered layer; thus, the relaxation is allowed, thereby accelerating the disordering of the entire crystal. The photoinduced loosening of the crystal was confirmed by comparing single-crystal X-ray structures before and after UV irradiation. Thus, the equivalent isotropic atomic displacement parameters (U_{eq}), which represent the size of the thermal ellipsoid and hence the degree of disorder, became large by UV irradiation for 33 out of 36 atoms; the increase rates were up to 6% (Figure 3.19). In general, the RTP disappears when the ordered

crystalline lattice is disturbed.[32-34] Therefore, the disappearance of the skew emission is due to pronounced nonradiative decay and indicates crystal loosening owing to UV irradiation.[37] Moreover, the sigmoidal increase of the planar emission intensity after the inductive period (Figure 3.8b) indicates that the formation of the planar conformer is autocatalytic, and crystal loosening is necessary to overcome the barrier for it.[48-50]

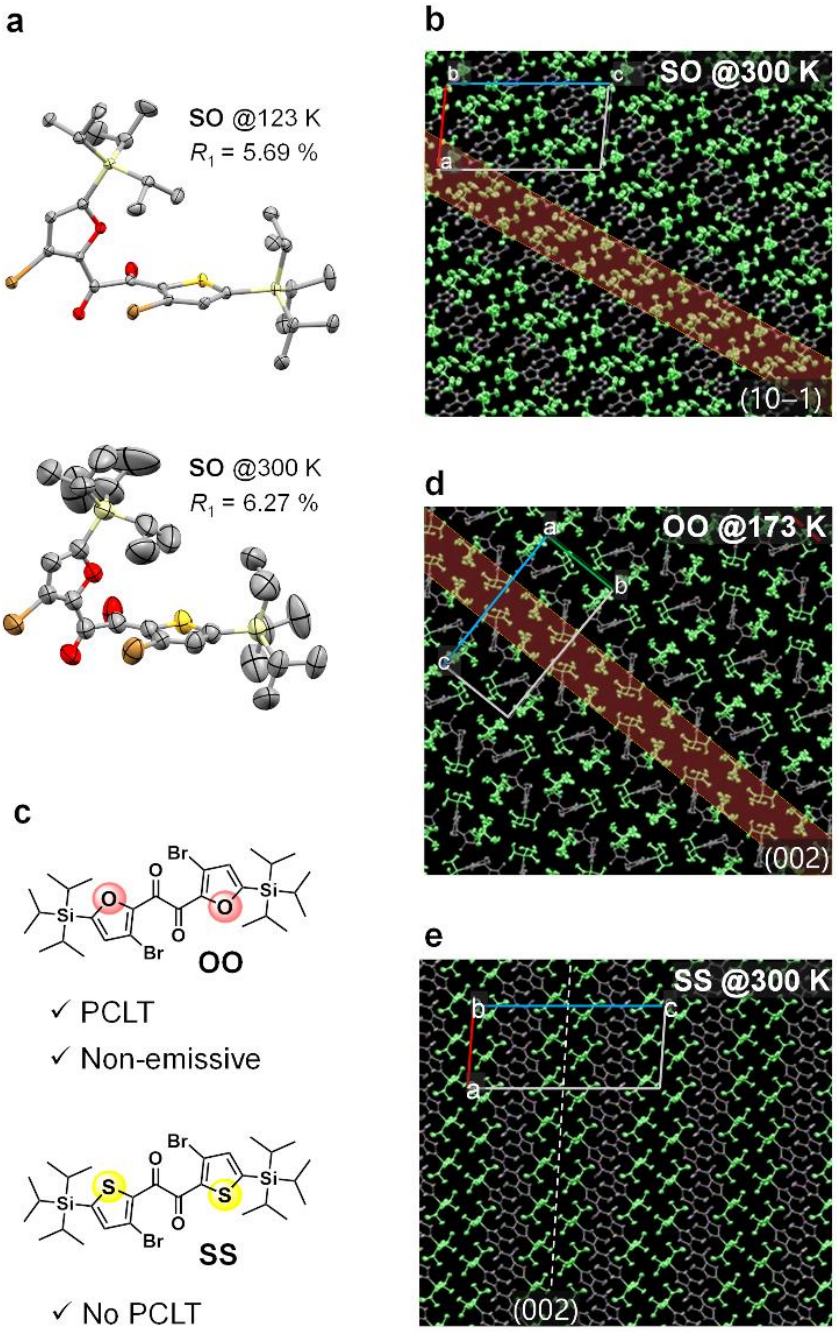

Figure 3.16. ORTEP drawings of (a) molecular structures of **SO** at 123 and 300 K and packing structure of (b) **SO** at 300 K, (d) **OO** at 173 K, and (e) **SS** at 300 K. Thermal ellipsoids are set at 50% probability level, and hydrogen atoms are omitted for clarity. In the panels b, d, and e, the silyl moieties and diketone cores are drawn in green and grey, respectively. The disordered layers along the lattice plane facing silyl moieties are highlighted. (c) Chemical structures of **OO** and **SS**. Reproduced from ref II.

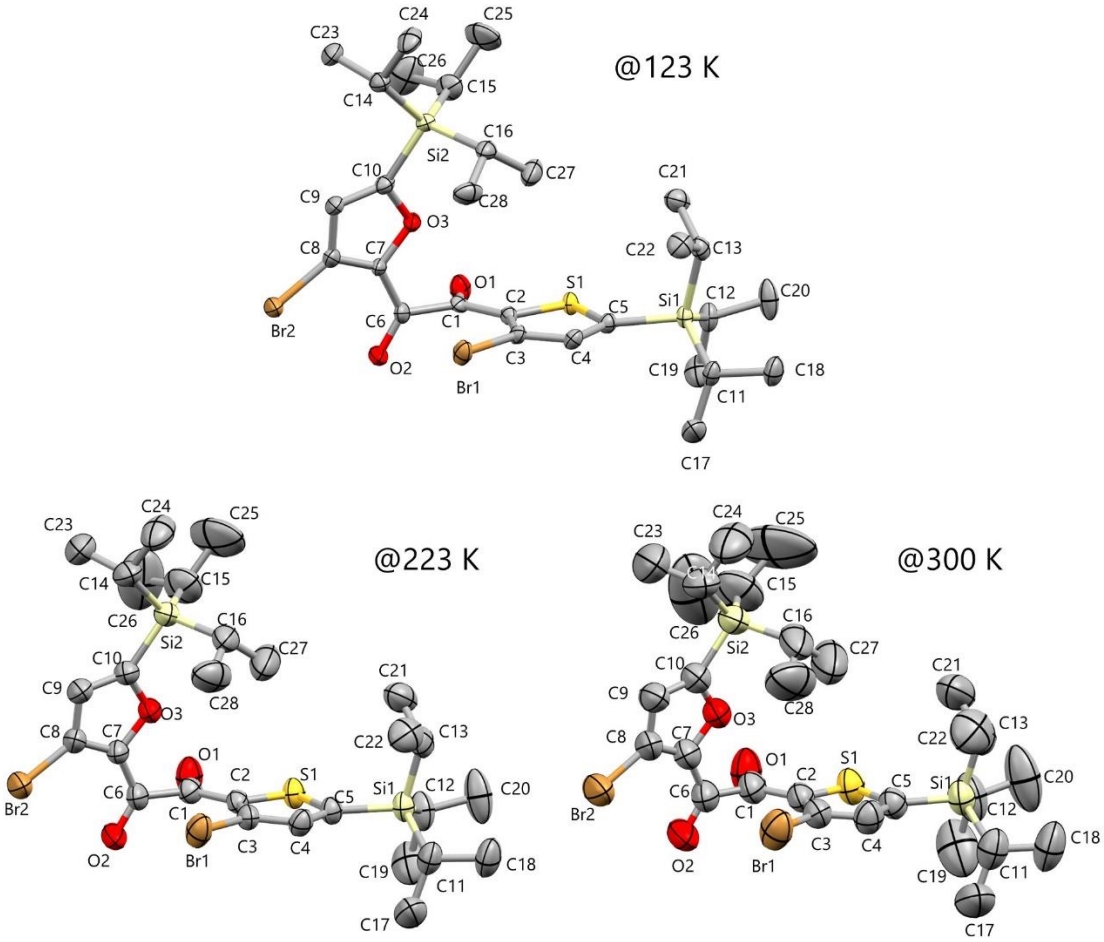

Figure 3.17. ORTEP drawing of the single-crystal X-ray structures of **SO** at various temperatures. Hydrogen atoms are omitted for clarity, and the thermal ellipsoids are set at the 50% probability level. Reproduced from ref II.

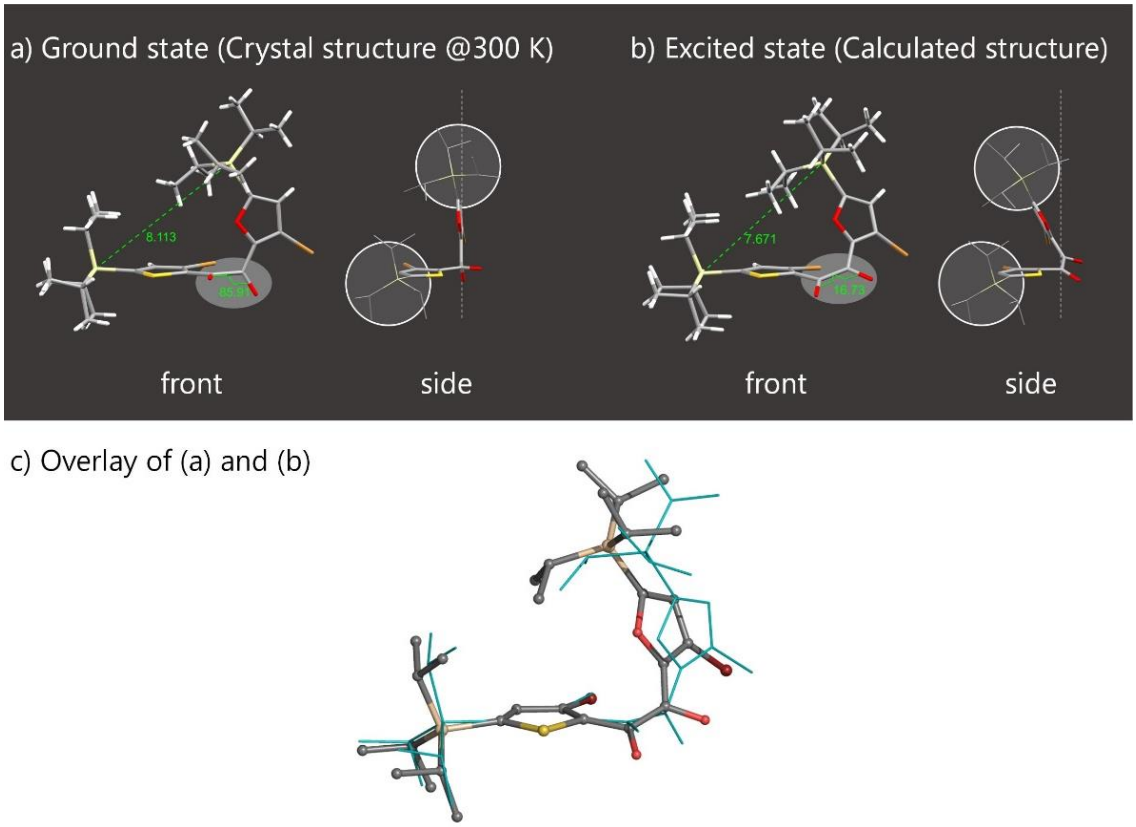

Figure 3.18. (a) Crystal structure at 300 K and (b) T_1-optimized relaxed skew structure calculated at the UB3LYP-D3/6-311G(d) level of theory. (c) Overlay of the crystal structure (a, cyan line) and the T_1-optimized structure (b, capped stick model). Reproduced from ref II.

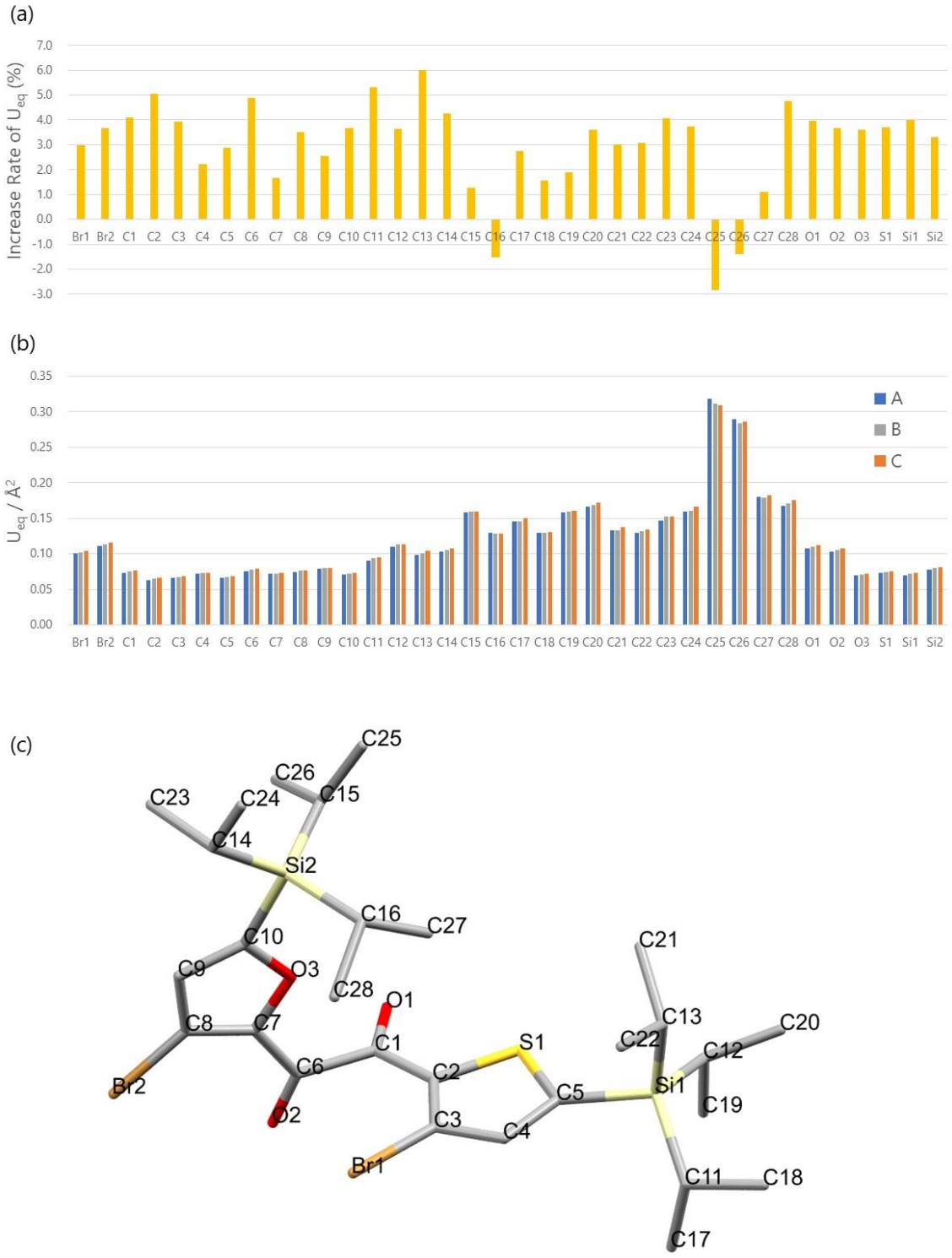

Figure 3.19. (a) Increase rate of U_{eq} from A to C. (b) U_{eq} of A, B, and C. (c) Crystal structure of C with atom numbering. Reproduced from ref II.

To gain further insights into the factors controlling PCLT, I examined the photoresponse and crystal structures of the analogous diketones **OO** and **SS** (Figure 3.16c). Despite the similarity in their chemical structures, with only one atom being different, their crystals responded differently upon UV irradiation; PCLT did not occur in the case of the **SS** crystal, while the **OO** crystal melted (without luminescence) (Figure 3.20 and Figure 3.21). Single-crystal X-ray structural analysis revealed that **OO** exhibits packing features similar to those of **SO**, while **SS** does not (Figure 3.16b, 3.17d, and 3.17e). Thus, while all three diketones have a lattice plane facing the silyl moieties, in the cases of **SO** and **OO**, the two silyl moieties within a single molecule face the same plane, whereas in **SS**, they face a different plane. Moreover, the silyl moieties of **SO** and **OO** are disordered, while those of **SS** are well ordered even at room temperature (Figure 3.16e and Figure 3.22). These results further confirm the importance of a crystal structure with a disordered layer for a molecular crystal to be PCLT-active.[5-54]

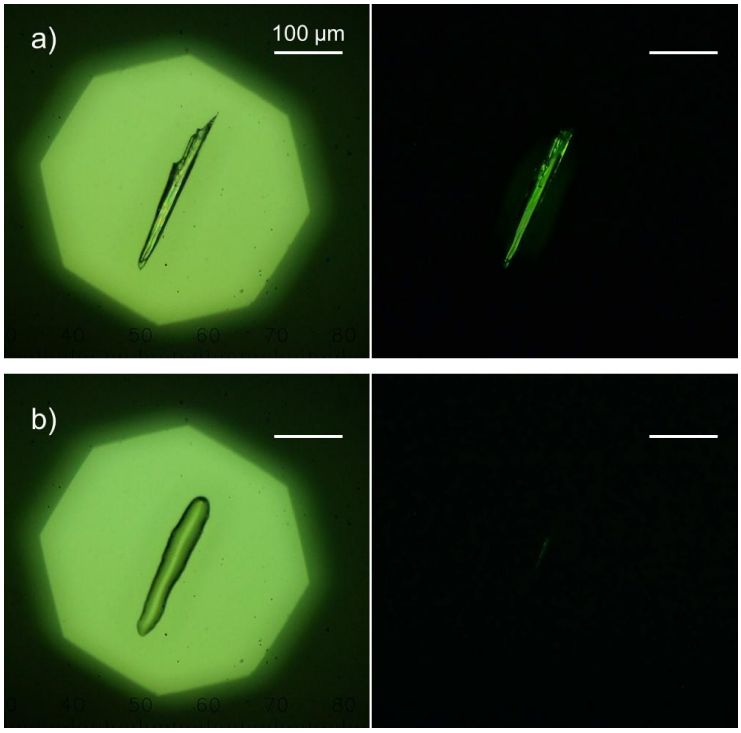

Figure 3.20. Photographic images of **OO** crystal under (left) bright-field and (right) polarizing optical microscopes with crossed Nichol prisms (a) before irradiation and (b) after continuous UV-light irradiation for 1 min. Reproduced from ref II.

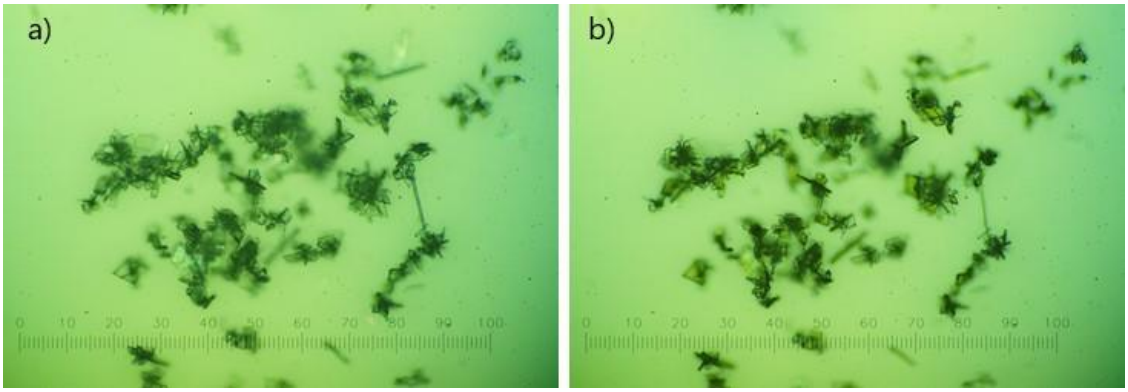

Figure 3.21. Photographic images of **SS** crystal under bright-field microscope (a) before irradiation and (b) after continuous UV-light irradiation for 11 h. Scale bar = 1 mm. Reproduced from ref II.

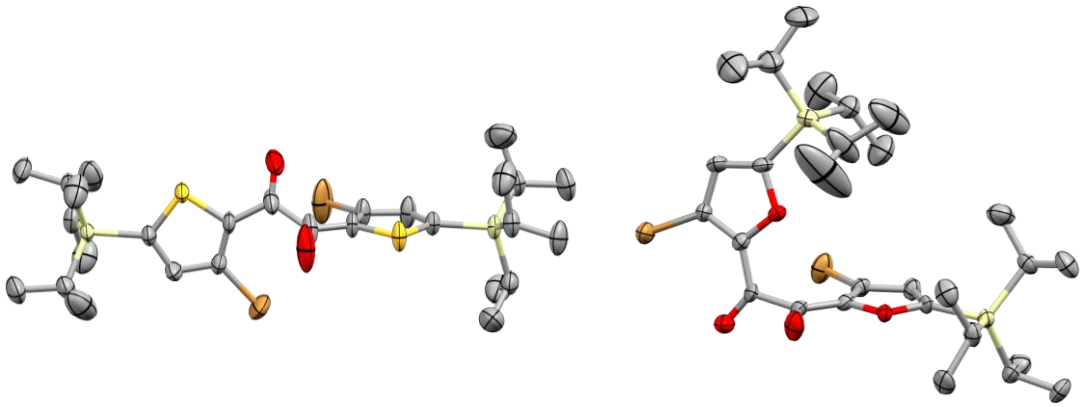

Figure 3.22. ORTEP drawing **SS** (left) at 300 K and **OO** (right) at 173 K. Thermal ellipsoids are set at 50 % probability level. Reproduced from ref II.

Energetically, the skew-to-planar photoisomerization is favorable in all three diketones (Table 3.2). However, the barrier to the structural change should increase if the intermolecular interactions in the crystals increase. Using differential scanning calorimetry (DSC), the enthalpy of fusion (ΔH_m) values of the **SO**, **OO**, and **SS** crystals were determined to be 22, 29, and 40 kJ mol^{-1}, respectively (Figure 3.23–Figure 3.25). The values for **SO** and **OO** were significantly smaller, indicating that the intermolecular interactions in these PCLT-active crystals were weaker. The differences in ΔH_m reflect the different packing features, which is due to the different molecular conformations in the crystals (Figure 3.16, Figure 3.22, and Figure 3.26). **SO**, **OO**, and **SS** exhibited skewness with respect to the dicarbonyl moiety. However, their conformations differ with respect to the twist angle between one of the aromatic rings and the adjacent carbonyl group: C–S (or C–O) and C=O are s-*cis* in the case of **SS** and s-*trans* in the cases of **SO** and **OO** (Figure

3.16a and Figure 3.22). Different conformations in the crystal can be due to the relative stability of the two skew conformers, which is dictated by a steric effect. Thiophene and furan are geometrically different due to the different bond length/angle around the heteroatom. In particular, the exocyclic bond angles of 2- and 3-positions are approximately 71.6° and 80.4° for thiophene and furan, respectively. Consequently, in the *s-trans* arrangement, the carbonyl oxygen becomes closer to the bromine atoms in **SS** (thiophene) than in **SO** and **OO** (furan); the calculated Br–O distance is shorter than the sum of their van der Waals radii (3.35 Å) in **SS′** (Figure 3.26). This steric hindrance destabilizes the s-*cis* arrangement of **SS**. As a result of these s-*cis*/s-*trans* conformation differences, **SS** has a rod-like shape while **SO** and **OO** are spherical. The spherical shape reduces the specific surface area and packing density, thereby decreasing the strength of the van der Waals interactions. These conclusions were confirmed quantitatively based on a Hirshfeld surface analysis (Figure 3.27)[55] and partly explain why the enthalpies of fusion (and hence the intermolecular interactions) of the **SO** and **OO** crystals are smaller than that of the **SS** crystal. In addition, the two silyl groups of **SO** and **OO** are on one side of the molecule while those of **SS** are located at the two ends of its rod-like structure. This asymmetrical distribution of the C–H-bond-rich surface may be critical to the formation of the characteristic packing structure of **SO** and **OO**. Moreover, conformational changes require the rod-like structure of **SS** to be bent against the stronger intermolecular interactions between the core skeletons. Therefore, it can be assumed that **SS** requires more energy for relaxation/isomerization than do **SO** and **OO**.

Moreover, the Gibbs free energies for the crystal-to-SCL transition at 300 K for **SO**, **OO**, and **SS** were estimated to be 2.2, 2.7, and 12 kJ mol^{-1}, respectively. Clearly, PCLT is less endothermic in the cases of **SO** and **OO**. These results suggest that a subtle atomic replacement can significantly modulate the bulk thermal properties, resulting in PCLT in aromatic 1,2-diketones.

Table 3.2 The Gibbs free energies (ΔG) of the planar conformer relative to the (relaxed) skew conformer at the T_1-optimized geometries

Diketone	ΔG / kcal mol^{-1} [a]
SO	–9.89
OO	–8.35
SS	–6.38

[a] The energies include thermal correction at 298.150 K.

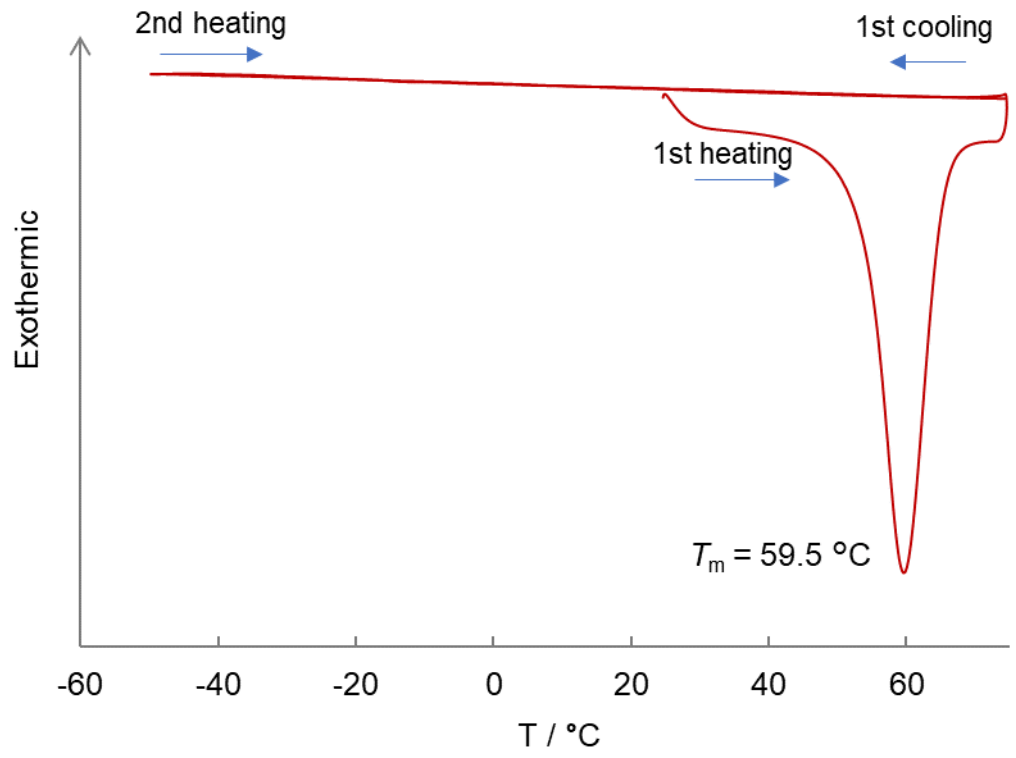

Figure 3.23. DSC thermogram of **SO** during heating/cooling cycles at 10 °C min^{-1} for the 1st heating and at 0.3 °C min^{-1} for the 1st cooling and 2nd heating processes, under a flow of N_2. Reproduced from ref II.

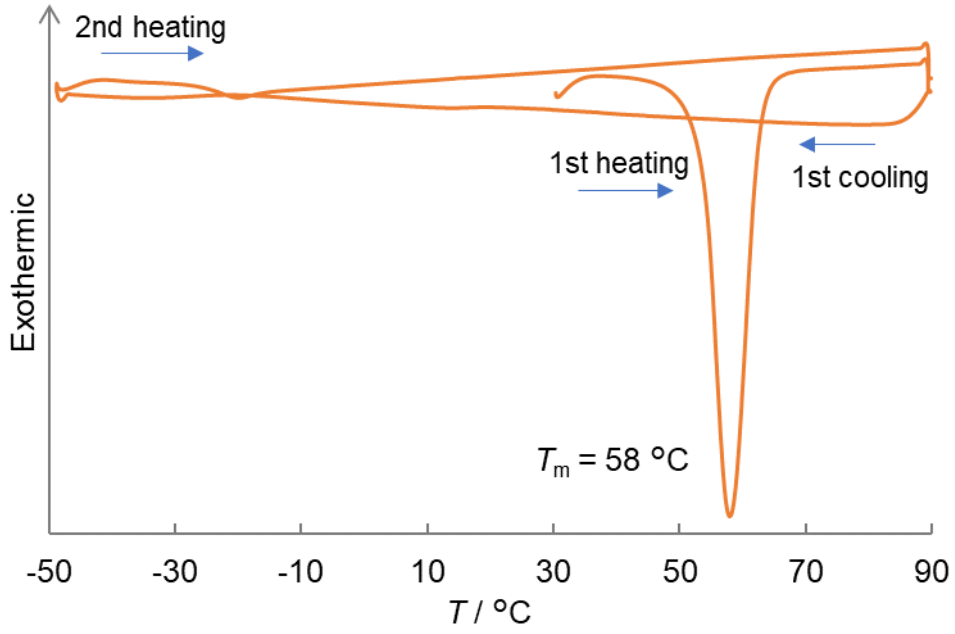

Figure 3.24. DSC thermogram of **OO** solid during heating/cooling cycles at 10 °C min^{-1} under a flow of N_2. Reproduced from ref II.

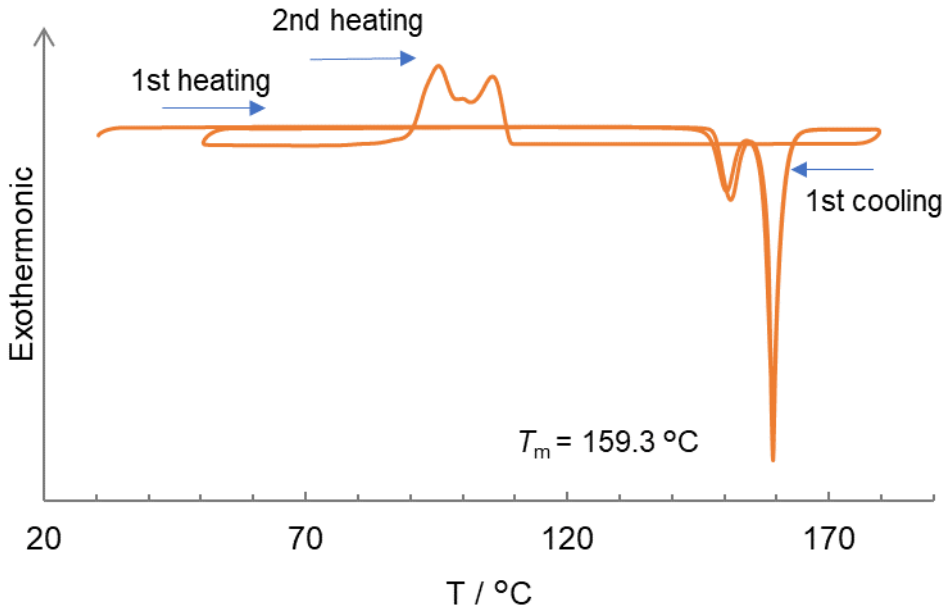

Figure 3.25. DSC thermogram of solid **SS** during heating/cooling cycles at 10 °C min^{-1} under a flow of N_2. Reproduced from ref II.

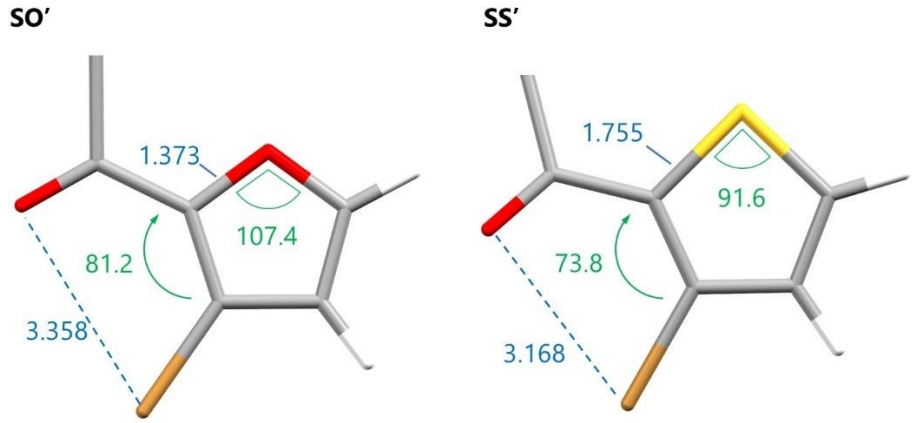

Figure 3.26. The optimized geometries, selected bond lengths (Å), distances (Å), and angles (°) of the *s-trans* conformers for **SO′** and **SS′** in the S_0 state calculated at the B3LYP-D3/6-311G(d) level of theory (only half of the molecules was shown). Reproduced from ref II.

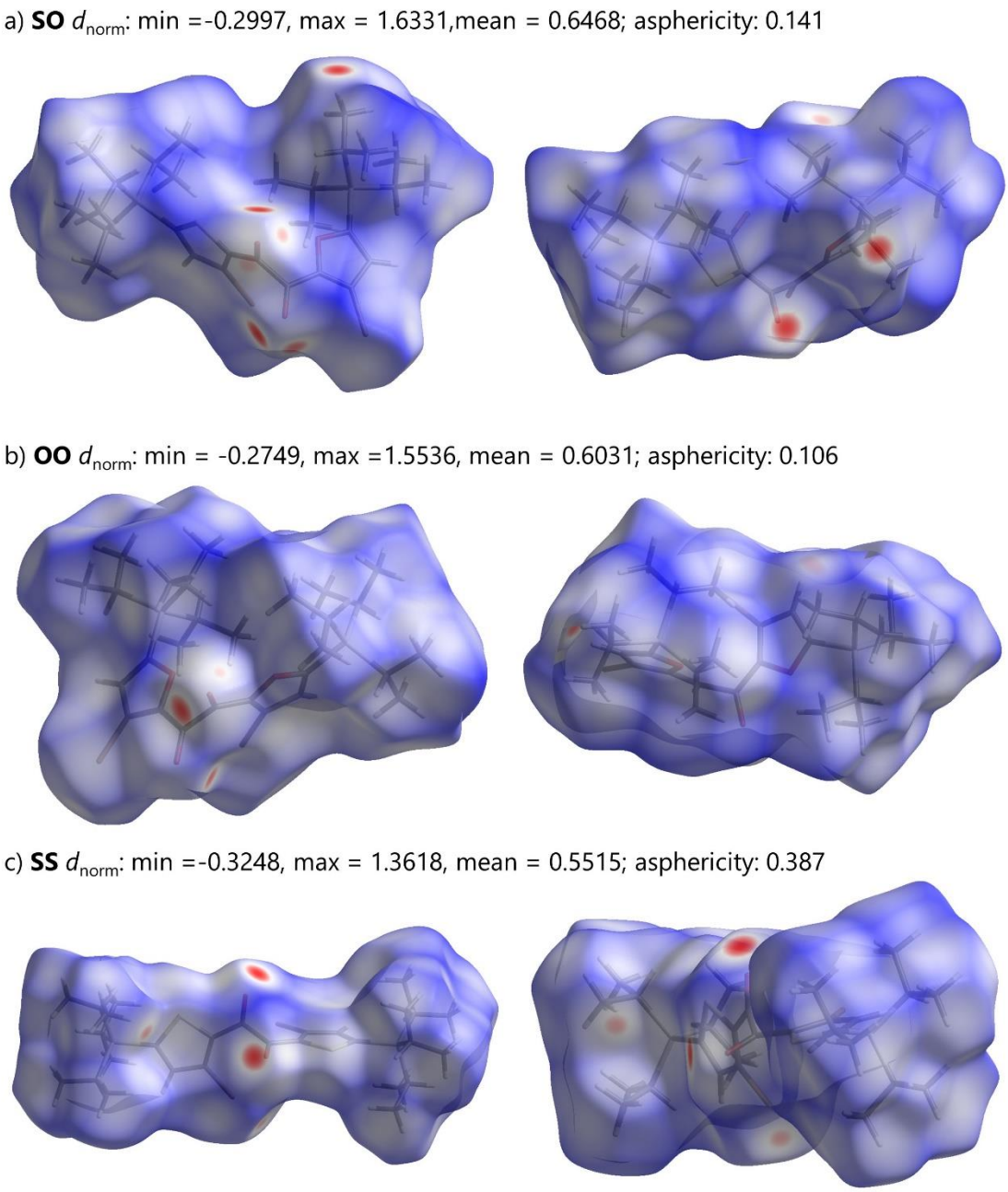

Figure 3.27. Hirshfeld surface of (a) **SO**, (b) **OO**, and (c) **SS** mapped with d_{norm} (mapped over a fixed color scale of –0.3 (red) to 1.7 (blue)). The surfaces as well as the minima, maxima, and mean values of d_{norm}, and a sphericity were obtained by CrystalExplorer21.[55] Reproduced from ref II.

3.2.4 A plausible PCLT mechanism of SO crystal

Based on these results, a possible total three-step process for PCLT in the **SO** crystal is suggested (Figure 3.28). Initially, the **SO** crystal exhibits a weak emission at 520 nm, which originates from

the skew conformation. As the first step, the crystal packing is loosened because of the photoinduced conformational relaxation. The loosening is evident from the disappearance of the skew emission and single-crystal X-ray structure analyses. Meanwhile, as the second step, the loosening allows a larger conformational change to generate the planar conformer, providing the yellow RTP (microscopic melting). These events can be regarded as premelting, as they occur while the bulk substance is still solid. The presence of an inductive period and the sigmoidal response of the yellow RTP indicates that the skew-to-planar conformational change is impossible at first; the loosening of the crystal packing through the smaller conformational relaxation is necessary beforehand. These conformational changes further loosen the crystal packing and promote subsequent conformational changes, which occurs repeatedly in an autocatalytic manner, finally leading to greater disordering in the longer range and the eventual macroscopic melting of the bulk crystal (the third step). Thus, the two-step changes in the luminescence of the PCLT-active crystal allowed the visualization of its molecular-level melting process in real-time. It should be worth noting that, to induce PCLT, photoexcited molecules within the crystal must undergo a structural change. However, the dilemma exists that relatively small structural changes, which are comparatively easier to occur, rarely lead to phase transitions. Conversely, larger structural changes that could lead to phase transitions are hard to occur in the crystal. It would be this dilemma that limits the diversity of the PCLT-active compounds. In contrast, PCLT of the diketones occurred not in one step but involved two types of structural changes that induce disordering. Such a PCLT mechanism can avoid the dilemma and diversify the molecular design of PCLT-active materials.

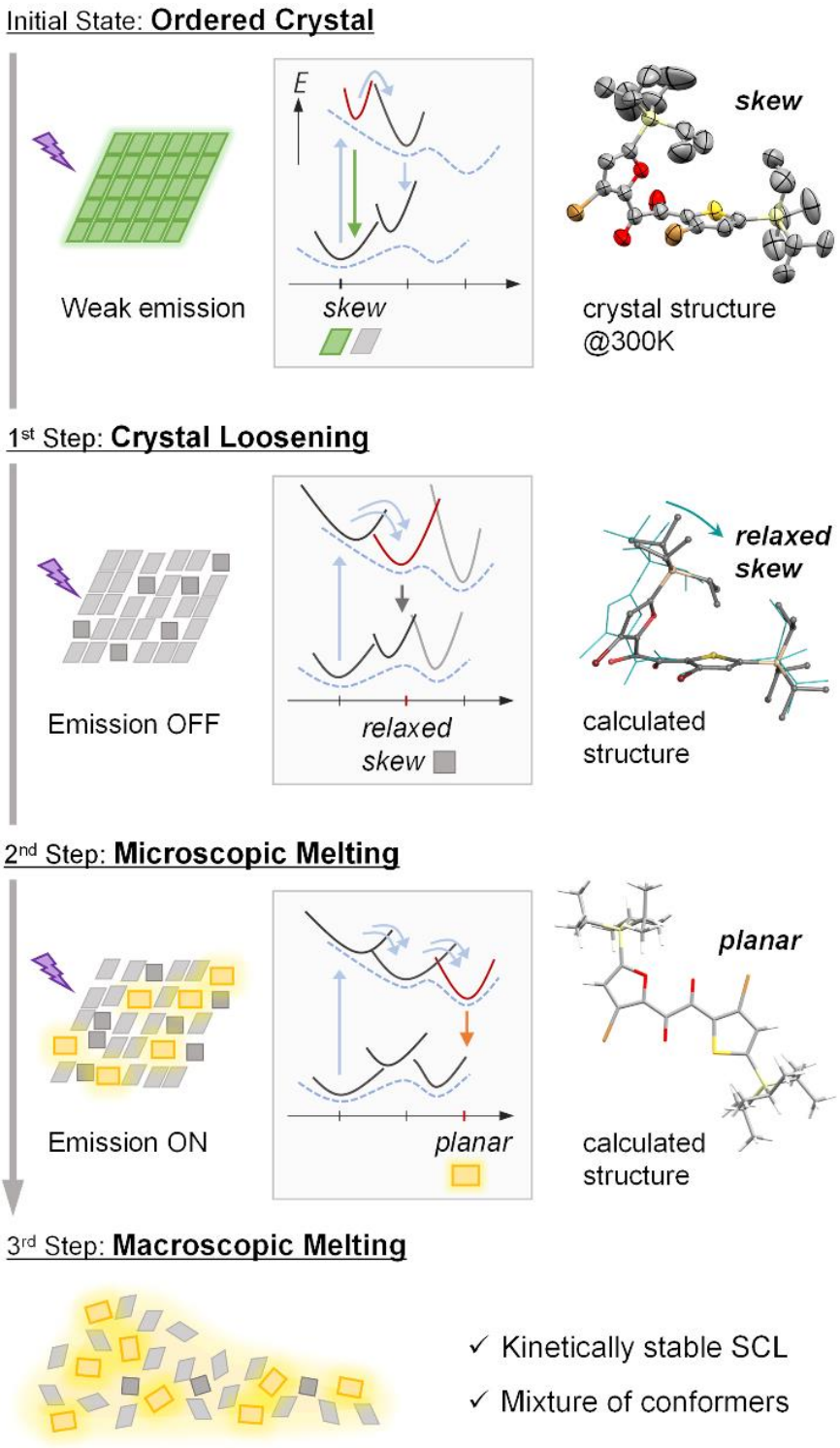

Figure 3.28. Schematic illustration of plausible PCLT mechanism. Left: the disordering crystal packing with luminescence properties. Panels on the middle: the potential energy curves, with solid lines for the molecules in crystal and broken lines for isolated molecules. Right: the corresponding molecular conformations. Reproduced from ref II.

The proposed PCLT mechanism is based on a conformational change around the single bonds. Meanwhile, the reported mechanisms for the PCLT of photochromic molecules are based on the double-bond *E*/*Z* isomerization[1-12] or the cleavage/formation of the σ-bond.[16] These photoreactions have a high energy barrier for the thermal back reaction in the ground state, so that those conventional motifs are photochromic as an isolated molecule. In contrast, the barrier for the backward reaction of **SO** is not high (calculated to be 6.86 kcal mol^{-1} in vacuum, Figure 3.15). Nonetheless, the SCL state of **SO** exhibits exceptionally high kinetic stability (greater than 3 months). I had previously demonstrated that SCLs do not crystallize readily even in the presence of crystal seeds.[31] This is likely because the diketone core has at least eight conformers, including axially chiral enantiomers (Figure 3.13). Moreover, the zero-shear viscosity of **SO** SCL was 45 ± 2 Pa·s at room temperature, which is four orders of magnitude thicker than conventional organic solvents.[31] Such a highly viscous environment slows down the conformation changes and the translational and rotational motions of the molecules, resulting in the slow kinetics of assembling and aligning molecules to form crystals. Thus, the backward recrystallisation process is extremely slow to compete with the melting process. Indeed, even at the earliest stage of the PCLT, it is virtually irreversible within a reasonable time range. The photoluminescence spectra did not change after keeping the specimen in the dark for 20 min after ceasing UV irradiation at the first step of PCLT (Figure 3.29). The elucidation of this mechanism should help improve the molecular design of PCLT-active materials and lead to the development of materials other than the conventional photochromic motifs.

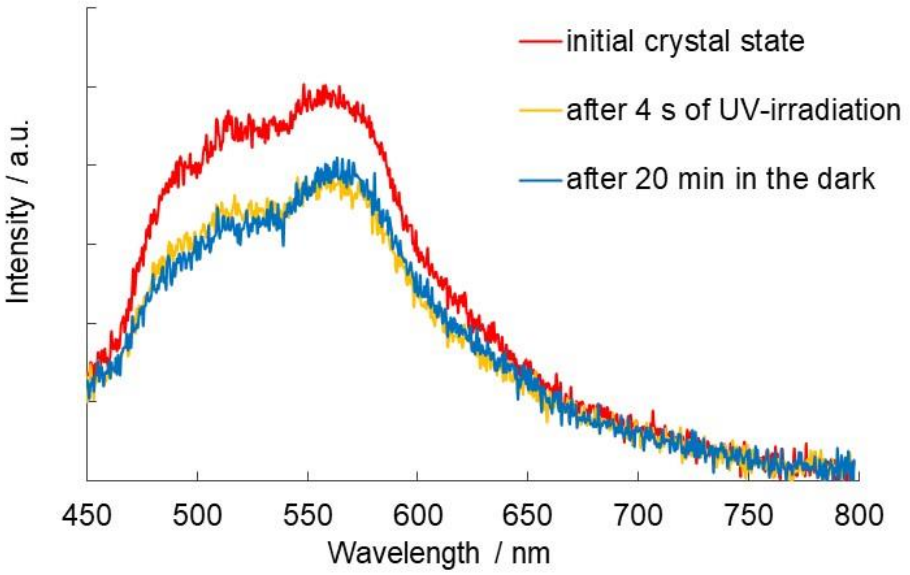

Figure 3.29. Photoluminescence spectra of **SO** under fluorescence microscope. Reproduced from ref II.

3.3 Summary of Chapter 3

In summary, I present the photo-induced crystal-liquid transition (PCLT) of heteroaromatic 1,2-diketones. In particular, diketone **SO** exhibits PCLT accompanied by luminescence evolution. Thus, the dynamic multistep changes in the luminescence color and intensity visualized the PCLT process involving two-step conformation changes, which furthers my understanding of the melting phenomenon at the molecular level. Based on the results and comparisons with the other two diketone derivatives, I clarified that the presence of a disordered layer in a crystal is an important factor for PCLT in diketone scaffolds. It should be noted that unlike the PCLT of conventional photochromic motifs, such as azobenzenes, the diketone demonstrates PCLT based on conformational isomerization, i.e., rotation around single bonds. Considering that various photofunctional molecules are not photochromic as a single molecule but exhibit considerable structural changes at the excited states, this work should lead to the diversification and multifunctionalization of PCLT-active motifs.

3.4 Experimental section

3.4.1 Instrumentation and chemicals

All the diketone derivatives (**SO**[31], **OO**[31], and **SS** [38]) were synthesized and confirmed to be highly pure using previously reported methods. The crystal samples were prepared through recrystallization by cooling a MeOH solution. UV-vis absorption and photoluminescence (PL) spectra were recorded at room temperature (RT) in air unless noted otherwise. The UV-vis absorption spectra were acquired using a Shimadzu UV-3150 spectrometer. PL spectra of the crystals and the supercooled liquid (SCL) were acquired using a JASCO FP-8200 spectrofluorometer. PL spectral tracking during the photo-induced crystal-to-liquid transition (PCLT) was performed using instrumentation A or B: (A) an OLYMPUS BX60M fluorescence microscope equipped with a Ushio 100 W ultrahigh-pressure mercury lamp (USH-102D), OLYMPUS mirror units (U-MWUS, λ_{max} = 365 nm, 60 mW cm^{-2}), and a HAMAMATSU Photonics PMA-12 photonic multichannel analyzer (C14631-01) and (B) a laboratory-built hyperspectral imaging system, which is described below (see Figure 3.30). Photographic images and movies were recorded using a SONY NEX-5N camera attached to the OLYMPUS BX60M fluorescence microscope with a MICRONET NY-1S adaptor unless noted otherwise. An OLYMPUS mirror unit (U-MBFL3, longpass, λ > 400 nm, < 10 mW cm^{-2}) was used for recording the bright-field and polarizing images while a U-MWUS or U-MWBS (λ = 460 to 490 nm) unit was used for the PL images.

3.4.2 Details of the laboratory-built hyperspectral imaging system

The illumination light source was an ultraviolet light emitting device (LED, Thorlabs, M365L2) centered at 365 nm, and its output was used for initiation of PCLT and photoexcitation of the sample to induce the emission. The **SO** crystal on the cover slip was placed on a 3-axis XYZ translation stage (OptoSigma, TSD-1202SH-M6 and Thorlabs, NFL5DP20/M) of a home-built microscope. The output of a white LED (Thorlabs, MCWHL6), which is combined to the UV light with a dichroic mirror (Thorlabs, DMLP425R), was used for bright-filed imaging. The emission from the sample and transmitted/scattered UV light were collected with an objective lens (Olympus, PLN10X) and split into two portions using a beam splitter with a ratio of 1:1. One was focused onto a complementary metal oxide semiconductor (CMOS) color camera (Mightex, SCE-C030-U) with an achromatic lens (Thorlabs, AC254-100-A-ML, f = 100) for recording bright-filed images. The other part was filtered by a long-pass filter (Semrock, BLP01-405R-25) to remove the excitation light. The extracted emission was imaged onto the adjustable slit (Thorlabs, VA100/M) with an achromatic lens (Thorlabs, AC254-100-A-ML, f = 100) for selection of the observation area of interest for the spectral detection. The spatially selected emission was spectrally dispersed by a transmission grating (RSpec, SA-100, 100 groove/mm), which is usually used in the field of astronomical spectroscopy, and the 0th and 1st order diffracted signals were recorded with a CMOS camera (FLIR, GS3-U3-23S6M-C) as one-line emission image and the corresponding spectra. The observation wavelength was calibrated by measuring transmission spectra of a V10 filter (HOYA, V10) which shows narrow absorption peaks as a source of the white LED. The emission spectral images were acquired at 5 frames per second. The bright-field images were recorded before and after the spectral imaging so as to confirm changes in the color and morphology of the crystalline sample. The overall setup was controlled by a home-built program written in LabVIEW 2018.

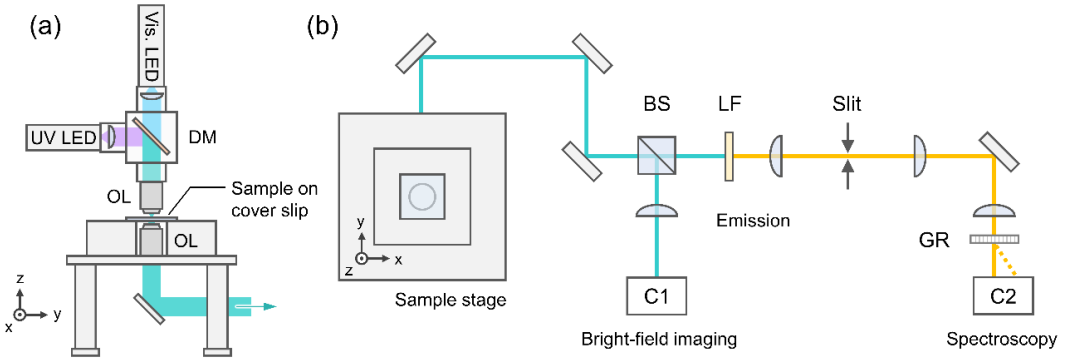

Figure 3.30. Schematic diagram of a hyperspectral imaging system used in the present work. (a) Side view. (b) Top view. DM: dichroic mirror, OL: objective lens, BS: non-polarizing beam splitter, LF: longpass filter, Slit: adjustable slit, GR: transmission grating, C1: CMOS camera for bright-field imaging, C2: CMOS camera for spectroscopy. Reproduced from ref II.

3.4.3 Details of a home-built Raman microscope

The light source was a He-Ne laser (Thorlabs, HNL210LB) centered at 632.8 nm. The output was spectrally cleaned up by a volume Bragg bandpass filter (OptiGrate, BP-633-M) and the spot was magnified by a factor of 3 with a beam expander for matching with pupil of an objective lens. The laser light was introduced into an inverted microscope (Olympus, IX73) and focused to the sample on the cover slip by the objective lens (Olympus, LUCPLFLN60X, NA 0.7). Raman scattering light was collected with the same objective lens and guided into a spectrograph with a half mirror (50:50). Unwanted Rayleigh scattering was effectively removed by three volume Bragg notch filters (OptiGrate, BNF-633-OD3-11M). Raman spectra were detected by a charge-coupled device (Andor, DU401A-BFV-SG) equipped with a polychromator (Jobin Yvon, HR-320, f = 320 mm, 1200 grooves/mm). The wavenumber calibration was performed using line emission of a neon lamp. The wavenumber resolution was ca. 4 cm^{-1}. Ultraviolet light at 365 nm (Thorlabs, M365L2) was irradiated to the sample through an optical fiber for initiation of PCLT. The Raman spectra were recorded at every 1 second during the PCLT process and 10 spectra were typically averaged into 1 spectrum. The bright-field images were also monitored by a monochrome CMOS camera (FLIR, GS3-U3-23S6M-C) for tracking the morphological change of the sample. The overall setup was controlled by a home-built program written in LabVIEW 2018.

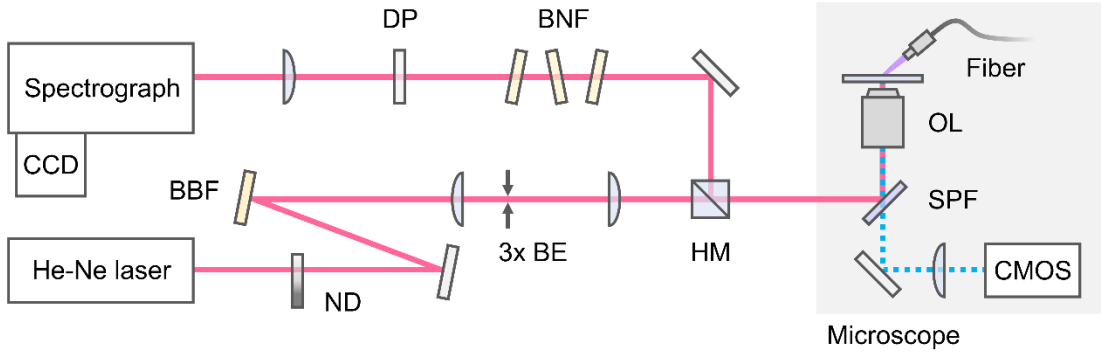

Figure 3.31. Schematic diagram of a Raman microscope used in the present work. ND: neutral density filter, BBF: volume Bragg bandpass filter, BE: beam expander (3x), HM: half mirror (50:50), SPF: shortpass filter (cutoff 505 nm), OL: objective lens (60x, NA 0.7), BNF: volume Bragg notch filter, DP: depolarizer, CCD: charge-coupled device, CMOS: complementary metal oxide semiconductor camera. Reproduced from ref II.

3.4.4 Procedures for evaluating photoinduced crystal melting

3.4.4.1 PL spectrum of SO crystal during PCLT

The **SO** crystal, obtained by recrystallization from MeOH, was placed on a slide glass under a microscope (instrumentation A). Next, UV light was irradiated on the sample through the

microscope. Movie was recorded under continuous UV irradiation using an Olympus U-MWUS mirror unit (excitation, 330–385 nm; emission, >420 nm). Photographic images of Figure 2a were captured from the movie, while Movies[41] were obtained by changing the speed. Fluorescence microscope images in Figure 2b were taken through an Olympus U-MWBS mirror unit (excitation, 460–490 nm; emission, >500 nm).

3.4.4.2 Luminescence lifetime of SO crystal after UV-irradiation.

The **SO** crystal, obtained by recrystallization from MeOH, was placed on a slide glass under a microscope (instrumentation A). Next, UV light was irradiated on the sample through the microscope for 1 minute. The decay curve of the PL intensity at 575 nm was acquired with a HORIBA DeltaFlex multichannel scaling system using DeltaDiode for excitation (368 nm). The area-weighted average lifetime τ_p = 15 μs was obtained from a triple-exponential fit using a HORIBA EZTime software (τ_1 = 16 μs (55%), τ_2 = 5.0 μs (12%), τ_3 = 40 μs (33%)). The reduced chi-square of the curve fitting was 1.10.

3.4.4.3 PL spectra of pristine SO powder during PCLT

The pristine **SO** powder, obtained by the spontaneous crystallization of the SCL, was placed on a slide glass under a microscope (instrumentation A). Next, UV light was irradiated on the sample through the microscope, and the PL spectra were acquired after <1, 10, and 30 s irradiation (Figure 3.4). The PL spectrum of the SCL, obtained as previously reported,[31] is shown for comparison. The PL spectra almost perfectly overlapped that of **SO** in the SCL state. Based on the results in Chapter 2,[31] I concluded that the emerging emission is of the planar conformer.

3.4.4.4 PL spectra of SO in a SCL state at higher temperatures

The **SO** SCL was placed in a quartz tube in an Ar atmosphere, and the tube was capped with a rubber septum. The PL spectra of the SCL were acquired using a JASCO FP-8200 spectrofluorometer equipped with a CoolSpeK USP-203-B cryostat (UNISOKU) with an L42 sharp cut filter (HOYA, longpass, > 420 nm) and a U340 bandpass filter (HOYA, λ_{ex} = 368 nm). The emission was mostly quenched at 55 °C, which is lower than the melting point (59.5 °C), even in the Ar atmosphere. Therefore, the increase in the emission intensity in air during melting by continuous UV irradiation (Figure 3.7 and Figure 3.8) indicated that the temperature was not high enough to cause thermal melting.

3.4.4.5 Excitation-wavelength-dependence of photoresponse

The **SO** crystal was placed on a slide glass under a microscope (instrumentation A). After obtaining the bright-field and polarizing photographic images of the crystal with a mirror unit (U-MBFL3), the mirror unit was switched to U-MWBS to irradiate the sample with BL (Figure 3.5b and Figure 3.6a–b). Photographic images of the samples were recorded, and the mirror unit was

switched to U-MWUS to irradiate the sample with UV light for the indicated periods.

3.4.5 Evaluating photoresponse before macroscopic melting

3.4.5.1 PL spectral tracking during irradiation for short periods (Figure 3.8 and Figure 3.32)

A **SO** crystal was placed on a cover strip on the sample stage of instrumentation B, and subjected to the experimental process described in Section 1 (18 mW cm^{-2}). Figure 3.8 and Figure 3.32 show two-dimensional representations of the results obtained using a different crystal. The intensity of the transient emission at approximately 520 nm and the length of the inductive period depended on the samples, which suggests that these parameters are determined by the crystallinity and/or thickness of the crystal.

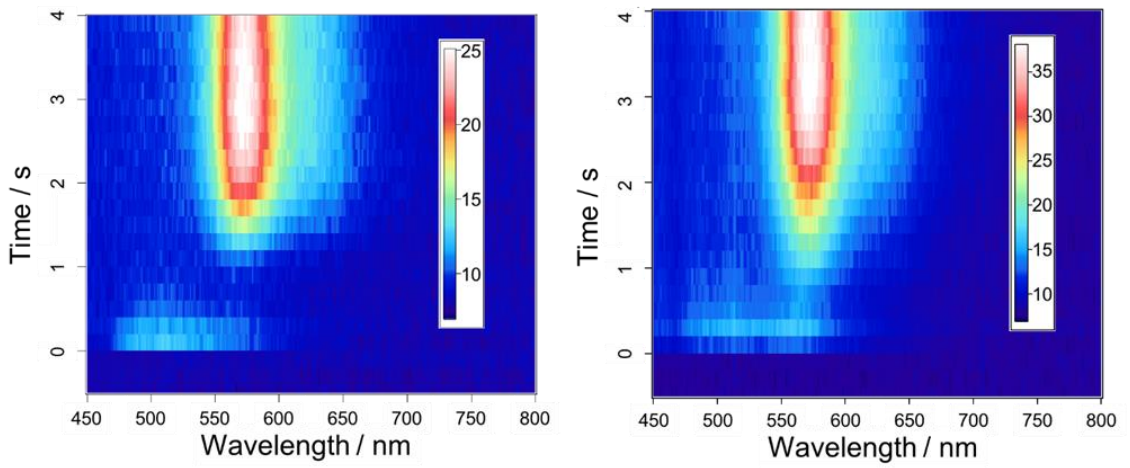

Figure 3.32. Evolution of PL spectra of different crystal samples during continuous UV-light irradiation. Note that left panel is the same as that in Figure 3.8a.

3.4.5.2 Reversibility of the photoresponse

A **SO** crystal was placed on a cover strip on the sample stage of instrumentation A. The PL spectrum was recorded initially (Figure 3.29, red trace) and after UV irradiation for 4 seconds (yellow trace), confirming the decrease in the intensity and the progress of crystal loosening (1st step). The decrease in the intensity at 515 nm is approximately 30%, which corresponds to only 10% progress for disappearing green emission according to Figure 3.8b. Then, the UV irradiation was stopped, and the solid was kept in the dark for 20 minutes. After that, the PL spectrum was recorded (blue trace), which was revealed to be unchanged.

3.4.5.3 Low-temperature PL measurements of SO crystal

The **SO** crystal or SCL was placed in a quartz tube and capped with a rubber septum in air. The PL spectra were acquired at –30 °C using a JASCO FP-8200 spectrometer equipped with a CoolSpeK USP-203-B cryostat (UNISOKU) with an L42 sharp-cut filter (HOYA, longpass, > 420 nm) and a U340 bandpass filter (HOYA) (λ_{ex} = 368 nm). Since the emission of the SCL is from the planar conformer, it can be concluded that the difference in the PL spectra is because of the emission from the skew conformer in the crystal (Figure 3.9).

3.4.5.4 Single-crystal X-ray structure analysis (Figure 3.16)

Single crystal of **SO** suitable for the X-ray crystal structure analysis was obtained by cooling MeOH solution. Data were successively collected at 123, 223, and 300 K using the same crystal on a Rigaku XtaLAB Synergy-R diffractometer with graphite monochromated MoKα radiation (λ = 0.71075 Å) in the ω-scan mode. The crystal was cooled by a stream of cold N_2 gas. Collection, indexing, peak integration, cell refinement, and scaling of the diffraction data were performed using the CrysAlisPro (Rigaku) software. The structure was solved by direct method (SHELXT 2018) and refined by full-matrix least-square refinement on F^2 (SHELXL2018). The non-hydrogen atoms were refined anisotropically. All hydrogen atoms were placed on the calculated positions and refined using the riding model.

Table 3.3. Crystallographic Data for **SO** (CCDC 2095928, 2189552, 2189553)

Empirical formula	$C_{28}H_{44}Br_2O_3SSi_2$	$C_{28}H_{44}Br_2O_3SSi_2$	$C_{28}H_{44}Br_2O_3SSi_2$
Formula weight	676.69	676.69	676.69
Temperature / K	123	223	300
Crystal system	Monoclinic	Monoclinic	Monoclinic
Space group	$P\,2_1/n$	$P\,2_1/n$	$P\,2_1/n$
a / Å	14.1498(4)	14.1870(4)	14.2291(4)
b / Å	9.2174(3)	9.2501(3)	9.2419(3)
c / Å	25.7482(8)	26.1208(7)	26.5165(7)
α / °	90	90	90
β / °	95.165(3)	95.646(2)	96.382(3)
γ / °	90	90	90
Volume / Å^3	3344.56(18)	3411.23(17)	3465.41(18)
Z	4	4	4
ρ (calcd) / g·cm^{-3}	1.344	1.318	1.297
Crystal size / mm^3	0.4 × 0.2 × 0.1	0.4 × 0.2 × 0.1	0.4 × 0.2 × 0.1
Completeness	99.99%	99.97%	99.97%
Goodness-of-fit on F^2	1.02	1.009	1.009
Final R indexes [$I >= 2\sigma(I)$]	R_1 = 0.0569, wR_2 = 0.1030	R_1 = 0.0642, wR_2 = 0.1205	R_1 = 0.0627, wR_2 = 0.1736
Final R indexes [all data]	R_1 =0.0958, wR_2 = 0.1135	R_1 = 0.1273, wR_2 = 0.1394	R_1 = 0.1517, wR_2 = 0.2132
CCDC number	2095928	2189552	2189553

3.4.5.5 Single-crystal X-ray structure analysis before and after UV irradiation

Single-crystal X-ray structure analysis was performed first for an unirradiated **SO** crystal (A), and then UV light was irradiated for 10 seconds before the second measurement (B). Again, UV light was irradiated for 10 seconds, and then the third measurement was performed (C). All measurements were performed at 300 K.

Table 3.4. Crystallographic Data for **SO** (CCDC 2095928, 2189552, 2189553)

Empirical formula	$C_{28}H_{44}Br_2O_3SSi_2$	$C_{28}H_{44}Br_2O_3SSi_2$	$C_{28}H_{44}Br_2O_3SSi_2$
Formula weight	676.69	676.69	676.69
Temperature / K	300	300	300
Crystal system	Monoclinic	Monoclinic	Monoclinic
Space group	$P\,2_1/n$	$P\,2_1/n$	$P\,2_1/n$
a / Å	14.2313(6)	14.2260(6)	14.2236(6)
b / Å	9.2571(5)	9.2521(5)	9.2423(4)
c / Å	26.4870(9)	26.4803(10)	26.4876(9)
α / °	90	90	90
β / °	96.271(4)	96.315(4)	96.355(4)
γ / °	90	90	90
Volume / Å^3	3468.5(3)	3464.2(3)	3460.6(2)
Z	4	4	4
ρ (calcd) / g·cm^{-3}	1.296	1.297	1.299
Crystal size / mm^3	0.8 × 0.3 × 0.2	0.8 × 0.3 × 0.2	0.8 × 0.3 × 0.2
Completeness	99.97 %	99.97%	99.95%
Goodness-of-fit on F^2	1.015	1.009	1.013
Final R indexes [$I >= 2\sigma(I)$]	$R_1 = 0.0545$, $wR_2 = 0.1558$	$R_1 = 0.0561$, $wR_2 = 0.1578$	$R_1 = 0.0569$, $wR_2 = 0.1587$
Final R indexes [all data]	$R_1 = 0.1168$, $wR_2 = 0.1863$	$R_1 = 0.1203$, $wR_2 = 0.1897$	$R_1 = 0.1248$, $wR_2 = 0.1940$
CCDC number	2252304	2252305	2252306

3.4.6 Theoretical study on the conformational dynamics of SO

3.4.6.1 DFT calculation for the conformers of SO′

Density functional theory (DFT) and time-dependent (TD)-DFT calculations were conducted at the (U)B3LYP-D3/6-311G(d) level of theory using Gaussian 16 program package.[56] All optimized structures were confirmed to be local energy minima without imaginary frequencies.

3.4.6.2 Raman spectra of SO crystal

A **SO** crystal and supercooled liquid were placed on a cover strip on the sample stage of home-built Raman microscope and subjected to the experimental process described in Section 1.

3.4.6.3 DFT calculation for structural relaxation

To examine the structural relaxation upon photoexcitation, I optimized the geometry taken from the crystal structure of **SO**, in the T_1 state. Frequency calculation confirmed that the optimized relaxed skew structure has no imaginary frequency. The skew conformer relaxed with changing the dihedral angle of the dicarbonyl moiety, affording another local minimum structure than the planar conformer (Figure 3.18). Concomitantly, the silyl moiety moved along the disordered (10–1) plane.

3.4.7 Photoresponses and structures of analogous diketones

3.4.7.1 Photoresponses of OO and SS

Pristine **OO** powder was obtained by the spontaneous crystallization of the SCL, while pristine **SS** powder was obtained through recrystallization by pouring a $CHCl_3$ solution into MeOH under vigorous stirring. A small amount of the sample was placed on a slide glass under a microscope (instrumentation A). Photographic images were obtained using bright-field and polarizing optical microscopes with a mirror unit (U-MBFL3), after which the mirror unit was switched to U-MWUS to irradiate the sample with UV light. The shape of the **SS** crystal did not change even after more than 11 h of irradiation. In contrast, the **OO** crystal melted completely within 1 min.

3.4.7.2 Comparison of single-crystal X-ray structure analysis of SO, OO, and SS

Crystallographic data of **SS** at 300 K have been reported and deposited to CCDC (1986446) previously.[31, 37] Single-crystal of **OO** was obtained by cooling MeOH solution. Data were successively collected at 123 and 173 K using the same crystal on a Rigaku XtaLAB Synergy-R diffractometer with graphite monochromated MoKα radiation ($\lambda = 0.71075$ Å) in the ω-scan mode. The crystal was cooled by a stream of cold N_2 gas. Collection, indexing, peak integration, cell refinement, and scaling of the diffraction data were performed using the CrysAlisPro (Rigaku) software. The structure was solved by direct method (SHELXT 2018) and refined by full-matrix least-square refinement on F^2 (SHELXL2018). The non-hydrogen atoms were refined anisotropically. All hydrogen atoms were placed on the calculated positions and refined using the riding model.

Table 3.5. Crystallographic Data for **OO** (CCDC 2189550–2189551)

Empirical formula	$C_{28}H_{44}Br_2O_4Si_2$	$C_{28}H_{44}Br_2O_3SSi_2$
Formula weight	660.63	660.63
Temperature / K	123	173
Crystal system	Monoclinic	Monoclinic
Space group	$P2_1/c$	$P2_1/c$
a / Å	15.3021(5)	15.3539(4)
b / Å	14.6862(4)	14.7515(3)
c / Å	29.0678(9)	29.2022(8)
α / °	90	90
β / °	98.666(3)	98.737(2)
γ / °	90	90
Volume / Å^3	6457.8(3)	6537.3(3)
Z	8	8
ρ (calcd) / g·cm^{-3}	1.359	1.342
Crystal size / mm^3	0.25 × 0.2 × 0.15	0.25 × 0.2 × 0.15
Completeness	99.90%	99.96%
Goodness-of-fit on F^2	1.163	1.131
Final R indexes [$I >= 2\sigma(I)$]	R_1 = 0.0768, wR_2 = 0.1723	R_1 = 0.0782, wR_2 = 0.1828
Final R indexes [all data]	R_1 = 0.1169, wR_2 = 0.1841	R_1 = 0.1336, wR_2 = 0.1998
CCDC number	2189550	2189551

3.4.7.3 Hirshfeld surface analyses of SO, OO, and SS crystals

Hirshfeld surface analysis provides a way to view molecules as "organic wholes".[55a] To investigate the intermolecular interactions visually and quantitatively, Hirshfeld surfaces of **SO**, **OO**, and **SS** in the crystal structure at 123 K were mapped with normalized contact distance d_{norm} with a fixed color scale of –0.3 (red) to 1.7 (blue) using CrystalExplorer21 software (Figure 3.27).[55b] d_{norm} is defined as follows:

$$d_{\mathrm{norm}} = \frac{d_{\mathrm{i}} - r_{\mathrm{vdW}}}{r_{\mathrm{vdW}}} + \frac{d_{\mathrm{e}} - r_{\mathrm{vdW}}}{r_{\mathrm{vdW}}}$$

where d_i is the distance from the Hirshfeld surface to the nearest nucleus inside the surface, d_e is

the corresponding distance to the nearest nucleus outside the surface, and r_{vdW} is the van der Waals radius of the atoms. The positive (blue) d_{norm} indicates a distance larger than van der Waals contact. As a whole, the surface of **SO** and **OO** are bluer than that of **SS**, and the mean d_{norm} are larger for **SO** and **OO** than **SS**. In addition, the surface area is larger for **SS** than **SO** and **OO** (609 Å^2 vs. 570 and 549 Å^2). The asphericity is also larger for **SS** than **SO** and **OO**. These results suggest that the intermolecular interactions are weaker in **SO** and **OO** than **SS**.

3.4.7.4 Differential scanning calorimetry (DSC)

DSC was performed with a Hitachi NEXTA DSC200 under a flow of nitrogen. Solid samples of **SO** and **OO** were obtained by spontaneous crystallization of the SCL, while that of **SS** was obtained by pouring $CHCl_3$ solution into MeOH with vigorous stirring. The enthalpies of fusion (ΔH_m) of **SO**, **OO**, and **SS** were estimated to be 22, 29, and 40 kJ/mol, respectively, from the area of the endothermic melting peaks appeared in the heating traces. The entropies of fusion (ΔS_m) were estimated according to the formula $\Delta H_m = T_m \Delta S_m$, where T_m is the melting point. Gibbs free energies for the crystal-to-SCL transition at 300 K (ΔG) were estimated to be 2.2, 2.7, and 12 kJ/mol for **SO**, **OO**, and **SS**, respectively, according to the formula $\Delta G = \Delta H_m - T \Delta S_m$.

3.4.7.5 DFT calculation

DFT calculations were conducted at the (U)B3LYP-D3/6-311G(d) level of theory using Gaussian 16 program package.[56] All optimized structures were confirmed to be local energy minima without imaginary frequencies. The skew and planar conformers of **OO SS** were optimized in the T_1 state. Frequency calculation confirmed that all the optimized structures have no imaginary frequency. The calculations suggest that the planar conformers of **OO** and **SS** are more stable than the skew conformer in the T_1 states (Table 3.2).

3.5 References and Note

1. W.-C. Xu, S. Sun and S. Wu, *Angew. Chem. Int. Ed.* 2019, **58**, 9712–9740.
2. Y. Norikane, Y. Hirai and M. Yoshida*, Chem. Commun*. 2011, **47**, 1770–1772.
3. Y. Okui and M. Han, *Chem. Commun.* 2012, **48**, 11763–11765.
4. E. Uchida, K. Sakaki, Y. Nakamura, R. Azumi, Y. Hirai, H. Akiyama, M. Yoshida and Y. Norikane, *Chem. Eur. J.* 2013, **19**, 17391–17397.
5. M. Hoshino, E. Uchida, Y. Norikane, R. Azumi, S. Nozawa, A. Tomita, T. Sato, S. Adachi and S. Koshihara, *J. Am. Chem. Soc.* 2014, **136**, 9158–9164.
6. P. Kumar, A. Srivastava, C. Sah, S. Devi and S. Venkataramani, *Chem. Eur. J.*, 2019, **25**, 11924–11932.
7. H. J. Meteling, F. Bosse, L. Schlichter, B. J. Tyler, H. F. Arlinghaus and B. J. Ravoo, *Small*, 2022, **18**, 2203245.

8. Y. Norikane, E. Uchida, S. Tanaka, K. Fujiwara, E. Koyama, R. Azumi, H. Akiyama, H. Kihara and M. Yoshida, *Org. Lett.* 2014, **16**, 5012–5015.
9. K. Ishiba, M. Morikawa, C. Chikara, T. Yamada, K. Iwase, M. Kawakita and N. Kimizuka, *Angew. Chem. Int. Ed.* 2015, **54**, 1532–1536.
10. M. A. Gerkman, R. S. L. Gibson, J. Calbo, Y. Shi, M. J. Fuchter and G. G. D. Han, *J. Am. Chem. Soc.* 2020, **142**, 8688−8695.
11. Z.-Y. Zhang, Y. He, Z. Wang, J. Xu, M. Xie, P. Tao, D. Ji, K. Moth-Poulsen and T. Li, *J. Am. Chem. Soc.* 2020, **142**, 12256–12264.
12. Q. Qiu, S. Yang, M. A. Gerkman, H. Fu, I. Aprahamian and G. G. D. Han, *J. Am. Chem. Soc.* 2022, **144**, 12627–12631.
13. H. Akiyama and M. Yoshida, *Adv. Mater.* 2012, **24**, 2353–2356.
14. X. Huang, Z. Shangguan, Z.-Y. Zhang, C. Yu, Y. He, D. Fang, W. Sun, Y.-C. Li, C. Yuan, S. Wu and T. Li, *Chem. Mater.* 2022, **34**, 2636–2644.
15. L. Kortekaas, J. Simke, D. W. Kurka and B. J. Ravoo, *ACS Appl. Mater. Interfaces*, 2020, **12**, 32054–32060.
16. E. Uchida, R. Azumi and Y. Norikane, *Chem. Lett.* 2014, **43**, 1619–1621.
17. G. Xu, S. Li, C. Liu and S. Wu, *Chem. Asian J.* 2020, **15**, 547–554.
18. S. Saito, S. Nobusue, E. Tsuzaka, C. Yuan, C. Mori, M. Hara, T. Seki, C. Camacho, S. Irle and S. Yamaguchi, *Nat. Commun.* 2016, **7**, 12094.
19. Y. Sagara, S. Yamane, M. Mitani, C. Weder and T. Kato, *Adv. Mater.* 2016, **28**, 1073–1095.
20. K. Li, Y. Lin and C. Lu, *Chem. Asian J.* 2019, **14**, 715–729.
21. T. Mutai, T. Sasaki, S. Sakamoto, I. Yoshikawa, H. Houjou and S. Takamizawa, *Nat. Commun.* 2020, **11**, 1824.
22. C. Matsuhashi, H. Oyama, H. Uekusa, A. Sato-Tomita, K. Ichiyanagi, S. Maki and T. Hirano, *CrystEngComm* 2022, **24**, 3332–3337.
23. F. Ito, *Symmetry* 2020, **12**, 1726.
24. N. Oka, F. Ito, Y. Haketa, H. Maeda, T. Miyano, N. Tohnai, S. Ito, H. Miyasaka and S. Ozeki, *Chem. Eur. J.* 2018, **24**, 4343–4349.
25. P.-Z. Chen, L.-Y. Niu, H. Zhang, Y.-Z. Chen and Q.-Z. Yang, *Mater. Chem. Front.* 2018, **2**, 1323–1327.
26. F. Ito, Y. Suzuki, J. Fujimori, T. Sagawa, M. Hara, T. Seki, R. Yasukuni and M. L. de la Chapelle, *Sci. Rep.* 2016, **6**, 22918.
27. X. Ye, Y. Liu, Y. Lv, G. Liu, X. Zheng, Q. Han, K. A. Jackson and X. Tao, *Angew. Chem. Int. Ed.* 2015, **54**, 7976–7980.
28. H. M. D. Bandara and S. C. Burdette, *Chem. Soc. Rev.* 2012, **41**, 1809–1825.
29. M. Okaji, M. Yamauchi and S. Masuo, *Chem. Lett.* 2022, **54**, 473–476.

30. M. Yamauchi, K. Yokoyama, N. Aratani, H. Yamada and S. Masuo, *Angew. Chem. Int. Ed.* 2019, **58**, 14173–14178.
31. M. Komura, T. Ogawa and Y. Tani, *Chem. Sci.* 2021, **12**, 14363–14368.
32. Kenry, C. Chen and B. Liu*, Nat. Commun.* 2019, **10**, 2111.
33. S. Hirata, *Adv. Opt. Mater.* 2017, **5**, 1700116.
34. P. Xue, J. Ding, P. Wang and R. Lu*, J. Mater. Chem. C* 2016, **4**, 6688–6706.
35. Goudappagouda, A. Manthanath, V. C. Wakchaure, K. C. Ranjeesh, T. Das, K. Vanka, T. Nakanishi and S. S. Babu, *Angew. Chem. Int. Ed.* 2019, **58**, 2284–2288.
36. V. C. Wakchaure, S. D. Veer, A. D. Nidhankar, Goudappagouda, R. Nayak, K. Asokan, S. Ravindranathan and S. S. Babu, *Chem. Commun.* 2022, **58**, 1998–2001.
37. Y. Tani, M. Komura and T. Ogawa, *Chem. Commun.* 2020, **56**, 6810–6813.
38. Y. Tani, M. Terasaki, M. Komura and T. Ogawa, *J. Mater. Chem. C* 2019, **7**, 11926–11931.
39. Y. Takewaki, T. Ogawa and Y. Tani, *Front. Chem.* 2022, **9**, 812593.
40. Unlike azobenzenes, photoisomerization of **SO** does not proceed through a conical intersection according to theoretical calculations (Figure 3.1b and Figure 3.15).
41. a) Y. Tani, (2023/4/28) Crystal melting under fluorescence microscope, YouTube. Retrieved from https://youtu.be/-atobxlggBk; b) Y. Tani, (2023/4/28) Photo-induced luminescence changes, YouTube. Retrieved from https://youtu.be/EfO-hi7ZVa4
42. Y. Zhao, L. Ma, Z. Huang, J. Zhang, I. Willner, X. Ma and H. Tian, *Adv. Opt. Mater.* 2022, **10**, 2102701.
43. Y. Tao, C. Liu, Y. Xiang, Z. Wang, X. Xue, P. Li, H. Li, G. Xie, W. Huang and R. Chen, *J. Am. Chem. Soc.* 2022, **144**, 6946–6953.
44. L. Huang, L. Liu, X. Li, H. Hu, M. Chen, Q. Yang, Z. Ma and X. Jia, *Angew. Chem. Int. Ed.* 2019, **58**, 16445–16450.
45. J. Yang, X. Zhen, B. Wang, X. Gao, Z. Ren, J. Wang, Y. Xie, J. Li, Q. Peng, K. Pu and Z. Li, *Nat. Commun*. 2018, **9**, 840.
46. J.-A. Li, J. Zhou, Z. Mao, Z. Xie, Z. Yang, B. Xu, C. Liu, X. Chen, D. Ren, H. Pan, G. Shi, Y. Zhang and Z. Chi, *Angew. Chem. Int. Ed.* 2018, **57**, 6449–6453.
47. L. Gu, H. Shi, M. Gu, K. Ling, H. Ma, S. Cai, L. Song, C. Ma, H. Li, G. Xing, X. Hang, J. Li, Y. Gao, W. Yao, Z. Shuai, Z. An, X. Liu and W. Huang, *Angew. Chem. Int. Ed.* 2018, **57**, 8425–8431.
48. K. Morimoto, D. Kitagawa, H. Sotome, S. Ito, H. Miyasaka and S. Kobatake, *Angew. Chem. Int. Ed.,* 2022, **61**, e202212290.
49. K. Morimoto, D. Kitagawa, F. Tong, K. Chalek, L. J. Mueller, C. J. Bardeen and S. Kobatake, *Angew. Chem. Int. Ed.,* 2022, **61**, e202114089.
50. K. Morimoto, D. Kitagawa, C. J. Bardeen and S. Kobatake, *Chem. Eur. J.*, 2023, **29**,

e202203291.

51. P. Kotula, A. R. H. Walker and K. B. Migler, *Soft Matter* 2016, **12**, 5002–5010.
52. D. de Loera, A. Stopin and M. A. Garcia-Garibay*, J. Am. Chem. Soc.* 2013, **135**, 6626–6632.
53. Y. Kim, H. L. Strauss and R. G. Snyder, *J. Phys. Chem.* 1989, **93**, 7520–7526.
54. This type of a structure having both ordered and disordered layers has been reported in a PCLT-active azobenzene derivative as well. See ref 5.
55. a) M. A. Spackman and D. Jayatilaka, *CrystEngComm* 2009, **11**, 19–32; b) P. R. Spackman, M. J. Turner, J. J. McKinnon, S. K. Wolff, D. J. Grimwood, D. Jayatilaka and M. A. Spackman, *J. Appl. Cryst.* 2021, **54**, 1006–1011.
56. M. J. Frisch, G. W. Trucks, H. B. Schlegel, G. E. Scuseria, M. A. Robb, J. R. Cheeseman, G. Scalmani, V. Barone, G. A. Petersson, H. Nakatsuji, X. Li, M. Caricato, A. V. Marenich, J. Bloino, B. G. Janesko, R. Gomperts, B. Mennucci, H. P. Hratchian, J. V. Ortiz, A. F. Izmaylov, J. L. Sonnenberg, D. Williams-Young, F. Ding, F. Lipparini, F. Egidi, J. Goings, B. Peng, A. Petrone, T. Henderson, D. Ranasinghe, V. G. Zakrzewski, J. Gao, N. Rega, G. Zheng, W. Liang, M. Hada, M. Ehara, K. Toyota, R. Fukuda, J. Hasegawa, M. Ishida, T. Nakajima, Y. Honda, O. Kitao, H. Nakai, T. Vreven, K. Throssell, J. A. Montgomery, Jr., J. E. Peralta, F. Ogliaro, M. J. Bearpark, J. J. Heyd, E. N. Brothers, K. N. Kudin, V. N. Staroverov, T. A. Keith, R. Kobayashi, J. Normand, K. Raghavachari, A. P. Rendell, J. C. Burant, S. S. Iyengar, J. Tomasi, M. Cossi, J. M. Millam, M. Klene, C. Adamo, R. Cammi, J. W. Ochterski, R. L. Martin, K. Morokuma, O. Farkas, J. B. Foresman, and D. J. Fox, , *Gaussian 16 Rev. C.02*; Wallingford, CT, 2019.

Chapter 4 Conclusion

This thesis reports unique room-temperature phosphorescence (RTP) of unsymmetrical diketone in liquid and solid state. Conventional metal-free organic RTP molecules were designed for suppressing non-radiative decay because of their small phosphorescence rate constant (k_p). In contrast, thienyl diketone framework has k_p and flexibility of structure. In addition, desymmetrizing substitution of thienyl diketone particularly affected on intermolecular interactions in aggregation state. I envisioned that desymmetrizing thienyl diketone framework itself would lead to new properties that conventional molecules could not achieve.

Chapter 2 describes the efficient RTP in a solvent-free liquid state in air, which was realized through desymmetrizing a C_2-symmetrical thienyl diketone into thienyl furyl diketone. The unsymmetrical flexible core kinetically stabilized the SCL state even in the presence of seed crystals or under pricking or shearing stresses. Notably, only the liquid exhibits RTP; the solution and crystalline solid are virtually non-emissive. I concluded that the liquid was sufficiently dense to benefit from the intermolecular (external) heavy atom effect and suppress oxygen diffusion, while being sufficiently flexible to generate an intrinsically emissive planar conformer. In addition, the unsymmetrical diketone exhibited thermochromic phosphorescence, which stemmed from its fluidity. This work demonstrated the significance of an unsymmetrical flexible core for realizing RTP in a condensed, yet loose liquid state.

Chapter 3 describes photo-induced crystal-to-liquid phase transition (PCLT) with changing RTP properties of the unsymmetrical thienyl furyl diketone. The dynamic multistep changed in the luminescence color and intensity visualized the PCLT process involving two-step conformation changes, which furthered understanding of the melting phenomenon at the molecular level. Based on the results and comparisons with the other two diketone derivatives, I clarified that the presence of a disordered layer in a crystal was an important factor for PCLT in diketone scaffolds. It should be noted that unlike the PCLT of conventional photochromic motifs, such as azobenzenes, the diketone demonstrated PCLT based on conformational isomerization, *i.e.*, rotation around single bonds. Considering that various photofunctional molecules are not photochromic as a single molecule but exhibit considerable structural changes at the excited states, this work should lead to the diversification and multifunctionalization of PCLT-active motifs.

The present reports indicate the potential benefits of desymmetrizing the diketone framework with large k_p. This approach successfully led to the realization of liquid RTP and PCLT with luminescent property changes due to increase molecular conformational freedom, which affects thermal and kinetic properties of aggregate states without losing RTP from planar conformer. I believe that these findings accelerate the enhancement of RTP efficiency and diversify the photofunctions of metal-free organic compounds.